https://lib.uliege.be https://matheo.uliege.be

Response surface-based prediction of ship resistance in shallow water conditions

Auteur : p243957
Promoteur(s) : Rigo, Philippe
Faculté : Faculté des Sciences appliquées
Diplôme : Master : ingénieur civil mécanicien, à finalité spécialisée en "Advanced Ship Design"
Année académique : 2022-2023
URI/URL : http://hdl.handle.net/2268.2/18068

Avertissement à l'attention des usagers :

Tous les documents placés en accès ouvert sur le site le site MatheO sont protégés par le droit d'auteur. Conformément aux principes énoncés par la "Budapest Open Access Initiative"(BOAI, 2002), l'utilisateur du site peut lire, télécharger, copier, transmettre, imprimer, chercher ou faire un lien vers le texte intégral de ces documents, les disséquer pour les indexer, s'en servir de données pour un logiciel, ou s'en servir à toute autre fin légale (ou prévue par la réglementation relative au droit d'auteur). Toute utilisation du document à des fins commerciales est strictement interdite.

Par ailleurs, l'utilisateur s'engage à respecter les droits moraux de l'auteur, principalement le droit à l'intégrité de l'oeuvre et le droit de paternité et ce dans toute utilisation que l'utilisateur entreprend. Ainsi, à titre d'exemple, lorsqu'il reproduira un document par extrait ou dans son intégralité, l'utilisateur citera de manière complète les sources telles que mentionnées ci-dessus. Toute utilisation non explicitement autorisée ci-avant (telle que par exemple, la modification du document ou son résumé) nécessite l'autorisation préalable et expresse des auteurs ou de leurs ayants droit.

Response surface-based prediction of ship resistance in shallow water conditions

Ravindu Udayanga

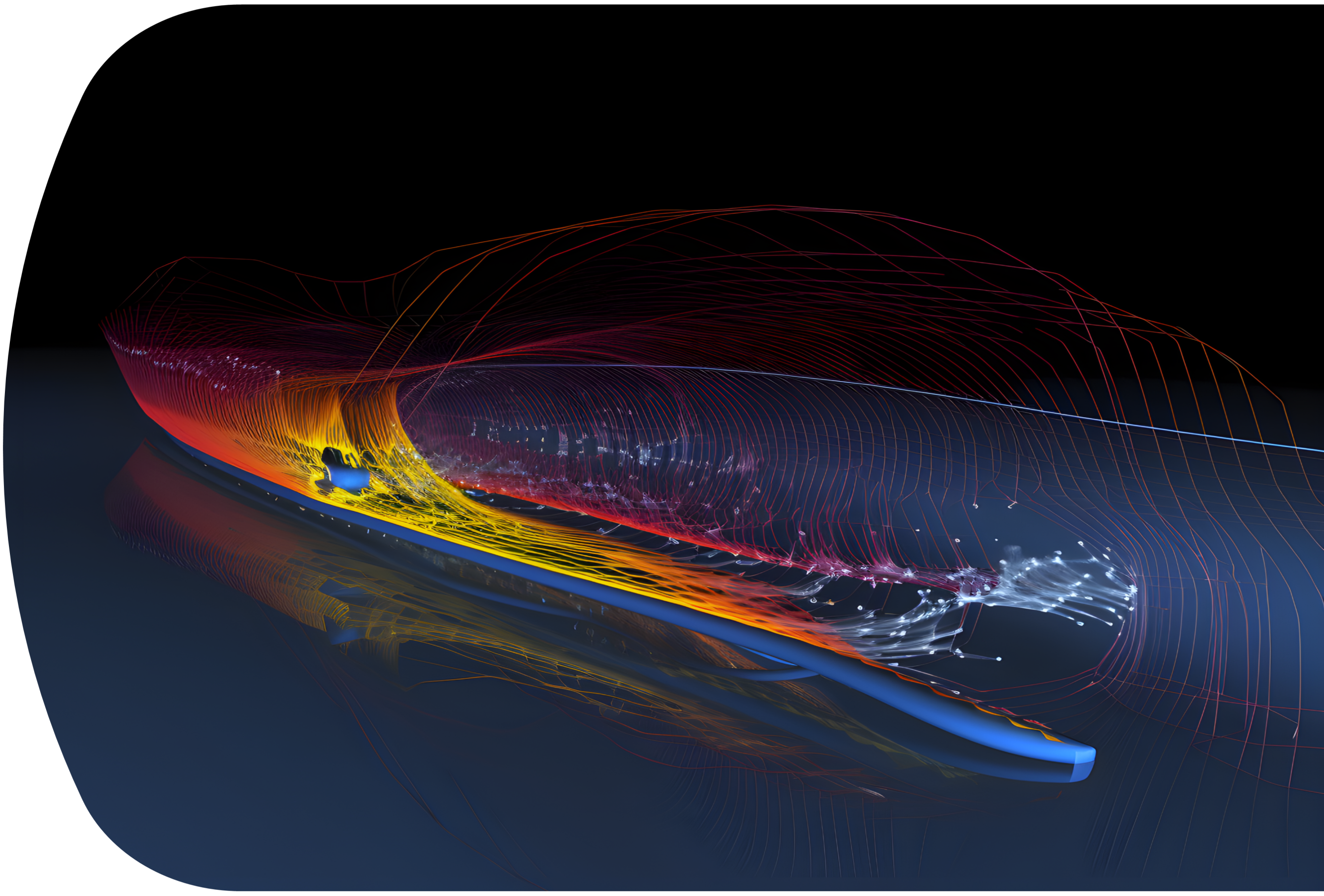

Created with MidjourneyAI, published under creative commons license

MASTER'S THESIS

University of Rostock

&

DST Entwicklungszentrum für Schiffstechnik und Transport systeme e. V.

Response surface-based prediction of ship resistance in shallow water conditions (2023)

The work in this thesis was carried out in the:

DST Entwicklungszentrum für Schiffstechnik und Transportsysteme e. V.
Duisburg, Germany

Faculty Supervisor:	Prof. Nikolai Kornev (University of Rostock, Germany)
Direct Supervisors:	Dipl.-Ing. Jan Kaufmann(DST, Duisburg)
	Dipl.-Ing. Jens Ley(DST, Duisburg)
Co-reviewer:	Prof. Evert Lataire (University of Ghent, Belgium)

Page intentionally left blank

Abstract

Ships experience increasing hydrodynamic resistance as the depth of the water decreases. This difference in resistance between shallow and deep water is termed as the added resistance in shallow water that exhibits a non-linear behaviour with respect to operational parameters such as water depth to ship draft ratio (h/T), velocity of the ship (v), and depth-based Froude number (Frh). A comprehensive development framework is proposed to generate a surrogate model to estimate shallow water added resistance on a modern chemical oil tanker. The developed model was proven to provide cheaper and faster resistance predictions with acceptable error margins, as compared to the computationally/capitally expensive CFD simulations and model tests.

Several surrogate models were built using Kriging and Artificial Neural Networks (ANN) methods with a dataset containing 556 combinations of water depth (h), draft (T), ship velocity (v), and their corresponding added resistance values (ΔF_T) alculated with RANSE-based OpenFOAM CFD simulations. At their base states, 88% and 64% predictive accuracies were demonstrated by the best Kriging and ANN models with respect to the r^2 matric. After tuning the hyperparameters, the accuracy of the best ANN model went up to 85%. The same hyperparameter tuning process resulted in a Kriging model with 97.6% prediction accuracy, which was identified as the “best performer”. A fully-automated, iterative refinement loop was introduced to further improve the local uncertainties. The finalized iterative loop integrated a squared error and LHS-based adaptive sampling strategy to introduce further information to the local areas with the highest prediction uncertainty at each iterative step. A 0.5% performance improvement was seen on the “best performer” surrogate model after a 20-iteration test run of the loop.

The “best performer” surrogate model is nominated to be integrated into the MARIDATA decision support system, a cutting-edge initiative funded by the German Federal Ministry of Economic Affairs and Climate Action, which is aimed at enhancing the sustainability and efficiency of ship operations. Moreover, the fully open-source, Python-based modelling framework developed is denoted to act as a basis to create surrogate models for shallow water resistance prediction for ships other than the chemical oil tanker considered in this project. With minor improvements, this use case can be extended to predict other ship operational parameters.

Acknowledgements

As my cherished journey with the EMSHIP+ program draws to a close, I am filled with a profound sense of gratitude and accomplishment. Over the past two years, I have gained more than just academic knowledge and professional skills. I have grown as a person, navigating the challenges of a demanding program and emerging on the other side stronger and more confident. Thank you Prof. Philippe Rigo for opening the door two years ago and welcoming me into this land of opportunities. Before you, lie the labour of my love and dedication, the culmination of tremendous hard work.

Throughout the two-year journey at the University of Liege and the University of Rostock, the challenges were countless, each one pushing me out of my comfort zone, and teaching me to adapt, learn, and grow. To the remarkable faculty of the University of Liege and Rostock, my deepest appreciation. You have not only taught me, but you have also inspired me, and for that, I will always remain grateful.

The thesis outcome would not have been the same without the guidance and support of my supervisors. I am immensely grateful to Jens Ley at DST for acknowledging me as a professional and designing this captivating thesis topic per my request. Your trust and encouragement, and all the wisdom have been instrumental in the thesis journey. I am equally indebted to Jan Kaufmann, whose careful supervision and patient mentorship have been nothing short of transformative. Despite his busy schedule, Jan always made time to ensure my understanding of new concepts, spending countless hours imparting his knowledge and experience. His dedication and commitment to my learning experience were both humbling and inspiring. To Jens and Jan, your faith in my abilities has made all the difference. Thank you for guiding me through this enlightening journey. My heartfelt appreciation also extends to Professor Nikolai Kornev, who has played a pivotal role as my faculty supervisor. Amidst his bustling schedule, he was always responsive whenever I sought his guidance.

Dear EMSHIP colleagues of mine, you deserve a special mention for the countless laughs we shared, the many storms we weathered, and the triumphs we celebrated. Your companionship turned obstacles into stepping stones, making the path to success seem less daunting. Thank you for standing tall with me through thick and thin. And my dear beloved, I am immensely blessed to always have you by my side, filling my life with warmth and love throughout this challenging journey. Dearest Kaushala, thank you for the unwavering support and for the love that kept me grounded.

Table of Content

List of Figures

List of Tables

Acronyms

IMO	International Maritime Organization	1
EEDI	Energy Efficiency Design Index	1
EEXI	Energy Efficiency Existing Ship Index	1
SEEMP	Ship Energy Efficiency Management Plan	2
HSVA	Hamburg Ship Model Basin	4
DST	Development Centre for Ship Technology and Transport Systems	4
WSA	Wetted Surface Area	30
SM	Surrogate Model	8
RSM	Response Surface Methodology	8
RS	Response Surface	8
ML	Machine Learning	10
ANN	Artificial Neural Networks	10
RF	Random Forests	10
CFD	Computational Fluid Dynamics	11
DoE	Design of Experiments	11
RMSE	Root Mean Square Error	15
CoD	Coefficient of Determination	15
RAE	Relative Absolute Error	15
IoAd	Index of Agreement	15
HPC	High-Performance Cluster	18
RANS	Reynolds Averaged Navier-Stokes	42
SIMPLE	Semi-Implicit Method for Pressure Linked Equations	42
PISO	Pressure Implicit with Splitting of Operator	42
DNS	Direct Numerical Simulations	43
VoF	Volume of Fluid	47
DoI	Domain of Interest	55
LHS	Latin Hypercube Sampling	60
RFE	Recursive Feature Elimination	67
GPR	Gaussian Process Regression	72
RBF	Radial Basis Function	74
MLP	Multi-Layer Perceptron	75
ReLU	Rectified Linear Unit	76
VT	Voronoi Tessellation	96

Page intentionally left blank

CHAPTER

Introduction

1

The chapter is dedicated to shortly summarize some important aspects of the maritime industry as a whole, and the circumstances that led to this thesis.

1.1 Motivation: calls for sustainability in maritime industry

1.1.1 Background

In response to the mounting public outcry concerning global warming and climate change, and the self-realisation of the importance of a sustainable future, the modern maritime industry y now functions within a strict framework of environmental protection regulations. These regulations are spearheaded by the International Maritime Organization (IMO) through the Marine Environment Protection Committee (MEPC) and the continually evolving convention known as the Prevention of Pollution from Ships (MARPOL) (IMO, 2023). They are set towards goals like maritime decarbonisation, end-of-life management, reduction of toxic emissions, and overall safety and efficiency improvements. The limitations are set not only for the ships yet to be designed but also for ships already in service. As a result, significant progress has been made (Tadros, Ventura, and Guedes, 2023).

- reduction of emissions of nitrogen oxides (NOx) by 80% within a time span of 16-years (2000-2016) and reduction of emissions of sulphur oxides (SOx) by 95% within a time span of 5-years (2010-2015), in selected emission control areas
- achieved and set targets for the reduction of greenhouse emissions through the Energy Efficiency Design Index (EEDI) and Energy Efficiency Existing Ship Index (EEXI) criteria (compared to the baseline 2008 status, reduce the greenhouse emissions in transportation work in the maritime industry by, (i) at least 40% by 2030, and (ii) at last 70% by 2050)

A study conducted by Faber and Hoen (2015) offers a rather paradoxical perspective on the effect of EEDI criteria on the efficiency of ships. The authors discovered that a 20% improvement in efficiency due to EEDI guidelines merely restored the efficiency levels typical to the 1999-2008 shipbuilding era. This finding underlines a drastic downfall followed by a long stagnation period in the efficiency status of newly designed ships (Figure 1.1). Therefore, to keep conforming with all the newly imposed rules and regulations, the shipping industry had to adopt improvised, sophisticated tools and innovative technologies, such as improved efficient engines, electrification of ships, alternative fuel-driven propulsion systems, and design for reuse/recycle concepts. A plethora of these tools and technologies can be attributed to the integration of big data, modern data processing tools and artificial intelligence into maritime operations. One prominent example of big data application within this context is the IMO-regulated Ship Energy Efficiency Management Plan (SEEMP). which is a ship-specific energy regulation protocol mandated for all ships above 400 gross-tonnage capacity (IMO, 2020). The main two parts of the SEEMP are, (I) monitoring ship/fleet performance over time and synthesizing the optimal operational conditions, and (II) a protocol for ships above 5000 gross tonnage should use to collect and report data to the authorized entities.

The particular work addressed by this thesis, associated with the MARIDATA initiative, aligns closely with all the aforementioned aspects of the maritime industry. Funded by the German Federal Ministry of Economic Affairs and Climate Action, MARIDATA was implemented with the goal of enhancing the sustainability of ship operations. MARIDATA aims to achieve its objectives by harnessing the power of big data and leveraging modern analytical tools; as highlighted above, a domain within the maritime industry that has rapidly gained popularity in recent years.

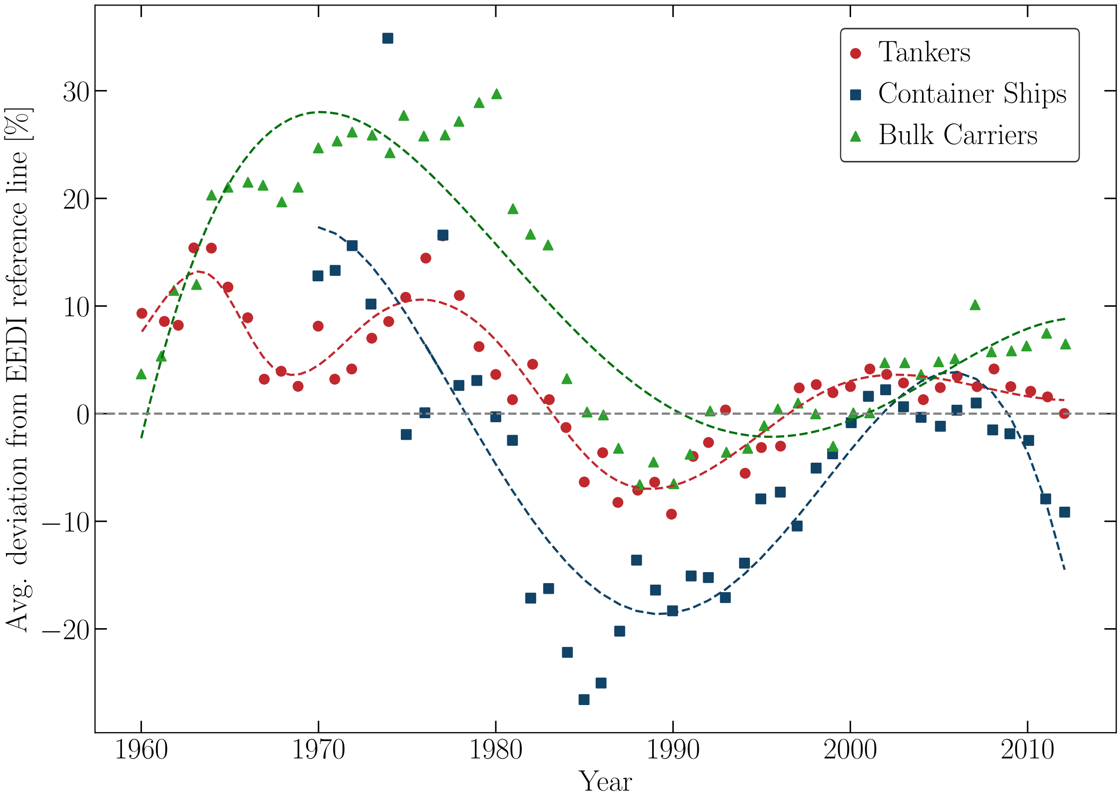

Figure 1.1: Status of efficiency of newly built ships recorded between 1970-2015 period, presented as the average deviation from EEDI reference line (Faber and Hoen, 2015)

1.1.2 MARIDATA initiative and the MARISHALLOW sub-branch

At its essence, MARIDATA resembles the SEEMP as a data-centric decision support system (DSS). However, the scope of MARIDATA transcends the scope of SEEMP by fusing big data analytics with the information gathered from simulation-based methods. The ultimate aim of MARIDATA is to deliver prompt online simulations for a multitude of operational scenarios, to decision-makers both onboard and onshore.

> *"MariData's goal is to develop, improve and classify simulation-based modules for ship energy management using a carefully selected combination of state-of-the-art maritime technologies and experience as well as AI-based tools and methods for a groundbreaking product for holistic ship energy and operations management"*

The system will incorporate arrays of geospatial, technical, environmental, operational and economic data and function as a digital twin of ships that employ it. The advantages of a sophisticated decision support system like MARIDATA would be immense, and some of them are identified as follows (DNV, 2022).

- Speed optimisation: determining the optimal speed for the ship in order to reduce fuel consumption without compromising the schedule
- Weather routing: predict weather patterns and adjust the ship's course accordingly, thereby improving safety and fuel efficiency
- Hull monitoring and maintenance: generating inspection and cleaning schedules of the hull, based on predictions of fouling propagation
- Efficient cargo operation: enabling effective communication among all parties involved in cargo operations in order to reduce delays, and as a result, save fuel for subsequent journeys
- Electric power management: predicting the power demand of the ship by referring to previous power profiles, and efficiently adjusting the use of the ship's power plant and electrical machinery
- Optimization of new designs: predicting the best operational scenarios for a new ship in its design phase and optimizing the hull/appendage geometries, and sizing the auxiliary systems (not an elaborated focus area in the current project layout. Stated as a potential, prospective use-case)

Figure 1.2 demonstrates the potential of future CO_2 reductions predicted for actions that can be assisted by the MARIDATA system. This underscores the pivotal role that the initiative could play in the future, particularly in enhancing sustainability and reducing the environmental impact of the maritime industry. The graph was influenced by a comprehensive review of numerous other studies published by Bouman et al. (2017). The upper and lower limits of the whiskers represent the range of data reviewed, and the vertical black line in the middle represents the median of all datasets for that respective category (Mittendorf, 2023).

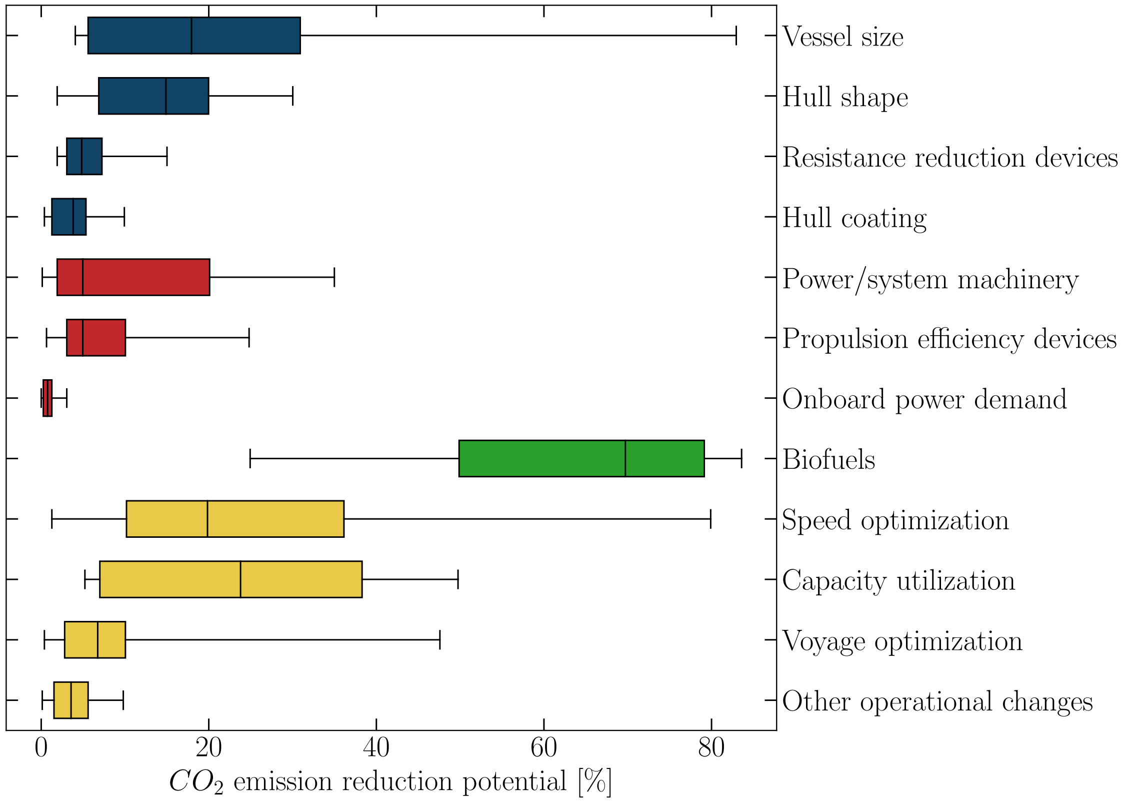

Figure 1.2: The CO_2 reduction potential of actions that can be supported by the MARIDATA system categorized under main focus areas (Bouman et al., 2017)

- 🟦 Hull optimization and resistance reduction
- 🟥 Power management and optimization
- 🟩 Alternative fuels
- 🟨 Optimization of operational parameters

Figure 1.3 briefs the layout of the MARISHALLOW initiative as a schematic diagram. The core idea is to replicate real-world ship systems (technical systems) as data-driven virtual models that predict certain operational parameters. The broad project scope is shared among multiple partners, including Hamburg Ship Model Basin (HSVA) and Development Centre for Ship Technology and Transport Systems (DST). This thesis specifically focuses on the MARISHALLOW branch of this scope which is handled by DST, addressing the shallow water aspects of the proposed information system (as highlighted in Figure 1.3). When predicting ship behaviour under shallow water conditions, resistance is a crucial factor that needs to be taken into account. When water depth decreases (in zones of tidal estuaries for instance), the hydrodynamic conditions change, which in turn increases the resistance exerted on the ship. This increment is generally not linear and thus hard to quantify with simple calculations. As will be discussed in future chapters of this report, an accurate calculation of shallow water should be carried out with either direct model tests or numerical simulations. Many challenges are associated with both methods; For instance, direct model testing requires significant capital investments, while numerical simulations call for sophisticated computational resources and substantial time investments.

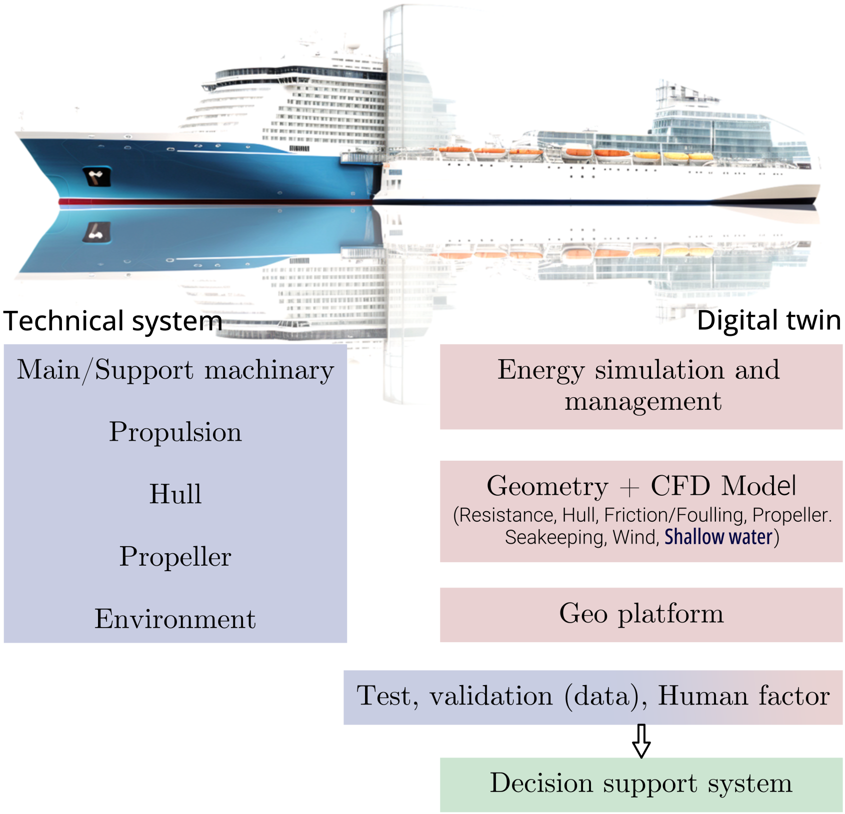

Figure 1.3: The structure of the MARIDATA project presented on the official website, with the specific shallow water portion associated with the project highlighted (Source: maridata.org)

It is not efficient to let a sophisticated decision support system like MARIDATA rely on such costly and lengthy methods when generating predictions. This will defeat the whole purpose of having a decision support system in the first place, that is mimicking ship operational scenarios and coming up with fast predictions to assist maritime stakeholders in making informed decisions. Therefore, a more efficient and time-effective method is essential for the success of the MARISHALLOW component, and ultimately the MARIDATA system itself.

1.2 Scope, objectives and contribution

The MARISHALLOW project, and by extension the work presented with this thesis, should implement a reliable method that appends the capability of generating fast and cheap shallow water resistance predictions to the large MARIDATA system. In search for such a method, the use of “surrogate models” caught the attention. Basically, surrogate models are simplified systems that can replace complex mathematical calculations with satisfactory accuracy. The intended surrogate model will be developed for a single ship, which will be addressed as the “reference ship” in this report. The project will be executed while satisfying some already imposed limitations by the partners of the MARDATA initiative, including the exact reference ship that will be used. It is a medium-sized, modern chemical oil tanker owned by one of the MARIDATA partners. Since the hull of the ship has a unique shape, all the visualizations showcased in this report will conform to a confidentiality agreement placed at the beginning. The shallow water conditions in this project context would be typically encountered in regions like tidal estuaries, the vicinity of ports, and near coastal regions where the reference ship, the chemical oil tanker, could potentially operate. Shallow water is generally defined as a condition where the depth of the water is not significantly greater than the ship's draft. A different state of hydrodynamic conditions is seen in shallow water compared to deep water conditions, which ultimately results in an increase in ship resistance. This increased resistance is addressed as “added resistance in shallow water”.

In order to build an accurate surrogate model, a “training dataset” would be needed. It should consist of a satisfactory number of already calculated sample points that can represent complex patterns and linear/non-linear mathematical relationships between contributing variables. In the case of the MARISHALLOW project, the contributing variables are water depth (h), draft of the ship (T), velocity of the ship (v) and output (prediction) variable is added resistance in shallow water (ΔF_T). Moreover, an “initial dataset” consisting of multiple sample points, that represent the added resistance of shallow water corresponding to multiple combinations of h, T and v values was available at the commencement of the project. Each such combination can be defined as a “sample point”. If the initial dataset is found to be inadequate when generating a reliable surrogate model, an “extended dataset” will be generated. All in all, answers will be sought for the research question,

> *How to use surrogate modelling techniques to develop a comprehensive framework that can replace computationally and economically expensive numerical simulations or direct model testing when predicting the added resistance in shallow water acting on a ship?*

To seek the answers to the main research question, the workflow is structured to achieve the following main objectives.

- Develop a surrogate model using a dataset consisting of the best affordable number of sample points, that guarantees accurate prediction of added resistance exerting on the reference ship when it is operating in limited water depths with different drafts and velocities.
- Explore the accuracy and limitations of the initial surrogate model and apply tools and techniques available in the literature to further tune its performance.
- Developing an iterative loop to continuously improve the already created base surrogate model by adding new sample points.

In order to achieve the above-mentioned main objectives, a couple of sub-objectives were implemented.

- Carrying out a comprehensive literature review to gather information on the state-of-the-art application of surrogate models, tools and techniques used to fine-tune the performance of an already-built surrogate model and the methodology of developing a surrogate model.
- Using a suitable sampling method to generate new combinations of input variables values as sample points and developing a calculation setup to efficiently and accurately evaluate the corresponding added resistance for each combination. Then using those completed sample points to develop the surrogate model.

Once the surrogate model is deemed capable of predicting added resistance up to acceptable accuracy, it will be nominated to integrate into the MARIDATA decision support system, as depicted in Figure 1.3. By utilizing the details about the shallow water resistance predicted by the model, the operational profile of the reference ship can be optimized greatly for improved efficiency. For instance, when the ship is scheduled to sail in a shallow water region in a particular time frame, the speed of the ship can be determined as a compromise between two scenarios; (a) traverse the shallow water region quickly with a fast phase but with increased shallow water added resistance, or (b) sail through the shallow water region slowly with less shallow water added resistance, but while consuming additional fuel to overcome the added resistance throughout an extended duration than before. Ultimately, it is intended that the framework presented by this thesis could be used to develop similar surrogate models for other ships too.

CHAPTER

Initial research and methodology

2

The chapter is dedicated to explaining how the literature and state-of-the-art findings led to the development of the overall methodology of the workflow.

2.1 Introduction to response surface-based surrogate models

Response Surface Methodology (RSM) can be understood as a form of higher-level regression analysis, that can regress through the data points of an available dataset in order to predict the values in unknown voids through interpolation or extrapolation. In a different perspective, RSM is used to synthesize the unknown relationships between input variables in order to predict one or more output variables. First introduced by Box and Wilson (1951), the actual uses of RSM in an engineering context extend far beyond the initial definition given above. Figure 2.1 proves how RSM is used in engineering applications more than any other field in the world. This applies a certain credibility to the decision taken to use RSM in the project context. It can be used in a broad spectrum of applications to develop relationships between a set of independent variables, and a set of dependent variables when the actual relation between them is too complex to cope with, non-existent, or simply not known. The extended uses of the RSM can be listed as follows,

- attain knowledge on a domain of interest of an experiment or a physical phenomena
- estimate the error of an experiment
- study whether a mathematical model developed on experimental data is adequate in terms of accuracy
- predict an observation variable within empty-data regions and use those predictions to optimize the objective variable

Among the above-listed uses, the particular work specifically aims to utilize the capabilities of RSM in prediction aspects. A Response Surface (RS) that can replace a complex mathematical calculation and predict the outcome of that calculation easier and faster is called a Surrogate Model (SM).

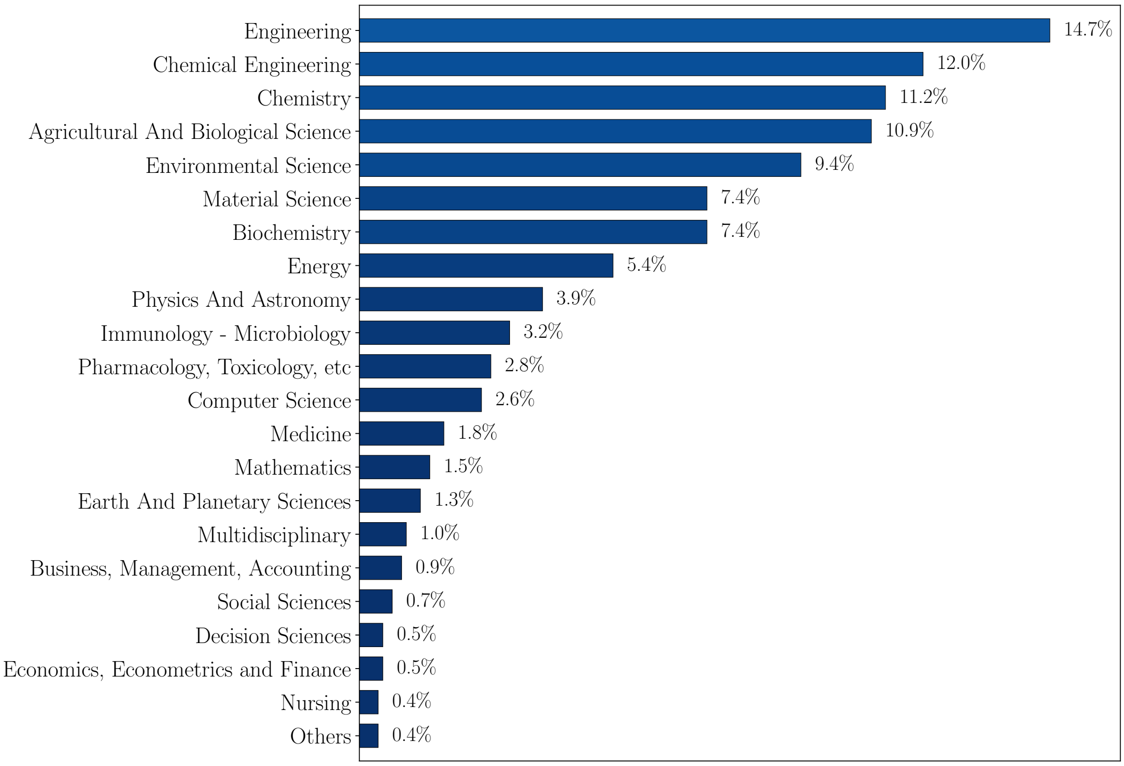

Figure 2.1: Percentage usage of the response surface methodology (RSM) by different industries shows that its presence in engineering applications is more frequent than any other field (Hadiyat, Sopha, and Wibowo, 2022)

2.1.1 Methods used for RS- & ML-based surrogate model generation

Over the years, RSM has been integrated with a multitude of mathematical concepts, making it an integral tool for data management in engineering. There are numerous response surface models available, all operated under the same main objective of developing a simple mathematical model between independent (input, design) and dependent (objective, prediction, output) variables. Given that independent variables are represented by x_i and the dependent variable set is represented by y,

$$y = f\left(x_1, x_2, \dots, x_k\right) + \varepsilon \tag{2.1}$$

The intended surrogate model will take the following forms. ΔF_T is added resistance due to shallow water, ΔC_T is non-denationalized for of added resistance, h is water depth, T is the draft and v is ship velocity. ε is the error/residual or the variability that is not accounted for, in the simplified model (Sarabia and Ortiz, 2009).

$$\begin{aligned} \Delta C_T &= h\left(h, T, v\right) + \varepsilon_h \\ \Delta F_T &= g\left(h, T, v\right) + \varepsilon_g \end{aligned} \tag{2.2}$$

The rationalization for the chosen independent variables is presented with section 3.5, and the rationalization for the choice of possible dependent variables is presented with Section 4.4.1. Based on the accuracy and sensitivity required, the complexity of the RS can be freely chosen. The simplest form is assuming that a linear combination of input variables would estimate the output variables.

$$y = \beta_0 + \beta_1 x_1 + \beta_2 x_2 + ... + \beta_k x_k + \varepsilon \tag{2.3}$$

where β_i would be weighting coefficients determined by the RS algorithm. If further smoothness and complexity are needed, a higher-order polynomial regression or other more sophisticated methods can be chosen. The model for a second-order polynomial RS is given below.

$$y = \beta_0 + \sum_{i=1}^{k} \beta_i x_i + \sum_{i=1}^{k} \beta_{ii} x_i^2 + \sum_{i<j} \sum \beta_{ij} x_i x_j + \varepsilon \tag{2.4}$$

The most commonly used models in RSM are linear combinations or higher-order polynomials due to their simplicity (Box and Tidwell, 1962). The weighting coefficients for these models can be calculated easily using the least-square regression method. While this simplicity is appealing, it is worth noting that, not all relationships in engineering are simple enough to be accurately modelled with polynomial regression. It is probable that non-linear hydrodynamic relationships in shallow water would also demand an enhanced model than a simple polynomial regression. Such higher models are powered by various statistical tools to capture very intricate relationships between input and output variables, resulting in a more reliable surrogate model. Machine Learning (ML) is such a widely known tool that will be used in the project scope. ML models are capable of building SMs by learning from the input datasets and figuring out more complex relationships between variables. Some of the widely known machine learning models are listed below (Uddin et al., 2019; Zhang and Wu, 2021). Even though techniques like Artificial Neural Networks (ANN) and Random Forests (RF) are not directly considered in the RSM context, they can be utilized as SMs that can predict. Also, their development mechanisms and use-cases as SMs align well with the conceptual frameworks of response surface modelling. Therefore, a loose definition of RSM is used in this thesis context in order to encapsulate a wide array of methods that are not inherently RSMs but can be considered as potential solutions.

- Supervised Learning: Linear Regression, Logistic Regression, Decision Trees, RF, Support Vector Machines (SVM), ANN, K-Nearest Neighbors (KNN), Naive Bayes, Gradient Boosting
- Unsupervised Learning: K-Means Clustering, Hierarchical Clustering, Principal Component Analysis (PCA), Independent Component Analysis (ICA), Autoencoders, Generative Adversarial Networks (GAN), Self-Organizing Maps (SOM)
- Reinforcement Learning: Q-Learning: Deep Q-Networks (DQN), Policy Gradient Methods, Actor-Critic Methods

2.1.2 Sampling strategies used in surrogate modelling

To apply RSM, a dataset with a sufficient number of combinations of input variable values is needed, along with the corresponding output variable value for each of these combinations. The set of combinations (samples) of input variables can be generated using a sampling method. The accuracy of the final model largely depends on the quality and variety of the data collected. Thus, proper choice of sampling strategy is a crucial factor in RSM applications. Here, sampling points are presented in the form, $X = [x_1^i, x_2^i, x_3^i, x_4^i....x_n^i]$ with $i = 1, 2, ...$ Different sampling methods available to collect the initial dataset, and any following datasets to improve the surrogate model are listed below (Box and Draper, 1987; E. O. Geiger, 2014; Meng et al., 2015; Yuangyai and Nembhard, 2010).

- Random Sampling: samples are generated on a purely random basis. The simplest sampling strategy available for RS development. There would be no guarantee that generated sample points will represent the whole domain of interest (population of independent variables).
- Stratified Sampling: the domain of interest is divided into classes (strata), based on identical properties, and relative characteristics. Even though the domain would be heterogeneous, each stratum would be homogenous.
- Cluster Sampling: the domain of interest is divided into clusters, and samples are chosen from each cluster to ensure the whole domain is represented.
- Full Factorial Design: when the number of independent variables is small, the full-factorial design can be used to generate all possible combinations as samples.
- Central Composite Design: the full factorial samples are combined with additional samples around the centre and corners of the domain of interest in order to make it easier to capture the curvatures of the RS.
- Design of Experiments (DoE): a tool equipped with systematic sample generations, optimal variable selection, and executing experiments to calculate corresponding dependent (output variables).

Once X is generated from a selected sampling strategy, the corresponding dependent variable set Y should be calculated for each combination using a selected method. Usually, this calculation method would be the one ultimately replaced by the surrogate model, in this project context, Computational Fluid Dynamics (CFD) calculations (will be discussed in chapter 3). The completed sample set with $X \rightarrow Y$ relationship will then act as the foundation for the surrogate model (training set).

2.1.3 Use cases of RS-based surrogate models

The broad spectrum of use cases of RSM-based SMs can be categorized into three main sections, namely, optimization, design, and prediction. In optimization, they are used to simplify relationships between design (input) and objective (output) variables. Then the optimization algorithms are applied on the RSs to locate the optimal points easily. For instance, if a mathematical function is implicit and virtually impossible to optimize with general optimization algorithms, approximating it with an explicit RS such as a polynomial model would make it optimizable (Q. Li, J. Wang, and Su, 2022).

Application of RSM in design tasks is an extension of optimization. If one plans to design a new hull with improved performance, they have to engage in optimization.

However, observing hydrodynamic behaviours at every step of the optimization process would be cumbersome with the complex mathematical equations associated with them. In such a case, a response surface can be developed based on a relatively small dataset, and it can be used for the optimization of the design (Coppedè et al., 2019; P. Wang et al., 2023; Oh, 2020). This will in turn significantly reduce the time taken for the computations too.

Prediction using response surfaces is the use case of RSM that will be important in this work. The base mechanism here is simplifying a complex system into a response surface which can predict the output variables corresponding to new input sample points which were not initially used to build the RS. Within the project scope, the idea is to replace the numerical resistance calculation simulations with an appropriate response surface, so the added resistance in shallow water could be predicted for random operational conditions within a few moments, compared to a few days (the time takes for a numerical simulation to be completed). Since the RS is "replacing" numerical simulations (or in other cases, the actual mathematical model used to calculate the output variable), it is called a "SM". The process of developing the surrogate model will be explained in future sections. The findings and conclusions discussed so far on RSM are summarized in the following Figure 2.2.

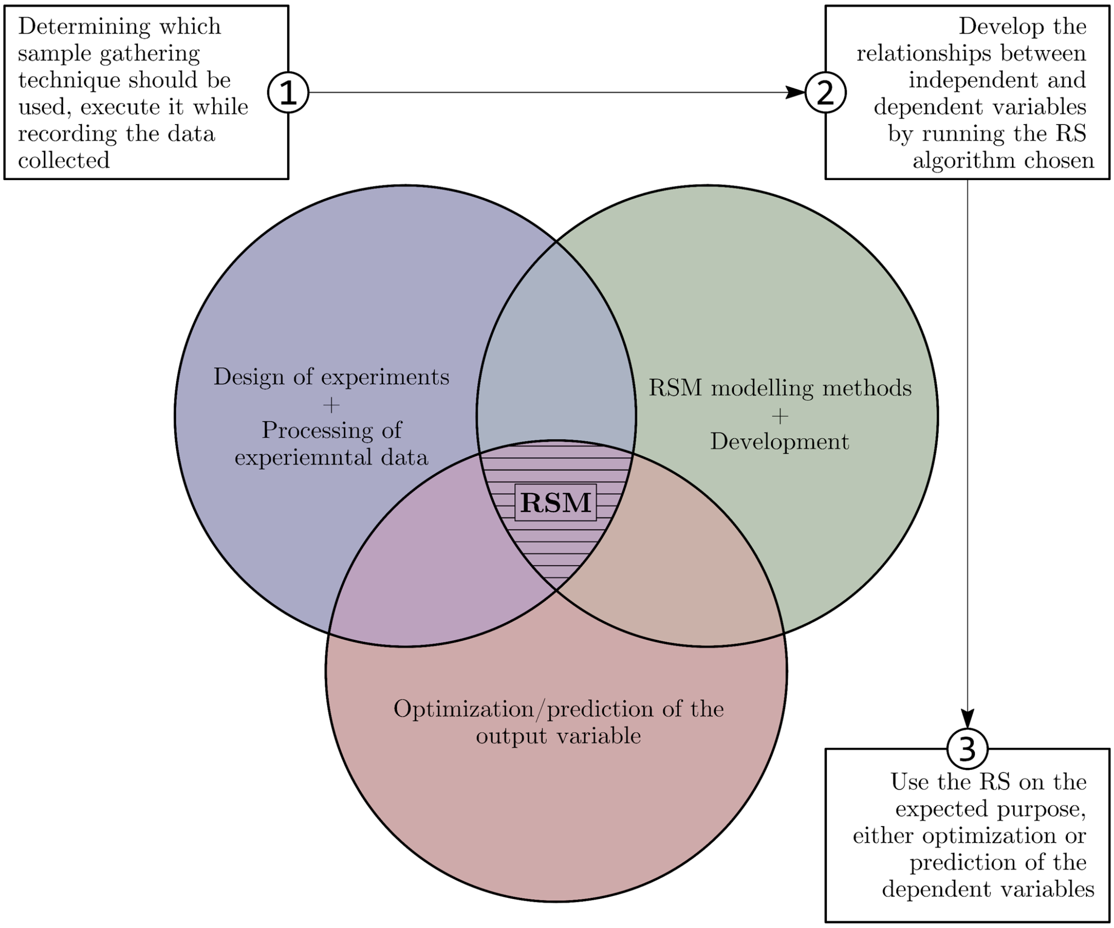

Figure 2.2: The summarized overview of using Response Surface Methodology (RSM) in engineering applications, presented as a schematic diagram, adapted from Oliveira et al. (2019)

2.2 State-of-the-art in surrogate modelling

As remarked in the preceding chapter, RSM is a versatile tool that can be used in numerous engineering applications, including the generation of SMs to aid optimization, design, and prediction tasks. While a substantial portion literature available is focused on the optimization aspect, this concise review attempts to isolate the specific and critical details pertinent to the prediction-based applications of SMs.

The SMs can be divided into three main categories based on their architecture, namely: (a) data-driven (response surface/statistical and black-box) SMs, (b) projection-based (reduced basis and model reduction) SMs, and (c) multi-fidelity based (hierarchical and physics-based) SMs (Asher et al., 2015). The SMs developed in this work will fall into the data-driven category, since the idea is to use a dataset with a number of sample points as the foundation of the model. Polynomial models (Liu et al., 2020), Gaussian processes and Kriging (Hoffer, B. C. Geiger, and Kern, 2022), radial basis functions (G. Chen et al., 2022), ANNs (Sun and S. Wang, 2019), and Bayesian networks (Lei et al., 2021) can be identified as some of the most popular data-driven SM methods. An overall process of developing a data-driven SM, applicable across any of these methodologies, can be observed in a review published by Queipo et al. (2005). The primary steps can be concluded as, (1) planning the DoE method and setting up the tools to collect the initial dataset, (2) selecting a sampling strategy and generating the initial sample set, (3) calculating the corresponding output variables and preprocessing the initial dataset, (4) selection of optimal input and output variables, sensitivity analysis, partitioning the initial dataset into training and testing subsets, (5) development of the surrogate model with the training subset, (6) testing the performance of SM with the testing subset, and lastly, (7) expanding the initial dataset and retraining the SM if the performance of the initial model deemed inadequate.

The prediction accuracy of data-driven SMs is dependent upon many factors such as the size and quality of the training dataset, and the nature of the physical phenomena being modelled (Breiman, 2001). A flawed implementation without considering the circumstances surrounding these factors can lead to unfavourable situations like overfitting, underfitting, and computationally costly calibrations (Razavi, Tolson, and Burn, 2012). Overfitting is a problem that arises with a sparse/not-complete, thus a generally weak training dataset. An overfitted SM is only accurate at the training data points while being loose and inaccurate at all other points. Underfitting occurs when the chosen SM is simply too weak to represent a relationship. For example, attempting to model non-linear shallow water behaviours with a linear regression method could lead to an underfitted SM. Overfitting and underfitting can be easily identified, and remedied by either improving the training dataset or changing the SM method. Razavi, Tolson, and Burn (2012) further states that, despite the widespread adoption of data-driven SMs, general optimization/prediction methods can be more effective than them under the right circumstances. Therefore, their suitability should be thoroughly assessed before use. This particular concern, however, holds limited relevance to this work context, as every single point predicted by the SM in mere moments will replace a fully-pledged CFD simulation that can span for several days. This renders the surrogate modelling approach unquestionably effective to achieve project objectives.

The literature on surrogate model development spread through more than four decades (Simpson et al., 2012). Table 2.1 summarizes a noteworthy few.

Table 2.1: Summary of the literature on some surrogate model development research and their important remarks

Source	Remarks
(Guerrero et al., 2018)	A surrogate model for naval architecture applications can be developed on a purely open-source setup. This is a promising prospect as potential licensing issues and availability issues that come with commercial software can be overridden.
(George, 2012) (Bai et al., 2019) (Harries and Uharek, 2021) (Hou and Behdinan, 2022)	The number of sample points demanded to ensure the accuracy of a surrogate, as well as the computational expenses of modelling exponentially increases with the number of input variables (design variables in optimization cases). Therefore, it is important to choose only the most important variables (dimensions) before generating the surrogate model. If the number of variables is still high, methods like principal component analysis can be applied to the dataset to reduce the dimensionality. Methods like Karhunen-Loève transformation (proper orthogonal decomposition) can project certain variables onto other variable spaces and reduce the number of variables.
(Barnes and McArthur, 2019) (Rehbach and Beielstein, 2019) (Corrales et al., 2022) (Zheng, 2022)	Using the proper independent/dependent variables combination can significantly improve the accuracy of a surrogate model. Feature expansion is a simple process of synthesizing all the possible combinations of a given variable set, under a predetermined order. • the second-degree feature expansion of x_1 and x_2 independent variables would be: x_1, x_2, x_1x_2, x_1^2, x_2^2. In other words, all the combinations x_1 and x_2 will have with under quadratic order • the third-degree feature expansion of x_1 and x_2 independent variables would be: x_1, x_2, x_1x_2, $x_1^2x_2$, $x_1x_2^2$, x_1^3, x_2^3. In other words, all the combinations x_1 and x_2 will have under cubic order Feature selection is a process that follows feature expansion, which can be used in conjunction with a variety of tools to select the most influential variables for the surrogate model. Some of the popular feature selection protocols are Pearsons coefficient, LASSO regularization, and feature selectors integrated with some surrogate methods like random forest selectors.

Continued on next page

Table 2.1 – continued from previous page

Source	Remarks
(Zitzler and Deb, 2000) (Bastin et al., 2013) (Yazdi and Salehi, 2014)	The concept of adaptive SMs is presented in these literature. Each study is conducted with its unique strategies to iteratively improve a base surrogate model by fine-tuning it. The overall mechanism should be involved with steps like improving the quality of the dataset, expanding the dataset, and integrating high-dimensional parameters such as gradients, or Hessians (gradient- or hessian-enhanced Kriging SMs). All in all, if the base SM developed needs improvements, the proposed methodologies from these studies can be utilized in the future.
(Moriasi et al., 2007) (Bennett et al., 2013)	Various criteria are available to test the accuracy of a developed surrogate model. Some of the most frequently used ones are (here $\hat{y}_i$ is the value predicted by the SM, y_i is the corresponding real value, $\bar{y}$ is the mean of real values). • Root Mean Square Error (RMSE) $\sqrt{\frac{1}{n}\sum_{i=1}^{n}\left(y_i-\hat{y}_i\right)^2}$ • Coefficient of Determination (CoD) (r^2) $1-\frac{\sum_{i=1}^{n}\left(y_i-\hat{y}_i\right)^2}{\sum_{i=1}^{n}\left(y_i-\bar{y}\right)^2}$ • Index of Agreement (IoAd) $1-\frac{\sum_{i=1}^{n}\left(y_i-\hat{y}_i\right)^2}{\sum_{i=1}^{n}\left(\lvert\hat{y}_i-\bar{y}\rvert+\lvert y_i+\bar{y}\rvert\right)^2}$ • Relative Absolute Error (RAE) $\frac{\frac{1}{n}\sum_{i=1}^{n}\lvert y_i-\hat{y}_i\rvert}{\frac{1}{n}\sum_{i=1}^{n}\lvert y_i-\bar{y}\rvert}$
(T. B. Bartz, 2021) (Kamath, 2022)	Almost all surrogate modelling methods possess architecture-level parameters that define their inherent characteristics. Tuning these hyperparameters (hyperparameter optimization) could enhance the performance of a surrogate model substantially. This could be potentially applied within the future workflow.

Figure 2.3 summarizes the performance of surrogate models developed in 20 different literature studies against the size of the training dataset. The performance of an SM is not solely dependent upon the size of the training dataset. Other factors like the real physical relationship between independent-dependent variables, the quality of the initial dataset, and SM method itself can also enhance or diminish the model's performance. Therefore, the graph intends to convey a primary idea of the relationship between the initial sample size and the surrogate performance. Further information for this analysis was gathered from some existing comprehensive reviews like Forrester and Keane (2009), Westermann and Evins (2019) and Alexiou et al. (2022).

As mentioned above, the primary aim of optimisation-focused SMs is not necessarily high prediction accuracy. These models function as intermediary tools that aid the optimization process (Mittendorf and A. D. Papanikolaou, 2021; Lin, He, and K. Li, 2018)[17, 14]. However, this is not valid for the case of surrogate models intended for prediction purposes, where the precision of the forecast is considered in high regard, depending on the project requirements (Yadav et al., 2018; Savasta and Sobey, 2021)[7, 20]. Although the number of sample points has no universal relationship with the performance – considering that some phenomena to be modelled can be simple and linear, while others can be complex and non-linear – it would be generally reasonable to anticipate that a larger sample set would substantially amplify the flexibility available to the model developer. This would likely improve the model's ability to capture the underlying patterns and complexities of the data, leading to better performance.

A study that centres on prediction-focused SM, conducted by Mittendorf (2023), bears notable similarities to the context of this work. It had been executed on the basis of predicting added ship resistance in waves. In their study, a significant initial data set of more than 500,000 samples were used from an already existing repository. However, in this work, it would be impractical to generate a sample set of that magnitude, while adhering to existing time constraints. As will be explained in the forthcoming chapter 4, even a simplified CFD simulation would take up to 48 h to reach full convergence. Thus, the goal would be to construct the SM using a manageable number of sample points, and then optimize it using the techniques listed in Table 2.1 until it meets the expectations of the MARISHALLOW sub-project of MARIDATA initiative.

One more important point highlighted is the frequency of SM methods used for naval architectural applications. Kriging- and ANN-based surrogate models are more frequently used than others. In this workframe, factors like uncertainty will not be considered, and supplementary data such as gradients and Hessians of the sample points are not currently planned to be incorporated, since the initial sample set will be limited in size. Therefore, it is noteworthy to mention that basic Kriging and ANN methodologies could be viable starting points.

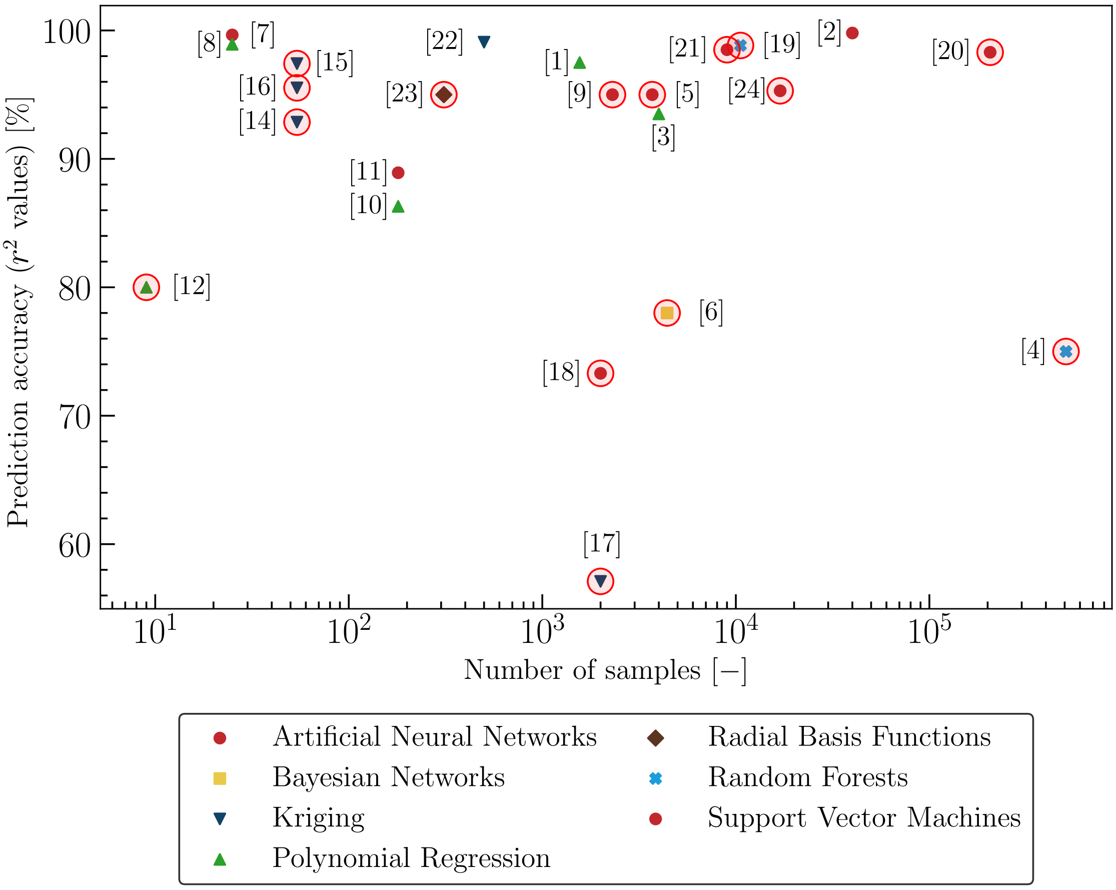

[1] (Nyshadham et al., 2019)
[2] (Balduin, Tröschel, and Lehnhoff, 2019)
[3] (Barnes and McArthur, 2019)
[4] (Mittendorf, Nielsen, and Bingham, 2022)
[5] (Milaković et al., 2020)
[6] (Montewka et al., 2013)
[7,8] (Yadav et al., 2018)
[9] (Segota et al., 2019)
[10,11] (Poorarbabi, Ghasemi, and Azhdary, 2020)
[12] (N. Papanikolaou and Anyfantis, 2022)
[13] (Rosenbaum and Schulz, 2012)
[14,15,16] (Lin, He, and K. Li, 2018)
[17,18] (Mittendorf and A. D. Papanikolaou, 2021)
[19] (Laurie et al., 2021)
[20] (Savasta and Sobey, 2021)
[21] (Petersen, Jacobsen, and Winther, 2012)
[22] (Masood, Khan, and Qian, 2021)
[23] (P. Wang, Z. Chen, and Y. Feng, 2021)
[24] (Grabowska and Szczuko, 2015)

Figure 2.3: General comparison of surrogate models developed in 20 literature studies, represented by the number of samples used for training vs. accuracy in Coefficient of Determination (r^2) values

Studies directly related to naval architectural context are highlighted with ⟨◉⟩

2.3 Methodology and work plan

From the comprehensive survey of literature covered in the previous Table 2.1, a basic framework for the surrogate generation process can already be established. The initial step would be generating a high-quality dataset that the surrogate model can operate on. The selection of appropriate independent variables can be carried out with the aid of a single or a combination of feature selection methods. Transforming the distribution of the dependent variables (in the training dataset) into a Gaussian normal distribution can improve the accuracy of the SM. Hyperparameters of the surrogate method can be tuned to improve performance. The performance can be measured through one of many accuracy measuring criteria. Overall, the whole process could be adapted into an iterative loop that can improve performance with each step. Figure 2.4 summarized this framework as a workflow that will be used to develop the base surrogate model from scratch. The end outcome would be a standalone surrogate model that can predict the added resistance in shallow water with satisfactory accuracy. Within the context of this report, this model is referred to as the base or phase-I surrogate model.

After the successful execution of the complete workflow related to phase I, an extension for the project scope is proposed in Figure 2.5. The extension is involved with developing a self-improving iterative loop so the base SM can iteratively improve in accuracy. The logic behind this loop will be generating a small set of new samples at each iterative step, calculating the added resistance for them, and appending them to the existing training dataset. The slightly expanded new training dataset will then be used to redevelop (retrain) the surrogate model. When this cycle is executed over and over, the surrogate model will continuously improve in accuracy. In order to make it automated, the main loop will be developed inside a Python environment, containing a sub-loop that can access the High-Performance Cluster (HPC), launch the CFD simulations, and extract their results back into the local machine. As will be discussed in section 4.1, HPC is a remotely located, specialized computing system designed to handle complex and computationally intensive tasks. It consists of multiple interconnected processing units or in other words, computers (nodes), that can work in parallel to solve large-scale computational problems like CFD simulations. The sub-loop will be developed as a shell script written with `BASH` language used with Ubuntu. Unless otherwise stated, the surrogate development process will be coded in a `Python 3.11.2 64-bit` environment. The resistance calculation tasks will be executed through the open-source numerical solver `OpenFOAM`.

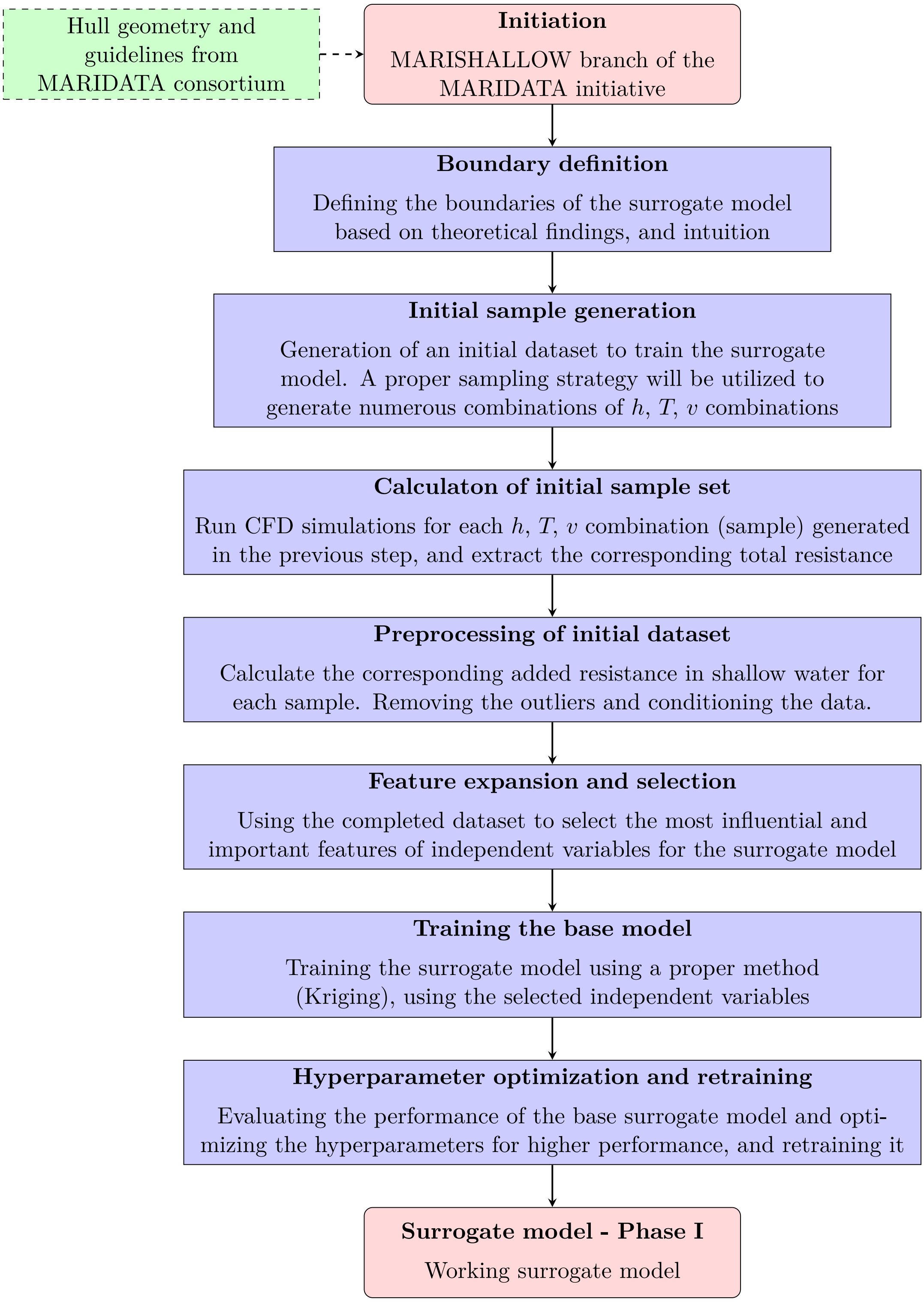

Figure 2.4: Flowchart for the development of the surrogate model with the adoption of numerous tools identified in the state-of-the-art survey

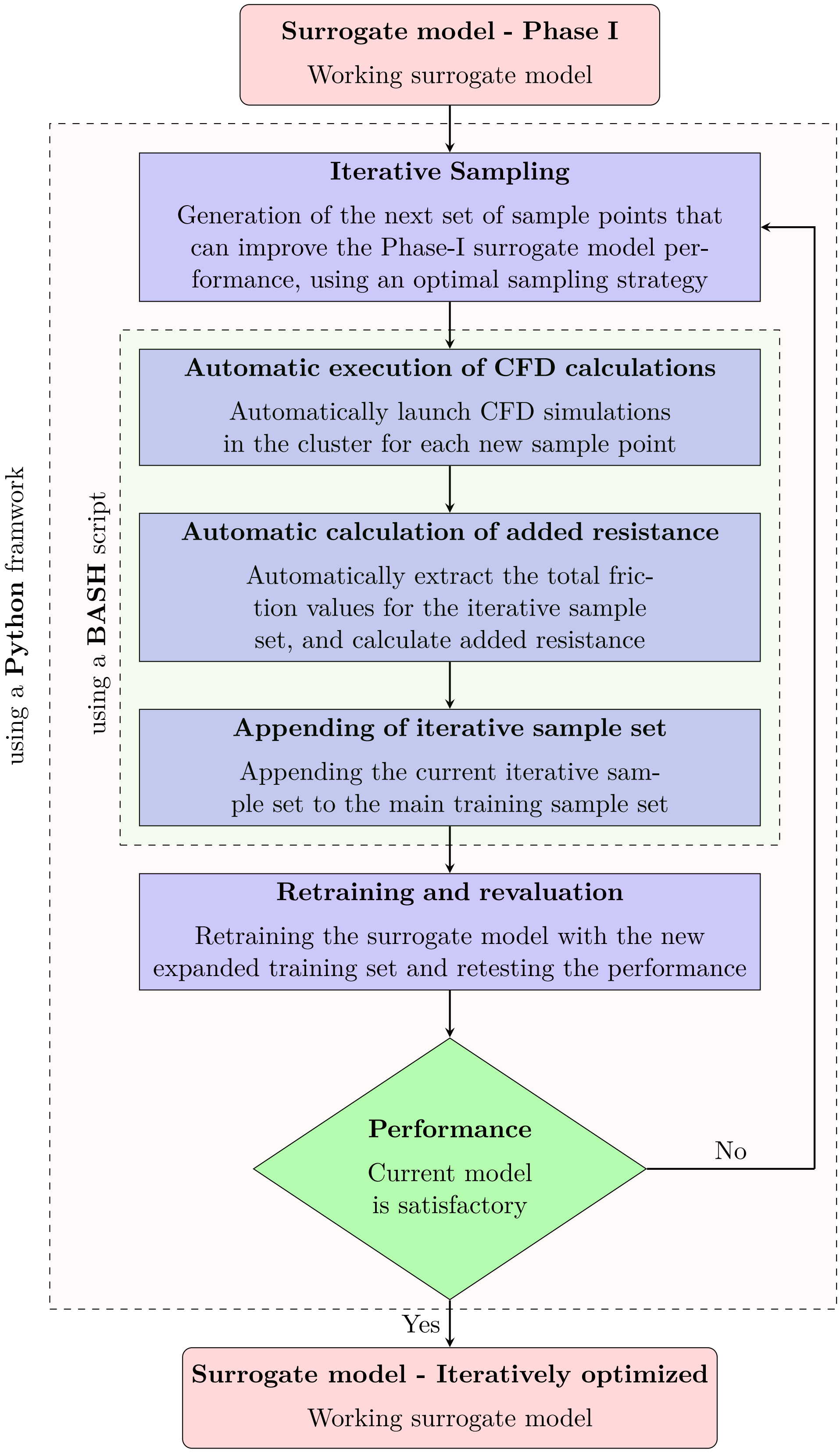

Figure 2.5: Flowchart of the iterative loop to enhance the performance of the base surrogate model

CHAPTER

Ship Resistance and shallow water hydrodynamics

3

The chapter is dedicated to exploring the hydrodynamic phenomena associated with ship resistance and effects of water depth on vessel performance.

3.1 Fundamentals of hydrodynamics

The field of fluid dynamics aims to provide the means to comprehend the behaviour of fluids in motion. Among the three main forms of matter; solids, liquids, and gases, the latter two fall into the category of fluids. The fluid motions in a Newtonian physical frame are governed by underlying principles like the conservation of mass, momentum, and energy. Evidence has been uncovered that prehistoric civilizations utilized fluid properties on hydraulic systems and distribution networks through more pragmatic approaches. More modern and scientific perspectives on fluid behaviour have emerged with Archimedes's hydrostatic laws remarking as one of the most important discoveries up to date when it comes to the field of engineering. Some notable publications such as *"Hydraulics"* (1737) by Johann Bernoulli, *"Hydrodynamica"* (1738) by Daniel Bernoulli, and *"Trait'e des fluides"* (1744) by d'Alembert succeeded in systematically conveying the theories of early fluid dynamics to the outside world and many of those findings still stand up to date (Birkhoff, 1983).

The contemporary hydrodynamic aspect is built on a series of vastly distinguishable theoretical pillars. Each pillar is developed upon different assumptions and thus has its own ebbs and flows. A few major pillars can be identified as, Bernoulli's principle, Euler-Lagrange formulation, Navier-Stokes equations, Potential theory, Archimedes' principle, boundary layer theory, and Computational Fluid Dynamics (CFD). Depending on the nature of the problem, resources available and the constraints invoked, the engineers are free to choose between any of these approaches, or even to use multiple of them in unison for separate domains of the same problem. A couple of frequently applied principles in marine engineering/ naval architecture context are briefly described as follows (R. W. Johnson, 1998).

3.1.1 Euler-Lagrange equations

The Euler-Lagrangian formulation is used to synthesise equations of motions of a physical system. These second-order ordinary differential equations combine two important explanations of classical mechanics to describe the motion of fluid particles and fluid flows in physical space. The Eulerian description explains the particle behaviour by observing local regions of the fluid flow (Figure 3.1b). Therefore, it can be used for more localized analyses of the fluid flow, for instance; the interaction with complex surfaces on a ship hull, or ship propellers. The Lagrangian description on the other hand explains the motion of individual fluid parcels of fluid particles in a fluid flow by observing the trajectory of the through time (Figure 3.1a). Therefore, to observe how a fluid stream or a wave can be affected by solid objects like a hull over time, the Lagrangian approach can be used. The Lagrangian definition for the initial position of a particle at initial time point t_0 can be defined as (Birkhoff, 1983; Constantin, 2008),

$$x(\vec{x}_0, t_0) = \vec{x}_0 = (x_0, y_0, z_0) \tag{3.1}$$

Therefore, by expressing the position ($\vec{x}$), velocity ($\vec{v}$) and acceleration ($\vec{a}$) of the particle as functions of initial position and time, the temporal propagation of the particle in physical space can be represented as follows,

$$\vec{x} = \vec{x}(\vec{x}_0, t) = \vec{x}(\vec{a}, t) \quad \text{and} \quad \vec{v} = \vec{v}(\vec{x}_0, t) \quad \text{and} \quad \vec{a} = \vec{a}(\vec{x}_0, t) \tag{3.2}$$

The Lagrangian definition of particle motion can be integrated with the Eulerian definition with the operator called material derivative. If $\vec{G}(\vec{x}, t)$ is a property of the fluid, the material derivative of that property can be expressed as,

$$\underbrace{\frac{D\vec{G}}{Dt}}_{\substack{\text{Lagragian}\\ \text{rate of change}}} = \underbrace{\frac{\partial\vec{G}}{\partial t}}_{\substack{\text{Eulerian}\\ \text{rate of change}}} + \underbrace{\vec{v}\cdot\nabla\vec{G}}_{\substack{\text{Convective}\\ \text{rate of change}}} \tag{3.3}$$

Similarly, numerous fluid properties like velocity, acceleration, density or even temperature can be represented with the material derivative.

The Euler-Lagrange equations are valid only for the domains of inviscid, incompressible fluids. Due to the combination of properties of Eulerian and Lagrangian formulations, they can be well applied in operations like hull optimization for wave interactions, or local system design (propulsion system), but fall short when it comes to calculating the resistance of a ship. The frictional resistance will entirely be neglected and the results would be significantly erroneous.

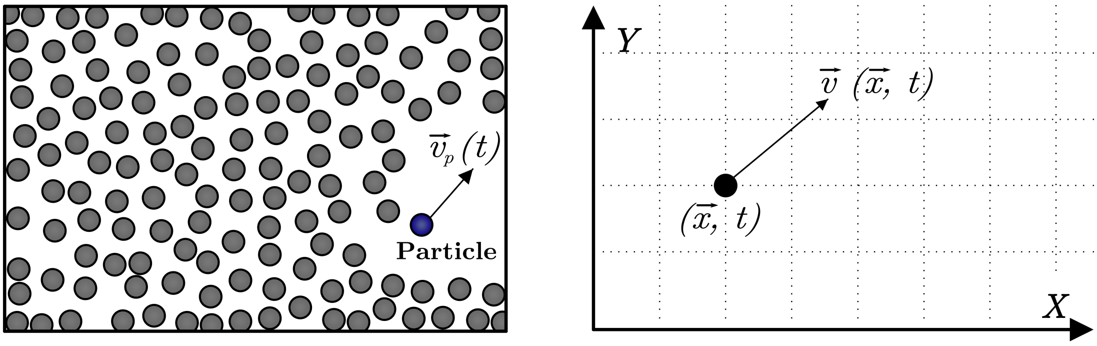

(a) Lagrangian definition *(b) Eulerian definition*

Figure 3.1: The distinction between Lagrangian and Eulerian definitions of fluid motion, (a) The Lagrangian definition uses motion equations in classical mechanics to define the motion of a particle or a fluid parcel along its trajectory,

(b) The Eulerian definition focuses on fixed points in a fluid flow and defines the motion of the flow passing those points (**MIT**, 2006).

3.1.2 Potential flow theory

Currently used in a plethora of practical applications, the potential flow theory also assumes an idealized state of fluids, which is inviscid, irrotational and incompressible. However, the theory can be closely correlated with numerous fluid dynamic phenomena taking place in the real world. The behaviour of water particles in a deep sea wave could be taken as an example. Another application of potential flow theory emerges when evaluating flow behaviours around bodies. When a body is smooth and streamlined, the boundary layer formed is thin enough for the potential assumptions to be valid. When the body is rough and complex, the boundary layer thickens and flow becomes more susceptible to adverse phenomena like flow separation. This eventually renders the potential flow theory inapplicable, unless a workaround is used, such as applying the potential theory outside the boundary domain and adding corrections to the final results within it.

The potential flow theory is used in a wide range of applications in the naval architecture context. The simplified solutions for potential equations can lead to significant time savings when simulating manoeuvring trajectories, seakeeping characteristics, motion in waves, and even pressure resistance. To calculate the total resistance, some potential flow solvers are coupled with viscous solvers, or the pressure resistance component calculated by a potential solver is added to the viscous friction component approximated using empirical formulations like the 1957 empirical friction formulation from ITTC (Janson and Larson, 1997; Sulovsky et al., 2023). This leads to faster calculations (approximations) of ship resistance and ship motion characteristics, making potential flow theory an ideal candidate for iterative hull optimization processes. However, for a ship sailing in shallow water, potential flow solutions based on inviscid, irrotational assumptions will not capture the complex boundary layer or vortices generated in the narrow passage between the hull bottom and river or ocean bed. Thus, another option was sought to calculate the resistance.

The potential (velocity potential) is a scaler function that describes the velocity of a fluid at any point of flow. When the potential is signified as $\phi(x, y, z)$, the velocity components can be calculated by respective gradients in each direction. u, v and w are velocity components of the fluid particles along the x, y, and z directions. Since the velocity field is derived from this scaler potential, further calculations are greatly simplified (Larsson et al., 1999).

$$u = \frac{\partial \phi}{\partial x} \quad \text{and} \quad v = \frac{\partial \phi}{\partial y} \quad \text{and} \quad w = \frac{\partial \phi}{\partial z} \tag{3.4}$$

Considering the conservation of mass, the velocity field adheres to the Laplace equations, as shown in the following equations.

$$\begin{aligned} & \frac{\partial u}{\partial x} + \frac{\partial v}{\partial y} + \frac{\partial w}{\partial z} &&= 0 \\ & \frac{\partial^2 \phi}{\partial x^2} + \frac{\partial^2 \phi}{\partial y^2} + \frac{\partial^2 \phi}{\partial z^2} &&= 0 \\ \text{Laplace Equation} \quad \Rightarrow \quad & \nabla^2 \phi &&= 0 \end{aligned} \tag{3.5}$$

3.1.3 Navier-stokes equations

Named after two physicist/mathematicians set apart by several decades (Claude-Louis Navier (1822) and George Gabriel Stokes (1842-1850)), Navier-Stroke equations basically extend the Euler equations by considering the effects of fluid viscosity. Therefore, the underlying theories (mass/momentum conservation) and the operation of Navier-Strokes partial differential equations are quite similar to the Eulerian model. The whole model can be broken down as follows,

- Independent variables: the coordinates (x, y, z) that describe the spatial representation of fluid particles or flow and time (t) that describe the evolution of fluid motion.
- **Dependent variables:** represent the properties of the fluid itself, such as; pressure (p), density (ρ), and temperature (T) and three velocity components long $x, y,$ and Z directions, respectively $(u, v, and\, w)$.
- Continuity equation: this time-dependent equation validates the conservation of mass in the fluid flow.
- Conservation of momentum equation: derived by applying Newton's second law of momentum to a finite fluid volume, taking into account the body and surface forces applied on that volume. The unified action of surface and body forces is equalized to the rate of change of momentum.
- Conservation of energy equation: reflects the mathematics behind the first law of thermodynamics by relating the independent temperature variable with the internal energy of the fluid. The total energy of the fluid is equalized to the heat transfer amount to and from the fluid and the work done by body/surface forces.

A simplistic representation of Navier-Strokes equations is given with the following equations (Marion and Temam, 1998). Here, $\vec{V}$ is the vector of three velocity components $[u, v, w]$, $\vec{g}$ is the gravitational acceleration, ρ is the density of the fluid, ∇p is the pressure of the fluid, and t is the time.

$$\begin{aligned} \text{Continuity equation} \quad &\Rightarrow \quad \nabla \cdot \vec{V} &&= \quad 0 \\ \text{Momentum equation} \quad &\Rightarrow \quad \underbrace{\rho \left(\frac{\partial \vec{V}}{\partial t} + \vec{V} \cdot \nabla \vec{V} \right)}_{\substack{\text{Material} \\ \text{derivative}} = \frac{D\vec{V}}{Dt}} &&= \quad -\nabla p + \rho \vec{g} + \mu \nabla^2 \vec{V} \end{aligned} \tag{3.6}$$

A smooth analytical solution for the general form of Navier-Strokes equations is still absent. Numerous forms of derivations with various assumptions (laminar flow, incompressible fluid, two-dimensional flow, etc.) are used in reality with exact solutions of their own. These solutions are calculated numerically with discretized fluid domains with the method known as Computational Fluid Dynamics (CFD) (Langtangen, 2012). As an advanced extension of Eulerian equations with the capability of considering the viscosity and compressibility of fluids, the Navier-Strokes equations, in general, are able to capture intricate behaviours of fluid flows more accurately compared to Euler-Lagrangian equations or the potential flow theory.

3.2 Hydrodynamics of ship resistance

Just like other resistance forces, the ship resistance also acts opposing to the motion of a marine vessel. The forward motion of the ship is mainly considered when sizing the propulsion system and powering requirements at the design stages. After all, a ship would be predominantly traversing forward during its operational phase. Moreover, a ship's speed is highest in its forward motion, leading to the highest resistance. This underlines the general fact that the speed of an object is always positively correlated with the resistance it encounters. An accurate estimation of resistance at the ship designing stage and tailoring of the ship hull and propulsion train is now more important than ever, due to rising concerns regarding marine emissions, fuel costs and the overall sustainability of the maritime industry.

Although the project scope is focused solely on the forward resistance, the resistance components opposing other motions like heave, pitch and yaw are also important when it comes to manoeuvring and seakeeping analyses. A marine vessel floating standstill on the water only experiences the hydrostatic pressure to be buoyant. However, when a relative motion is invoked between the ship and the water, numerous other force components start to appear, due to factors like viscosity, hydrodynamic pressure, fluid-structure interaction, and added mass. Resistance is a force generated due to this. The total resistance on a ship is a collective superposition of some of these force components. In other words, the resistance on a marine vessel can be decomposed into multiple components.

3.2.1 Components of ship resistance

In classical hydrodynamics, a body fully submerged in an inviscid fluid would experience no opposing force while moving (D'Alembert's paradoxon (Bertram, 2012, p. 66)). However, in reality, idealised non-viscous fluids are non-existence, and a body moving through them would experience frictional and pressure resistance forces opposing its motion. Also, the moving body pushes fluid volumes in front of it away, causing disturbances. These disturbances lead to pressure variations acting on the fluid, and on the body itself as reactions. These variations are manifested in a way that the pressure in front of the moving body is higher than the pressure in the trailing side (a pressure gradient decreasing in the opposing direction), generating an additional pressure force opposing the motion. When the submerged body is located close to the fluid surface, the pressure variations caused by its motion can disturb the free fluid surface, making elevations and depressions, essentially forming a wave pattern. This wave pattern seems to be radiating from the moving body, adding another force component to the total resistance. In the case of a ship that is not fully immersed in water, the free water surface is directly disturbed not only by the pressure variations but also by the hull itself, leading to more pronounced wave generation. In the presence of already disturbed waters (by natural waves or other ships passing by), more resistance components come into play. However, only the resistance in calm water conditions is considered in this thesis. The decomposition of ship resistance is depicted by its major components in Figure 3.2.

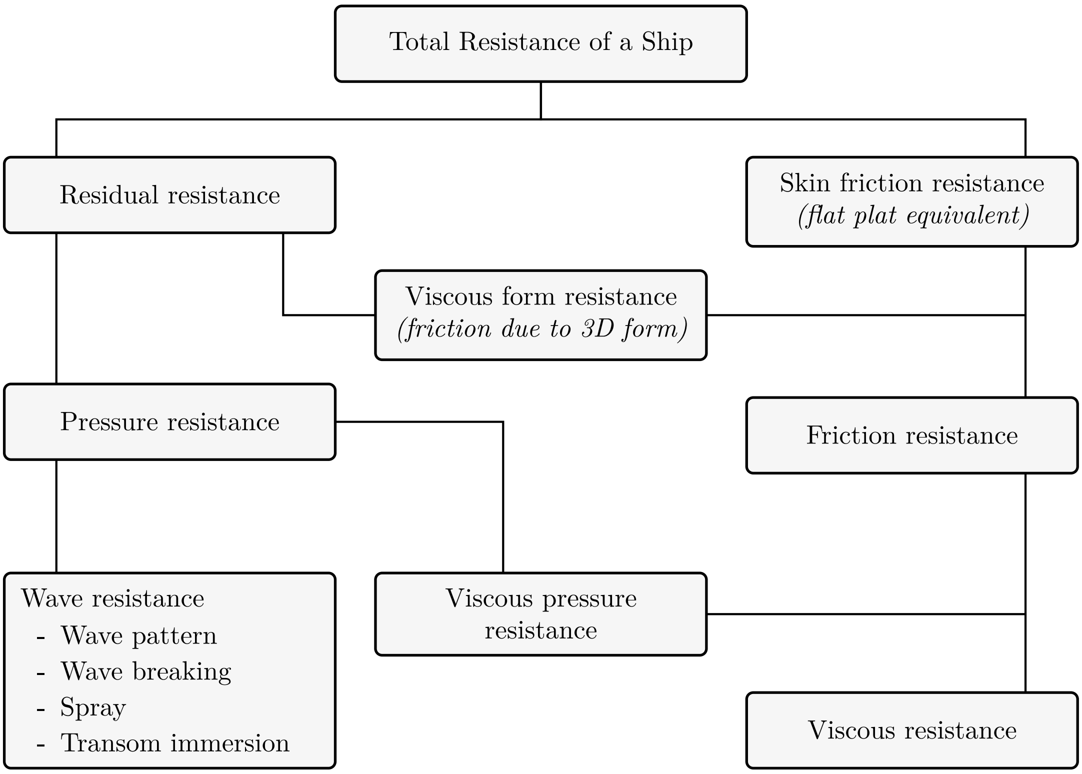

Figure 3.2: Major components of decomposed ship resistance from a hydrodynamical point of view. The aerodynamic resistance on the above waterline portion is also applied on a ship, but not significant compared to its hydrodynamic counterpart (Bertram, 2012)

3.2.1.1 Skin friction resistance

The particles of a viscous fluid tend to "cling" onto any solid surface passing by them since the viscosity provides frictional properties to the fluid. The clinging effect is highest at the solid surface but progressively fades to zero when the distance to the object increases. The region between the solid surface (hull surface) to undisturbed fluid (generally defined from where fluid particles have 99% of undisturbed velocity) is called the boundary layer (Hauke, 2008, p. 197).

Fluid particles right on top of a hull surface are assumed to have fully adhered and moved along with it (the wall boundary condition). The wall fluid layer tags the adjacent fluid layer along. However, the speed would be decreased (slip will be there) since the fluid-fluid viscous adhesion is not as strong as fluid-solid adhesion. This pattern continues up to the boundary region, resulting in fluid volumes with reducing layer speeds, pulled by the moving solid object (ship). A portion of the ship's propulsion power is expended to pull the large volume of water virtually enclosed by the boundary layer. Simply, when the viscous shear stresses are integrated over the submerged surface (wetter surface) of the hull, skin friction resistance is yielded (Figure 3.3). The magnitude of skin friction drag can depend upon multiple factors.

- Viscosity: Viscosity is the main reason for fluids to have friction properties, thus the skin drag increases with it.

- Relative velocity between fluid and object: The shear stresses increase intensively when the relative motion between the wall and fluid is increased. Generally, it is assumed that skin friction drag is proportional to the square of relative velocity.

- Surface area of the body: The magnitude of the skin friction drag is directly proportional to the surface area of the body in contact with the fluid.

- Surface roughness: When the surface is rougher, the adhesion effect increases and the skin drags along with it. A perfectly smooth hull would experience zero skin drag even in a viscous fluid. This ideal situation does not occur in reality.

- Reynolds number (Re): Reynolds number is a dimensionless quantity that represents the ratio between inertial forces and viscous forces of flow. When a ship hull is slowly moving with a low Reynolds number, skin friction drag is said to dominate other drag components discussed later in this section (Soares, 2015, p. 24). This is in spite of the fact that low Reynolds numbers are associated with laminar flows, which inherently generate less skin friction than turbulent flows. However, due to the large wetted surface area, the magnitude of skin drag remains significant.

$$Re = \frac{\text{Inertial forces}}{\text{Viscous forces}} = \frac{\rho v L}{\mu} = \frac{1020 \times 192}{9.8 \times 10^{-4}} = 1.99 \times 10^{8} \tag{3.7}$$

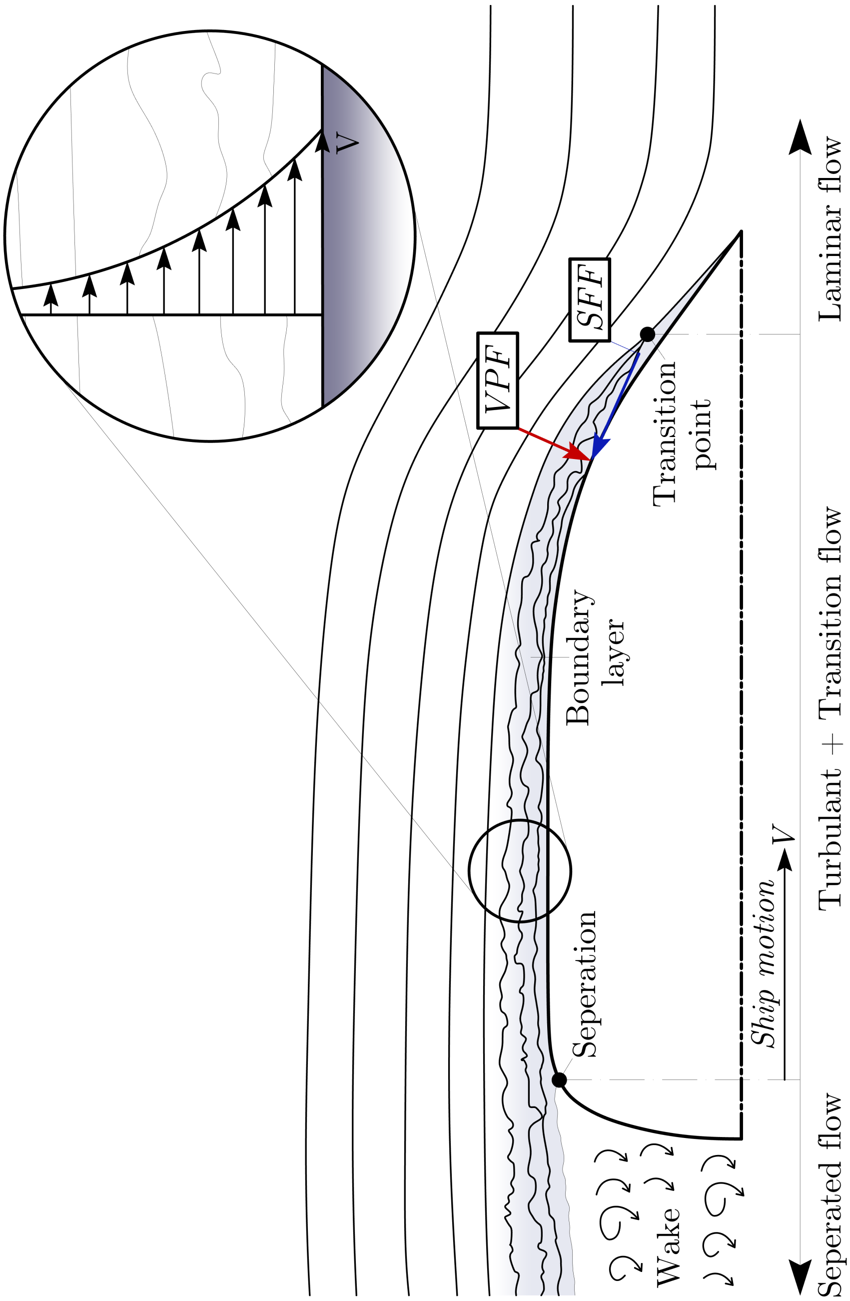

Figure 3.3: Development of the boundary layer along a forward-moving ship hull, its transition from laminar to turbulent states and how skin friction (⟶) and viscous pressure (⟶) resistance components are generated, inspired by Molland, Turnock, and Hudson (2017)

3.2.1.2 Viscous form resistance

The skin friction resistance consists of two components, namely, the 2-dimensional (2D) and 3-dimensional (3D) components. If a flat plate with the same surface area as the wetted surface of the hull is placed parallel to the flow, it would experience friction equivalent to the 2D friction component of that hull. Since the hull is not entirely flat, but made of complex curvatures and geometries, a correction should be added on top of the 2D friction. This 3D correction, known as the effects of hull form on viscous resistance, accounts for several factors.

- When the hull surface is not parallel to the forward ship direction, the entirety of tangential shear forces are not acting as resistance. Instead, a fraction of the tangential shear should be considered for the resistance.

- Curvatures of the hull cause local pressure variations on the flow, accelerating or decelerating it at different points. Since the skin friction is proportional to velocity (square of velocity in general), a 3D hull would experience a different resistance than a flat plate.

3.2.1.3 Viscous pressure resistance

A boundary layer developed around a hull can cause pressure variations. These pressure variations act simultaneously with the tangential shear stresses developed due to friction. However, they act normally on the hull surface instead of being tangential. Since the hull takes a complex 3D curvature, a component of them can act parallel to the ship's motion direction (just like in the viscous form case). When the boundary layer is displaced by the forward-moving fore section, pressure there would be higher than that of the stern portion, leading to a pressure imbalance. Therefore, the resultant pressure components would manifest into a net resistance against the forward motion.

3.2.1.4 Wave resistance

As described in the aforementioned sections, the ship hull moves forward by pushing a volume of water away from the bow. Subsequently, the stern "moves away" from the water, leading to increased and decreased pressure regions at the bow and stern respectively. These pressure variations ultimately form a wave system that deforms the free water surface. This phenomenon can be described by re-imagining the ship hull as a pressure point moving along the free surface. Basically, the wave system of the superposition of two transverse and divergent wave series. This whole ship wave (wake) generation was explained by Lord Kelvin who also highlighted the fact that diverging waves are always arranged 19.5° with respect to the ship centerline (Dias, 2014; Darmon, Benzaquen, and Raphaël, 2014). Interestingly, this angle norm does not hold for ships in shallow water. The total wave resistance is a representation of propulsion energy dissipated to create, maintain and carry this wave system (Figure 3.4a). The transverse wave series with troughs and crests contribute mostly to wave resistance. The main components of wave resistance are described below (Molland, Turnock, and Hudson, 2017).

- Wave pattern component is commensurate with the shape, size and movement speed of the waves generated by the hull.

- Wavebreaking resistance is generated when individual waves become too steep to stay stable, and ultimately break against the hull.

- Spray component describes how small water volumes are parted off and thrown against the hull, hindering its forward motion.

- The transom sterns of most modern ships can disrupt the flow that comes out from underneath the hull, forcing it to separate. Part of the separated flow turns into eddies and vortices that try to hold the hull back and affect the wave pattern (Figure 3.4b).

3.2.2 Representing resistance as dimensionless coefficients

Resistance coefficients are dimensionless quantities frequently used to represent ship resistance. These coefficients apply a degree of standardization to the ship resistance for different ships, making it easier to compare the values. Each resistance component can be represented as its own coefficient. In order to nullify the units corresponding to force ($[N]$ in SI form) the respective resistance component is divided by a combination of prominent factors that affect the resistance; generally, velocity (v), surface area (mostly Wetted Surface Area (WSA) or midship area of the hull ($A_{Midship}$)), and density of water (ρ). Given that the prospective surrogate model is intended for a single ship, representing the output variable as the coefficient of added resistance in shallow water is mandatory, albeit feasible. The decision to use either the coefficient or added force itself will be taken later. If we define the wetted surface area as S,

- the coefficient of total resistance,

$$C_T = \frac{R_T}{1/2\rho S v^2} \tag{3.8}$$

- the coefficient of residual resistance,

$$C_R = \frac{R_R}{1/2\rho S v^2} \tag{3.9}$$

- the coefficient of viscous resistance,

$$C_F = \frac{R_V}{1/2\rho S v^2} \tag{3.10}$$

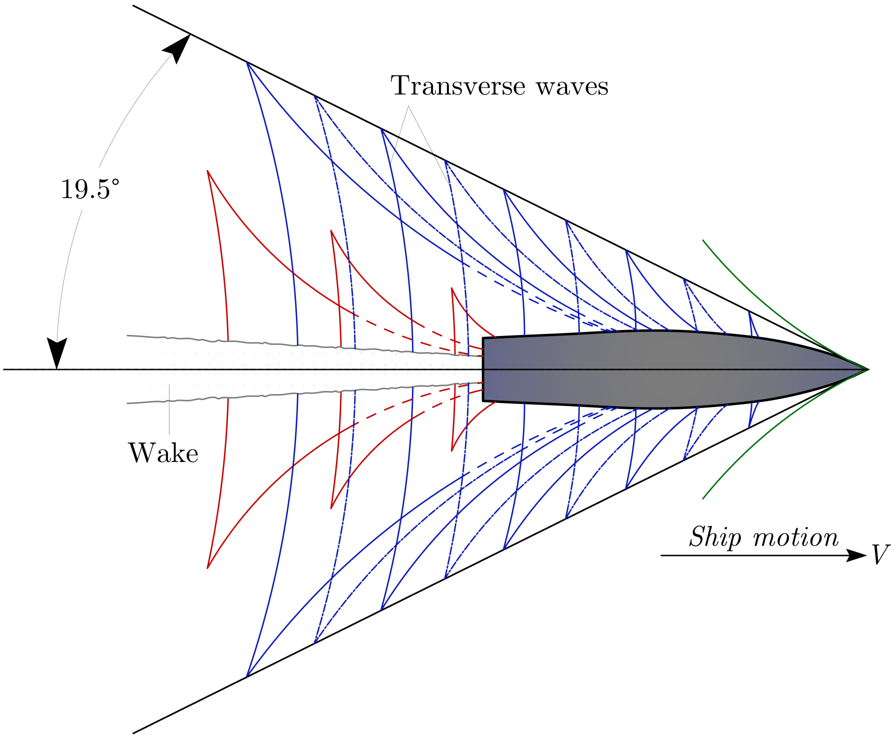

(a) *Generation of the wave profile with; (—) Bow wave, (—) Diverging wave crests, (- - - -) Diverging wave troughs, (—) Stern waves*

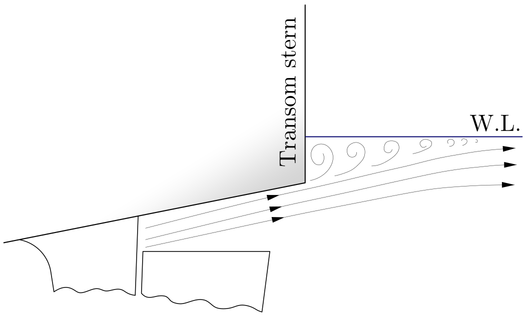

(b) *Transom immersion*

Figure 3.4: Components of the wave resistance,

(a) generation and arrangement of the hull wave system considering hull as a combination of two moving pressure points, inspired by Molland, Turnock, and Hudson (2017),

(b) Generation of vortices due to the flow separation caused by an immersed transom (Carlton, 2007)

As described by the Figure 3.2, the primary resistance components add up as the total resistance acting on the hull. The residual resistance is the combination of wave, viscous pressure, and viscous form components. It should be noted that there are other primary resistance components than the ones described above; such as the appendage resistance generated by auxiliary components attached to and protruding out of the naked hull (parts like rudders or bilge keels). These resistances are also subdivided into viscous and pressure components and added to the total resistance.

The total resistance (R_T) can be expressed with a linear combination of viscous resistance (R_τ), vortex resistance (R_{VT}), wave resistance (R_W) and residual resistance (R_R) as follows.

$$R_T = R_\tau + R_{VT} + R_W = R_\tau + R_R \tag{3.11}$$

Multiple experimental and analytical studies carried out by Abdulkareem, Tech, and Gotman (2002) and Weinblum et al. (1952) concluded that all the above resistance components in Equation 3.11 can be independently calculated. The direct proof of these findings can be seen in the studies of Baba (1969). This independency can be greatly beneficial to the future analyses since it allows for the effective analysis of individual components when deciding the optimal parameters (design parameters) for the surrogate model.

3.3 Effects of shallow water on ship resistance

Up until this point in the chapter, the generation of ship resistance has been addressed from a broad perspective. This 'general' view primarily encompasses operational conditions encountered by oceangoing ships in the majority of their life cycle where the water depth is substantially greater than the draft of the ship, and the waves encountered are irregular, corresponding to typical sea states, etc. However, it is likely that a ship would encounter operational conditions that are completely deviated from the general conditions. In such occasions, the underlying hydrodynamic principles will still remain valid, but the outcomes may not be as straightforwardly predictable. Such non-general scenarios include the events of extreme weather, unusually rough or turbulent waters, or the premise of the work discussed in this thesis, shallow water in regions such as tidal estuaries and rivers.

3.3.1 Definition of shallow water

Primarily, shallow water is defined when the water depth in the ship's path is not significantly higher than the ship draft. Therefore, the bottom of the ship hull will be in closer proximity to the solid bottom of the waterbody or the waterway. Numerous alterations in the hydrodynamic behaviours occur when a ship enters a shallow water region that will affect the ship's performance in turn. The exact boundaries of shallow water are set by different criteria by different researchers.

- According to PIANC (1992), four different water depth conditions can be defined by the ratio between water depth and ship draft.

deep water	$h\,/\,T > 3.0$
medium-deep water	$1.5 < h\,/\,T < 3.0$
shallow water	$1.2 < h\,/\,T < 1.5$
very-shallow water	$h\,/\,T < 1.2$

- According to Lewis (1989), the shallow water is defined when $h\,/\,T < 3$. This definition agrees with the above one.

- The International Towing Tank Conference considers that a ship will start to experience shallow water effects when the depth-to-draft ratio is less than five ($h\,/\,T < 5$) (ITTC, 2008)

3.3.2 Hydrodynamic changes in shallow water

The importance of considering the finite depth effect for the ship resistance problem was emphasized in early studies such as Graff (1964) and Tuck (1966). They have identified that restricted water depths can have obvious adverse effects on ship resistance. To describe the shallow water effects on a ship, the nominal velocity-based Froude number (Frv), as well as an additional form of Froude number based on water depth (Frh), are used. The following equation describes both Froude numbers and their exact values for the reference ship (Table 4.1) considered, for design velocity ($15\,kn$) and 30 m water depth.

$$\begin{aligned} &\text{Velocity-based Froude number} \quad \Rightarrow \quad \frac{V}{\sqrt{gL}} = \frac{5.4017}{\sqrt{9.81 \times 192}} = 0.1245 \\ &\text{Depth-based Froude number} \quad \Rightarrow \quad \frac{V}{\sqrt{gh}} = \frac{5.4017}{\sqrt{9.81 \times 30}} = 0.3154 \end{aligned} \tag{3.12}$$

The shallow water hydrodynamic transformations associated with ship resistance can be described as follows:

- Modification of the flow due to under hull clearance: the definition suggests that the clearance between the hull and the seabed (or floor of the waterbody) is severely restricted in shallow water conditions. When the flow is forced to pass under this narrow passage, its velocity increases compared to the deep passage available in deep water conditions. Therefore, the relative velocity between the under hull flow and the ship -one of the prominent factors contributing to skin friction drag (Section 3.2.1)- increases.
- The increased velocity under the hull leads to a pressure drop, and the ship tends to sink further. This phenomenon is known as ship squat.
- Since the seabed acts as a no-slip wall, the under-hull boundary layer is forced to end right on top of it. Also, due to the limited clearance, it will be thinner, resulting in a steeper velocity gradient. This in turn would increase the skin-friction drag further (Gourlay, 2014).
- The typical Kelvin wave pattern demonstrated in Figure 3.4a also changes form in the presence of shallow water. Due to the interaction with the closely located seabed, the waves grow higher in amplitude. To generate these increased energy waves, a ship has to disperse a higher portion of its propulsion power, leading to increased wavemaking resistance. The deformations corresponding to particular depth-Froude numbers are depicted in Figure 3.5.

The shallow water resistance of a ship can be explained under 3 distinct depth-based Froude number regions (Zhao, 1984).

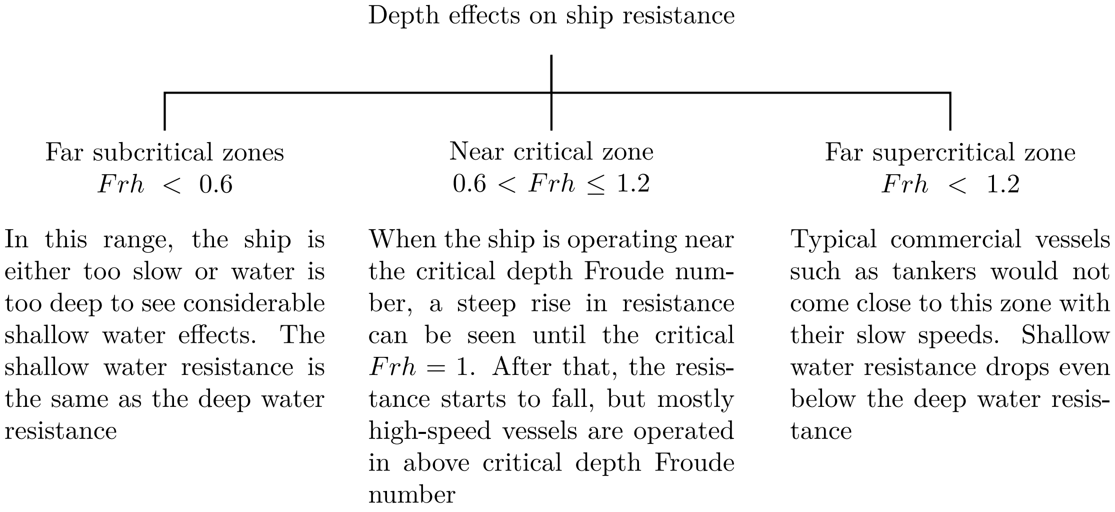

Depth effects on ship resistance

Far subcritical zones
$Frh < 0.6$

In this range, the ship is either too slow or water is too deep to see considerable shallow water effects. The shallow water resistance is the same as the deep water resistance

Near critical zone
$0.6 < Frh \leq 1.2$

When the ship is operating near the critical depth Froude number, a steep rise in resistance can be seen until the critical $Frh = 1$. After that, the resistance starts to fall, but mostly high-speed vessels are operated in above critical depth Froude number

Far supercritical zone
$Frh < 1.2$

Typical commercial vessels such as tankers would not come close to this zone with their slow speeds. Shallow water resistance drops even below the deep water resistance

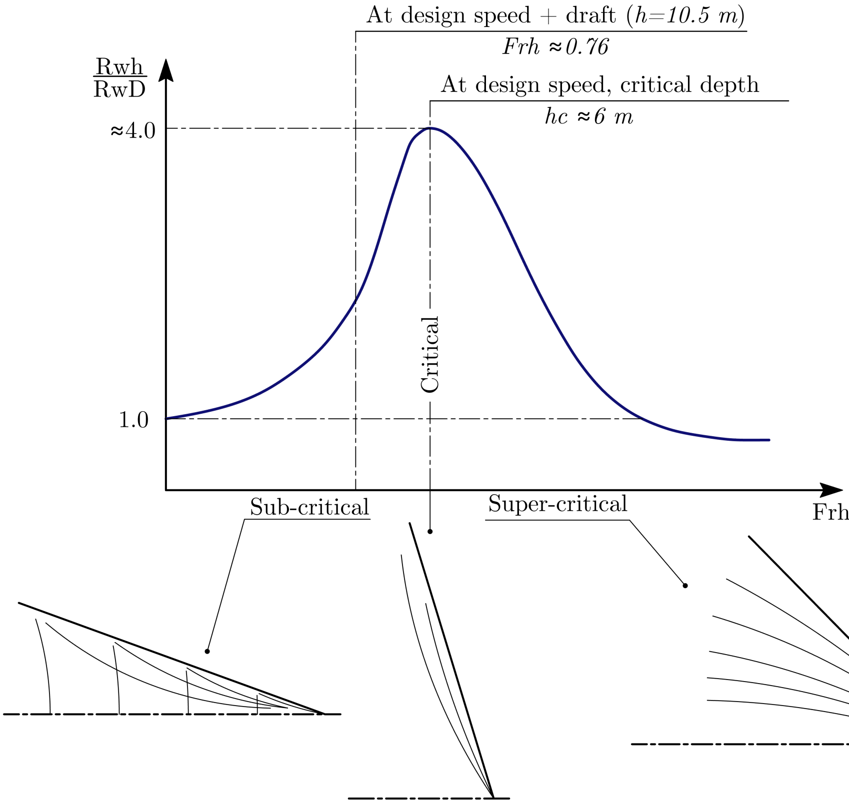

Figure 3.5: The ratio between wave resistance in shallow water vs. deep water plotted against the depth-based Frode number, inspired by Zhao (1984)

According to the specifications of the reference ship (Table 4.1), the design speed is set at 15 *kn* and the design draft is set at 10.5 *m*. In a hypothetical operational scenario where the ship is travelling at its design speed while the hull bottom virtually touching the seabed (the depth of the water is equal to the design draft), the depth Froude number can be calculated as follows.

$$Frh_{design} = \frac{v_{design}}{\sqrt{g \times T_{design}}} = \frac{7.7167}{\sqrt{9.81 \times 10.5}} = 0.760 \tag{3.13}$$

It can be reasonably assumed that the above-calculated design Froude number ($Frh_{design} = 0.760$) sets the upper limit for the ship's operational conditions. To exceed it, either the ship speed should be higher than the design speed or the depth of water should be lower than the design draft. The former is improbable, and the latter is outright impossible as it would result in a direct bottom collision or grounding of the ship. The ship operational region under this upper limit is shown in Figure 3.6, where it spans the entirety of the far subcritical zone and extends slightly into the near critical zone. This will substantially ease up the computational effort expended on generating the training dataset for the surrogate model and the training process itself as steep non-linearities (in the near-critical zone) are not included for the most part. Moreover, this preliminary analysis based on shallow water hydrodynamics hints that the surrogate model should be developed only for the scenarios that lie below the design Froude number ($Frh_{design} = 0.760$).

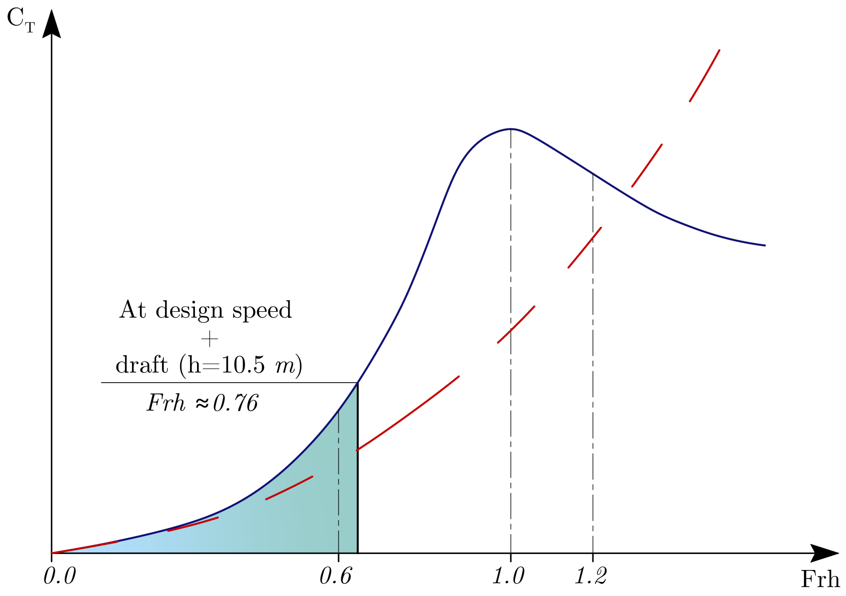

Figure 3.6: Variation of the total resistance coefficient with the depth-based Froude number in; (- - - -) deep water and (——) shallow water, along with the likely operational zone of the reference ship shaded; inspired by Larsson and Raven (2010); and Molland, Turnock, and Hudson (2011)

3.4 Methods used to predict hull resistance

One of the primary factors driving a ship's design process is the resistance it will encounter during operation. The ship's main power source (propulsion source) and propulsors are directly sized based on this ship's resistance. The propulsor should be large enough to provide enough thrust to move the ship forward while overcoming the resistance (Rawson and Tupper, 2001). The propulsion power source should be capable of providing enough power to drive the propulsor while overcoming any inefficiencies along the propulsion train. Therefore, accurately estimating the resistance is integral when it comes to designing an effective vessel in terms of monetary terms.

Beyond the design phase, a critical use case of resistance prediction can be seen in tandem with the development of the MARIDATA initiative (discussed in Section 1.1)linked to the objective of developing a reliable prediction model for shallow water resistance. Therefore, a literature review was conducted to identify the most effective method for calculating resistance. The resistance calculation methods can be categorized into four main classes based on the underlying mechanism.

3.4.1 Empirical/semi-empirical methods

Empirical methods were mainly used by early naval design practices amidst the unavailability of more sophisticated methods to calculate ship resistance. Rather than the dependency on experimental observations and test data alone like empirical methods, semi-empirical methods are formulated with the further assistance of theoretical formulas and visual graphs from reliable literature.

Holtrop-Mennen method

The widely known Holtrop-Mennen method is a semi-empirical method that employs a set of equations to approximate the resistance of a particular ship. The equations were first developed with the influence of a large number of model test results (Holtrop and Mennen, 1982). The displacement hull forms used in those model tests were characteristic of the period spanning from the 1970s to the 1980s. Modern hull forms, however, may vary significantly from those earlier designs, thus potentially introducing inaccuracies into predictions. To add to this uncertainty, the Holtrop-Mennen model is limited to the following operational and geometric conditions.

$$\begin{aligned} & Fn_v && < 0.45 \\ 0.55 \ \le\ & C_p && \le 0.85 \\ 3.90 \ \le\ & \frac{L}{B} && \le 9.50 \end{aligned} \tag{3.14}$$

where:

Fn_v = velocity based Froude number

C_p = prismatic coefficient of the hull [$= {}^{\nabla}/_{L_{PP}A_M}$]

∇ = submerged volume of the hull

L = length of the hull

B = beam of the hull

t = time

Standard series methods

Standard series in ship design refers to a group of well-defined hull forms that can be used as the foundation for developing new hulls. The resistance methods inherently formulated for these standard hull series are counted toward this category of resistance prediction methods. If a particular hull form resembles the geometric characteristics of a standard series, the respective resistance method can be leveraged to generate a reliable approximation of its resistance. Based on the requirements, either linear or higher-order interpolation is applied to adjust the resistance for variances in scales and dimensions. Some well-established resistance models, specifically designed for these standardized series, are as follows:

- Taylor Standard Series: First published in 1910, the resistance model currently possesses a broad range with the continuous addition of data over time (Gertler, 1976). The current model is capable of accompanying compatible hull geometries in the range $\sqrt{V}/L = [0.3,\ 2.0]$. The data are interpolated between three $B/T = \{2.25,\ 3.00,\ 3.75\}$ values, five ∇/L ratios, and eight prismatic coefficient $C_p = [0.48,\ 0.80]$ values. This allows the resistance model to be compatible with a large number of narrow to full hull forms operating at slow to fast speeds. Once the Taylor residual resistance coefficient C_R of a compatible hull form is interpolated from the resistance model, corrections are added to determine the total resistance coefficient C_T. The effective horsepower is calculated by (S is the wetted surface area),

$$\mathrm{EHP_n} = SC_{\mathrm{T}}V^3 \tag{3.15}$$

- BSRA Methodical Series: The BSRA standard series covers a range of different purpose hull forms and is being used up to date. The hulls with the block coefficients $C_B = [0.65,\ 0.80]$, bredth to draft ratio $B/T = [2.10,\ 3.45]$ and length to bredth ratio $L/B = [5.80,\ 8.40]$ are compatible with the model (BSRA, 1971).

3.4.2 Direct model testing methods

As the name suggests, model tests are involved with testing scaled-down replicas (geometrically similar) of ship hulls. These ship models are operated in controlled environments that can mimic operational hydrodynamic conditions. The controlled environments either can be a towing tank, circulating water channel, cavitation tunnel or a depressurized wave tank. Considering the focus here is measuring the hull resistance, a towing tank would be the most suitable testing facility. The basic idea is to construct a scaled-down model of the ship and tow it forward while secured to a rail-driven carriage. The connection between the model and the carriage is equipped with numerous types of sensors that can measure motions and forces (Gao, 2020).

The independence of resistance components described along with Equation 3.11 is the fundamental idea behind model testing to measure ship resistance. Based on this, William Froude postulated that separate consideration of residual and frictional resistance components will make the ship model testing possible. He observed that moving ships and model counterparts generate identical wave patterns when their speeds are proportional to the square roots of their lengths. The model tests are always conducted under “Froude’s similarity” conditions due to this. Froude similarity essentially states that a model should be tested at a speed that matches the Froude number of the actual ship (known as the corresponding speed), should the resistance results be accurate. When the exponent s represents the real ship and exponent m represents the model, Froude similarity can be given with equations (Carlton, 2007);

$$\frac{V_{\mathrm{M}}}{(gL_{\mathrm{M}})^{1/2}} = \frac{V}{(gL)^{1/2}} \tag{3.16}$$

3.4.3 Numerical methods

The premise of resistance calculation using numerical methods is to solve a set of governing equations delineated in Section 3.1. As explained, governing equations like Navier-Strokes are quite complex to be solved analytically. But, through a combination of strategic simplifications and numerical techniques, solutions can be easily reached. The computerized numerical algorithms developed in this regard are commonly identified as Computational Fluid Dynamics (CFD) solvers. Presently, one can afford to freely choose between a myriad of CFD solvers tailored for a variety of applications, each governed by distinct computational engines and employing diverse numerical techniques.

Due to the independent nature of resistance components, numerical solvers are capable of decomposing the total resistance into fundamental components. The frictional resistance can be separated by integrating the viscous shear stresses along the wetted surface and calculating the residual components by subtracting the frictional components from the total resistance. When using CFD methods, especially on hydrodynamically sensitive cases like shallow water resistance calculations, utmost care must be taken to select the best parameters such as the method of discretization and the turbulent model (Song et al., 2023). The discretization redefines a complex fluid/solid domain as simpler elements or cells, as well as grid points on which governing equations can be easily applied. In the absence of proper analytical models to model turbulence, turbulent models are used to approximate the evolution of turbulent flows numerically.

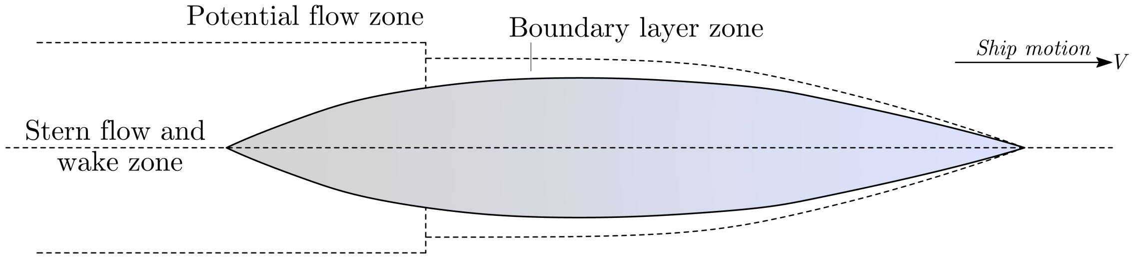

Figure 3.7: In a general CFD simulation associated with ship motion, the combined water, air, and structure domain can be identified as a combination of multiple zones

3.4.4 Comparison of some existing resistance prediction methods

Table 3.1 summarizes several, widely-used resistance calculation methods found in the literature. Some of them are specifically designed for shallow water calculations (Schlichtings, Lackenby, Jians) and some are capable of handling both shallow water and deep water scenarios (model testing, numerical methods). Most shallow water methods rely on applying corrections to deep water resistance values. Due to reasons such as outdated data in the modern context, lack of physical foundation, and industry scrutiny, among others, all methods except for model testing and numerical methodologies were dismissed as viable candidates for resistance calculation (Zeng, 2019). Gathering a large number of resistance data through model testing would demand significant financial investments; therefore, numerical methods were ultimately selected as the most appropriate approach.

Table 3.1: Different methods used to calculate the ship resistance and pros and cons of adopting them in shallow water resistance calculations

Method	Compatibility with the project ojectives
Standard series	The modern geometry of the reference ship might not be correspondent with any of the standard series[1], explicit shallow water capabilities were not discovered[2]
Holtrop-Mennen	Primarily developed and validated for deep water conditions, might add errors in shallow water cases[3]
Direct model testing	A validated method for accurate shallow water resistance estimations[4]. Specialized in inland shipping (and restricted waterways), the towing/wave tank facility at DST, Duisburg can perform well when it comes to shallow water scenarios[5]
Schlichtings method	Specified for shallow water resistance calculations. Estimates the shallow water resistance by adding correction factors based on velocity loss that occurs in shallow water. It however neglects the effect of ship squat on the resistance[6]
Lackenby method	As an extension to the Schlichtings method, it is compatible with a broader range of ship types[7]. However, the reliability of the method on modern ship shapes has been recently scrutinized[8]
Jiangs method	The method includes relatively recent model test data, yet the various simplifications assumed, coupled with the fact that it is tailored specifically for container ships may render it unsuitable within the context of work.[9]
Numerical methods	When applied correctly, numerical methods were found to be resulting in accurately predicted shallow water resistance. However, substantial computational time and resources required by these methods should be considered, given that a large amount of resistance data points need to be computed to synthesize the training dataset required

(1) (Gertler, 1976)
(2) (BSRA, 1971; Todd, 1963)
(3) (Holtrop and Mennen, 1982)
(4) (Gao, 2020)
(5) (Mucha et al., 2018)
(6) (Schlichting, 1940)
(7) (Lackenby, 1961)
(8) (ITTC, 2017)
(9) (Jiang, 2001)

3.5 Observations and concluding remarks

The following conclusions were drawn from the observations made, and analyses carried out in the chapter.

- The Hydrodynamic behaviour of a ship can be analysed through a number of methods. However, shallow-water sailing cases could not be analysed with every method. Methods like potential flow theory were found to be ineffective in calculating shallow water ship resistance due to inviscid assumptions. It was deemed optimal to use the Navier-Strokes method to calculate resistance. Solving Navier-Strokes equations, however, will be a computationally demanding task.

- Total ship resistance can be decomposed into multiple components which stand independent of each other. Therefore, there is a possibility to develop several surrogate models to represent each component (viscous, residual, wave) and linearly combine them to get the total resistance.

- Individual resistance components, along with the total resistance can be represented as dimensionless coefficients called resistance coefficients. These coefficients enable easy comparison of resistance between different ships. However, since the aim is to develop a surrogate model for a single ship, it may not be necessary to represent the predicting variable (added resistance in shallow water) as a dimensionless quantity.

- Ship resistance in shallow water can be analysed in three distinct domains defined on the depth-based Froude number. The reference ship is most likely to operate in the far-subcritical zone which is not involved with extreme non-linearities. Based on this, the intended surrogate model can be limited to depth-based Froude numbers below 0.76.

- Among a plethora of ship resistance calculation methods available, numerical modelling and direct model testing appeared to be the most suitable methods for the calculation of initial sample points. Other models were either outdated, scrutinized, or seemingly incapable of dealing with intricate flow patterns associated with shallow water ship motion.

- Due to the substantial financial investments demanded for direct model testing, numerical simulation methods were finalized for resistance calculation.

- Ship resistance, especially shallow water ship resistance is dependent upon numerous factors. However, in the work presented, three main variables will be used as independent variables, namely, the velocity of the ship ($v\,[ms^{-1}]$) that determines the velocity-based Froude number, depth of the water ($h\,[m]$) that determines the depth-based Froude number, and the draft of the ship ($T\,[m]$) that determines the wetted surface area and submerged volume of the ship.

CHAPTER

Numerical setup for resistance calculations

4

The chapter is dedicated to explaining how sample points for the surrogate model were calculated through an OpenFOAM setup. The setup was able to evaluate the resistance on the hull for different depth (h), draft (T) and velocity (v) combinations.

4.1 Simulation structure and governing equations

As concluded in the previous chapter, the resistance data for training the surrogate model was procured through a sequence of CFD simulations. The simulations were carried out with the OpenFOAM numerical solver. With its years-long expertise in inland shipping, DST was already in the possession of a well-refined OpenFOAM framework to carry out reliable shallow water simulations (Ley and Moctar, 2021; Friedhoff et al., 2019). It was deemed possible to integrate the same framework into this thesis scope after adaptation with some minor modifications. Employing OpenFOAM offers distinct advantages when compared to other commercial or open-source solvers available, including: (a) the open-source nature would not pose any future obstacles in terms of licensing the work, (b) the heavily customizable setup will facilitate ultimate freedom and (c) availability of a broad array of modules and libraries which had been proven for their reliability over time. The numerical solutions were sought through the PIMPLE algorithm operated on Reynolds Averaged Navier-Stokes (RANS) equations. The PIMPLE algorithm is generally used in transient CFD simulations as a combination of Semi-Implicit Method for Pressure Linked Equations (SIMPLE) and Pressure Implicit with Splitting of Operator (PISO) algorithms. In simple terms, the PIMPLE algorithm operates by applying the steady state SIMPLE algorithm iteratively into each time step of a transient simulation[1].

A brief explanation of the underlying RANS equations that govern the PIMPLE should commence with the conservation of mass and momentum laws presented in Equation 3.6. The sole purpose of the algorithm is to ensure these equations are applied correctly in numerical form.

---

[1] For additional information, refer to https://doc.cfd.direct/

- To revise, the mass conservation (continuity) equation is given by ($\vec{V} = [u, v, w]$ is replaced by u),

$$\frac{\partial \rho}{\partial t} + \nabla \cdot (\rho u) = 0 \tag{4.1}$$

- Under the assumptions of an incompressible fluid, the variation of the density with respect to time becomes null.

$$\nabla \cdot (\rho \mathbf{u}) = 0 \tag{4.2}$$

- The momentum equation conserves the momentum of a small control volume of fluid by considering the rate of change of momentum and net forces acting on it.

$$\frac{\partial \rho \mathbf{u}}{\partial t} + \nabla \cdot (\rho \mathbf{u}\mathbf{u}) = \mathbf{F} + \nabla \cdot \sigma \tag{4.3}$$

- The term F represents the body forces acting on the control volume. The σ term represents the combination of viscous stresses and normal stresses. This can be presented in tensor form using the Cauchy stress tensor.

$$\rho \left(\frac{\partial \mathbf{u}}{\partial t} + \mathbf{u} \cdot \nabla \mathbf{u} \right) = \mathbf{F} + \nabla \cdot \sigma \tag{4.4}$$

$$\sigma = \begin{bmatrix} \sigma_{xx} & \sigma_{xy} & \sigma_{xz} \\ \sigma_{yx} & \sigma_{yy} & \sigma_{yz} \\ \sigma_{zz} & \sigma_{zy} & \sigma_{zz} \end{bmatrix} \tag{4.5}$$

- For an incompressible fluid, the stress tensor can be represented in a simplified manner after expanding the stresses as a result of dynamic viscosity.

$$\rho \left(\frac{\partial \mathbf{u}}{\partial t} + \mathbf{u} \cdot \nabla \mathbf{u} \right) = -\nabla p + \mu \nabla^2 \mathbf{u} + \mathbf{F} \tag{4.6}$$

4.1.1 Reynolds Averaged Navier-Strokes Equations (RANSE)

Reaching an analytical solution for Navier-Strokes equations is not feasible in the present-day context. Therefore, they are solved by running Direct Numerical Simulations (DNS). Such simulations still demand astronomical computational resources as the mesh needs to be fine enough to catch even the infinitesimal flow variations or eddies.

- The RANS approach is used instead. The method decomposes the main fluid properties (velocity, pressure, stresses) into time-averaged (mean) and fluctuating components. Time-averaged components are presented with capital letters.

$$u_i = U_i + u_i' \quad ; \quad p = P + p' \quad ; \quad \tau_{ij} = T_{ij} + \tau_{ij}' \tag{4.7}$$

- The above process is called Reynolds decomposition and one of the main characteristics is mean values of fluctuating terms getting zero.

$$\overline{u_i'} = \overline{p'} = \overline{\tau_{ij}'} = 0 \tag{4.8}$$

- The continuity equation (Equation 4.2) can be written in decomposed terms as follows.

$$\frac{\partial (U_i + u_i')}{\partial x_i} = 0 \Rightarrow \frac{\partial U_i}{\partial x_i} = 0 \quad ; \quad \frac{\partial u_i'}{\partial x_i} = 0 \tag{4.9}$$

- The same way, the momentum equation Equation 4.3 becomes (after some manipulations, and written in Einstein notation where, $i, j = 1, 2, 3$);

$$\frac{\partial (U_i + u_i')}{\partial t} + \left(U_j + u_j'\right) \frac{\partial (U_i + u_i')}{\partial x_j} = -\frac{1}{\rho} \frac{\partial (P + p')}{\partial x_i} + \frac{1}{\rho} \frac{\partial \left(T_{ij} + \tau_{ij}'\right)}{\partial x_j} + \frac{1}{\rho} F_i \tag{4.10}$$

- The terms represented by R are called Reynolds stresses with $R_{ij} = R_{ji} = -\rho\overline{u_i' u_j'}$. In tensor form, this is known as the Reynolds stress tensor.

$$R = \overline{u' \otimes u'} = \underbrace{\frac{2}{3} kI}_{\text{isotropic}} + \underbrace{\overline{u' \otimes \mathbf{u}'} - \frac{2}{3} kI}_{\text{deviatoric}} \tag{4.11}$$

- In the above equation, k term represents the turbulent kinetic energy.

$$k = \frac{1}{2} \overline{u' \cdot u'} = \frac{1}{2} \operatorname{tr}(R) \tag{4.12}$$

- When the Equation 4.10 is averaged with respect to the time the following expression is reached.

$$\frac{\partial U_i}{\partial t} + \frac{\partial \left(U_j U_i\right)}{\partial x_j} = -\frac{1}{\rho} \frac{\partial P}{\partial x_i} + \frac{1}{\rho} \frac{\partial}{\partial x_j} \left(T_{ij} + R_{ij}\right) + \frac{1}{\rho} \left(F_i\right) \tag{4.13}$$

Driven on the aforementioned governing equations, the PIMPLE algorithm would execute the ship resistance calculation case in OpenFOAM. The ship was set to move along the vertical z-axis (heave) and rotate around the y-axis (trim). All the simulations were executed in the parallel environments set up for DST in a High-Performance Cluster (HPC). The HPC was accessed by the Linux subsystem 2.0, running in a Windows environment, governed by `Ubuntu 20.04.6` and `Python 3.11.2` (64-bit).

4.1.2 $k-\omega$ SST turbulence model

The Reynolds stress tensor (R) is not a quantity introduced by any equations so far. Therefore, it must be calculated using a mathematical model that can mimic the turbulence field of the fluid, also known as the turbulent model. Among dozens of turbulent models available in the literature, choosing the correct one would guarantee a reliable accuracy of CFD results (Schiestel and Chaouat, 2022). The mixing models and linear eddy viscosity models are the simplest forms available in this regard. They all are based on turbulent equations published by Boussinesq, under the assumption that turbulence is isotropic and homogeneous (Durighetto et al., 2022). The linear models are again divided into the forms of zero-equations (algebraic model), one-equation (Spalart-Allmaras model) and two-equation ($k-\epsilon$ and $k-\omega$ models), based on the number of mathematical equations associated with them. The two-equation models can guarantee higher accuracy compared to the remaining two types, especially in complex flow scenarios like shallow-water ship motion.

The turbulence model chosen to be used in the CFD setup was the $k-\omega\, SST$ (Shear Stress Transport). It is a two-equation, linear eddy-viscosity model that provides great prospects in terms of robustness and accuracy in shallow water simulations (Zeng, 2019, p. 78). The model was first introduced by Menter (1994) and it is an extension of the $k-\omega$ model which performed well on the flows with strong anisotropy or separation. However, for flow regions far away from the boundary layer, or walls, the $k-\epsilon$ model is used. Nevertheless, its inability to accurately model low Reynolds numbers or near-wall flows is overcome in the $k-\omega\, SST$ model. This is achieved by switching to the more capable $k-\omega$ model inside the boundary layer and near-wall regions.

4.2 Hull geometry and computational domain

The particular reference ship for the surrogate development was a collective choice taken by the main stakeholders of the MARIDATA project. The selected ship; designed to function as a modern chemical oil tanker of 192 m boasts a unique geometry. It is imperative to highlight the ongoing confidentiality agreement between the shipowner and the author regarding the disclosure of the hull shape. Under these confidentiality conditions, a comprehensive depiction of the hull is not presented at any instance of the report. Nevertheless, the utmost effort has been put into tailoring all the visualizations to facilitate the convenience of readers while adhering to the constraints of confidentiality. The major geometric and operational parameters of the reference ship are presented in the Table 4.1.

The computational domain, along with the imposed boundary conditions are shown in Figure 4.1. Symmetry boundary condition was used with respect to the ship's centerline plane. Placing the forward inlet 1.5×ship length ahead was deemed to be appropriate when catching the effect of inlet flow while not enlarging the computational domain unnecessarily (Table 4.2). The other extents of the water-air domain were set after referring to already executed, successfully validated shallow water simulations carried out by DST in the past.

Table 4.1: Major dimensions and operational parameters of the chemical oil tanker considered as the reference ship

Parameter	Value	Unit
Ship type	Chemical oil (C/O) tanker	[–]
Length overall	192	[m]
Beam	32	[m]
Nominal draft (T)	10.5	[m]
Maximum speed	15	[kn]

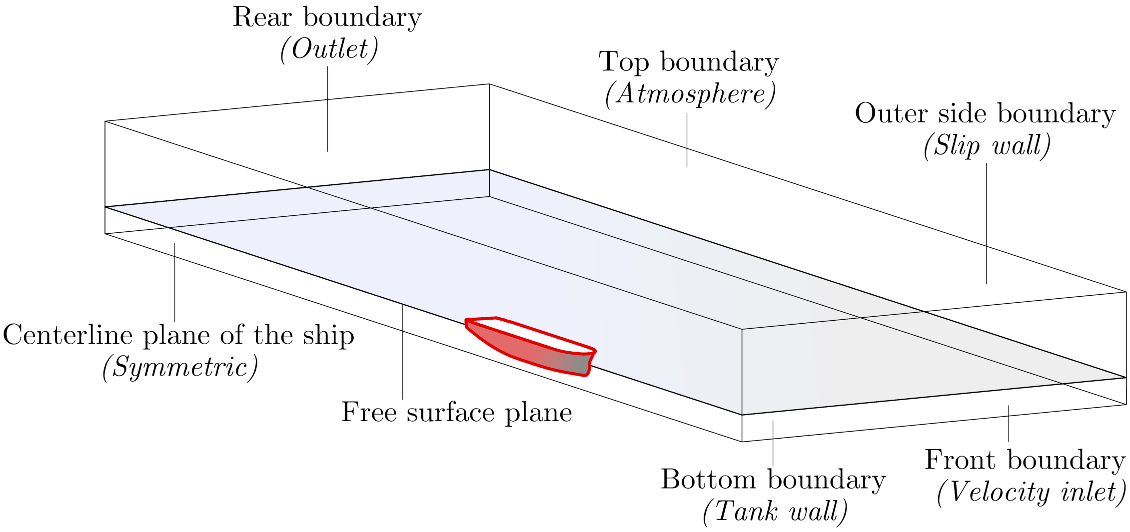

Figure 4.1: The computational region consisting of the ship hull and fluid-air domain used for the simulations with the physical boundaries set to achieve an optimal compromise between computational effort and accuracy (ITTC, 2011)

Table 4.2: Geometric definition of the computational domain in terms of ship length and boundary conditions

Boundary	Boundary condition	Position
X_{min}	Velocity outlet (Patch)	$4 \times LOA$ backward from stern
X_{max}	Velocity inlet (Patch)	$1.5 \times LOA$ forward from bow
Y_{max}	Slipwall (Patch)	$12 \times BOA$ right from starboard side
Y_{min}	Symmetric plane	Centerline plane of the ship
Z_{max}	No-slip wall moving with fluid	$1 \times$ Water depth below free surface
Z_{min}	Slipwall (Atmosphere)	$0.5 \times LOA$ above the free surface

4.2.1 Descretization of the domain

The whole domain was discretized using polyhedron (predominantly hexahedron) mesh elements (Figure 4.3). The mesh was refined around sensitive regions such as the free surface and non-slip wall to capture complex flow patterns in these areas, which can be seen in Figure 4.4. It is evident that the height of mesh elements is set to low around the non-slip bottom wall, and progressively increases as the vertical distance increases. To monitor how the domain is shared by structure, water, and air at a specific moment, different methods are used by CFD solvers, namely, interface-tracking, and interface capturing. Volume of Fluid (VoF) is a method that falls under the interface-capturing mechanism, that can effectively monitor the motion of the free surface and water-structure-air interaction (Hirt and Nichols, 1981). Essentially, the VoF method assigns volume fraction (α) values for each cell element in the domain as seen in Figure 4.2. The free surface can be isolated from the whole domain by extracting the cell elements with $\alpha = 0.5$, in other words, elements that are occupied with half-volume water and half-volume air.

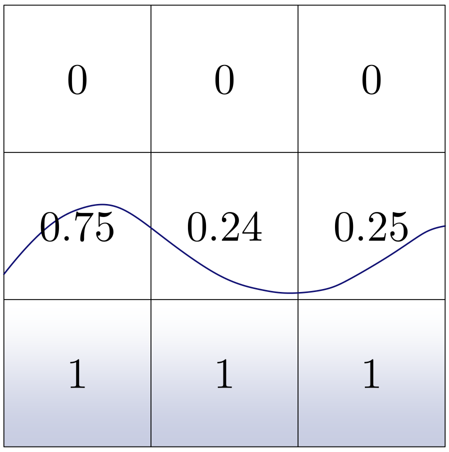

Figure 4.2: The principle behind the volume of fluid (VoF) method applies 0-1 values for each cell element based on the volume fraction of water. A cell filled with water will be assigned the value 1 and a cell filled with air will be assigned 0

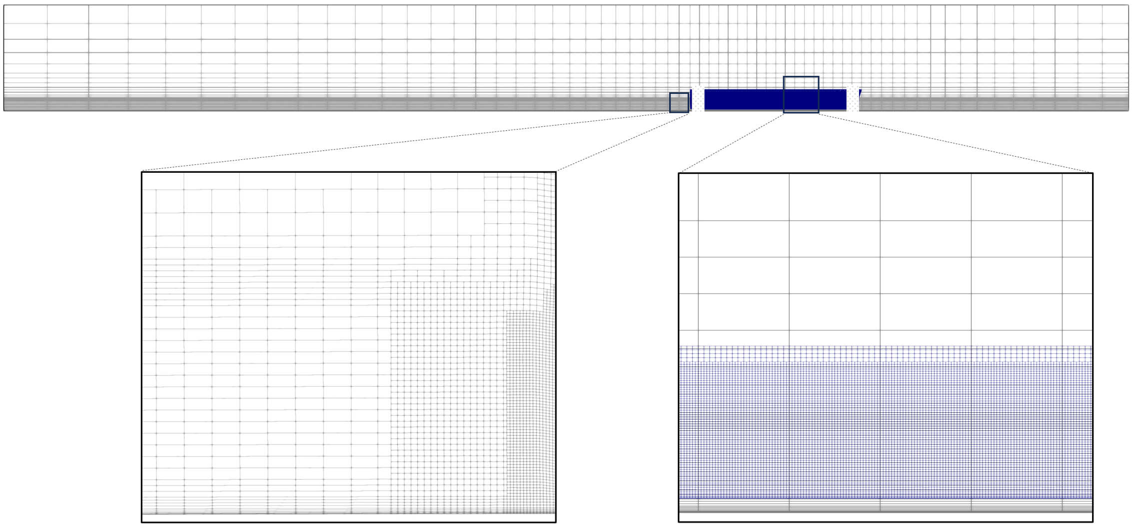

Figure 4.3: Visualization of the grid generated for the simulation case with parameters; depth = 12.5 m, draft = 10.5 m. A square region is zoomed in to show the fine adaptation of the grid under the hull and over the wetted surface area

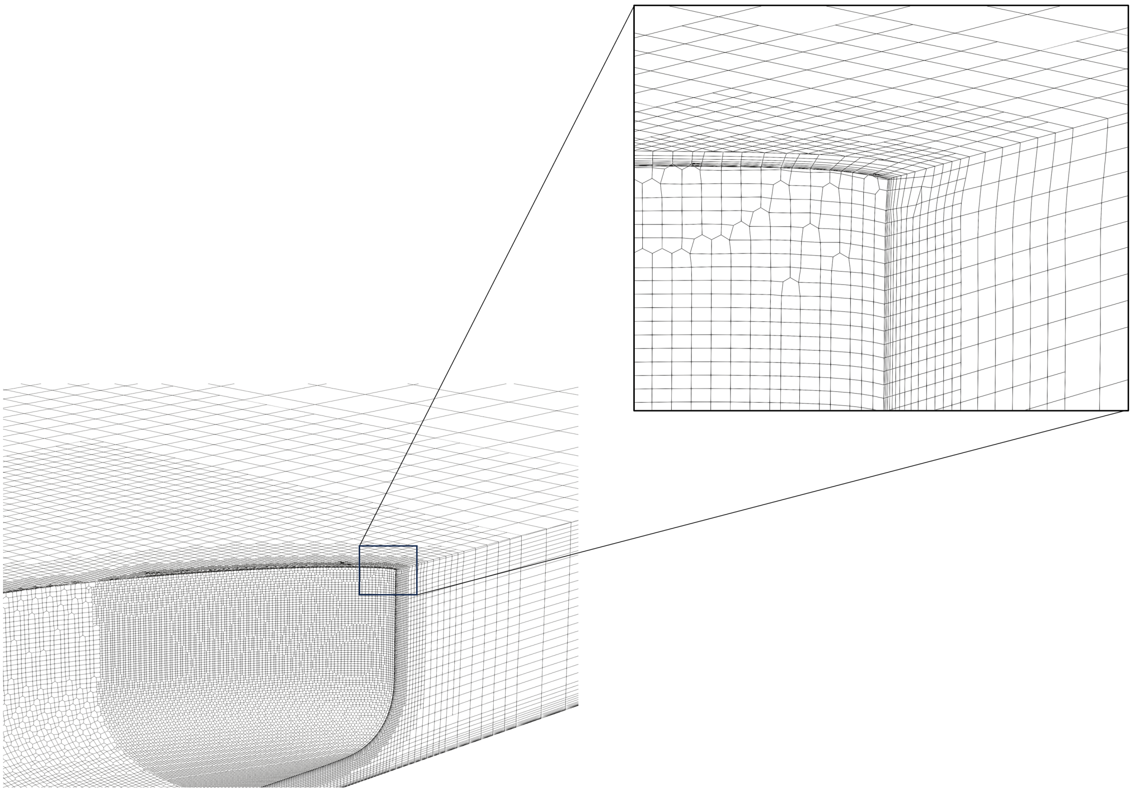

Figure 4.4: Locally refined grid (mesh) generated at the free surface for the case with parameters; depth = 12.5 m, draft = 10.5 m. The zoomed-in window highlights how the mesh is more refined around the fluid-structure interaction regions

4.3 Validation of the CFD results

A dedicated mesh independence study has not been carried out. The sizing of the elements has been set in line with already existing CFD simulations carried out on the reference ship by DST. those existing simulations were validated through model tests also carried out at DST, thus the delivered accuracy was not in question. The validation of the CFD setup can be established in the model scale as seen in Figure 4.5, with existing sets of model testing results and CFD results.

The model corresponding to the simulation is scaled down by a 44.8:1 length ratio. Therefore, the length of the model calculates down to 4.156 m, given that the length of the reference ships is 192 m. Model test data were available for four different depth/draft (h/T) values. No model test data were found for the case with $h/T = 8$. It is evident from the plot that, CFD results agree well with the model test results at low Froude numbers. This agreement becomes weaker as the Froude number increases. However, throughout the Froude range, the maximum error was observed to be less than 3%, underlining the satisfactory accuracy of the CFD model. It is also noteworthy to mention the increasing gap between the curves along with the increment of h/T values. This prompts that shallow water effects become more intensified as the depth is gradually decreased.

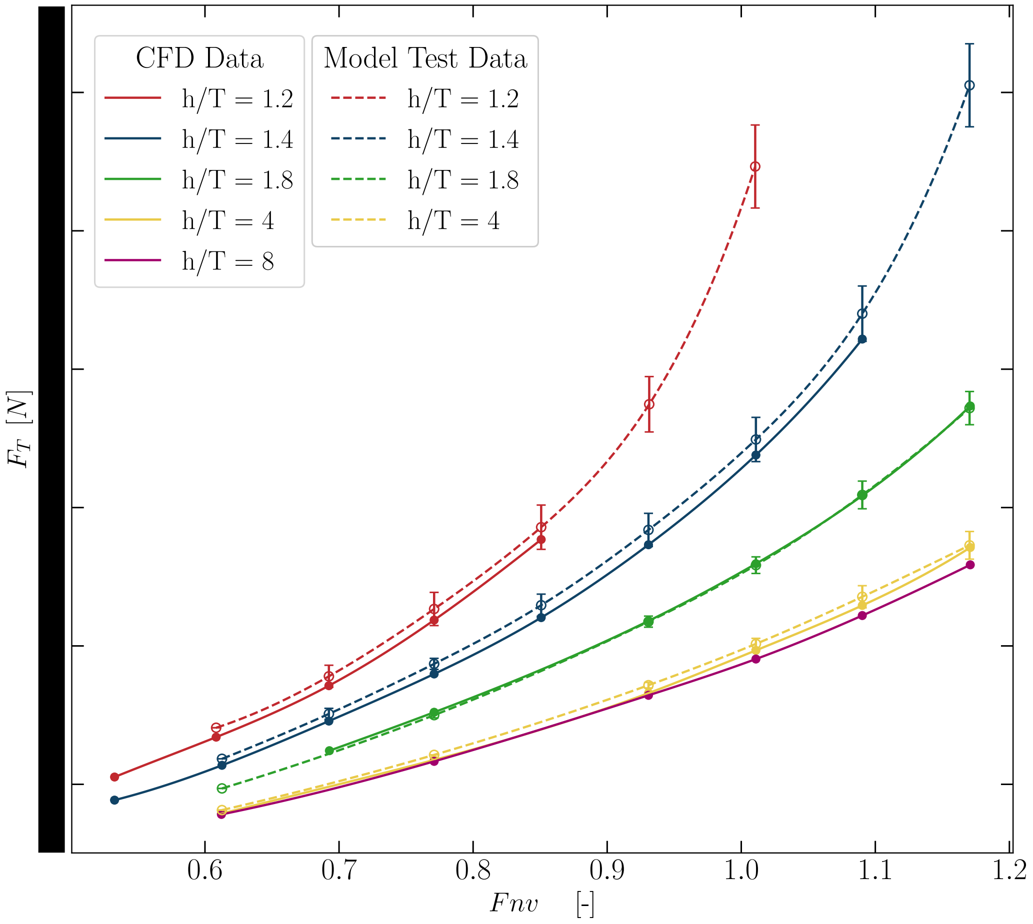

Figure 4.5: Comparison of total resistance data acquired through CFD simulations vs. model testing carried out on a 44.8:1 model of reference ship, categorized under four different h/T values

4.4 Discussion and conclusion of numerical results

With the original setup, an average shallow water simulation (such as the case demonstrated in Figure 4.6, Figure 4.7 and Figure 4.8) operated on a grid of 3.5 *million* elements with `nBaseCellsPerLength` (number of divisions a unit length should be discretized to) parameter set to achieve a fine mesh. The simulation run time was found to be more than 72 *hours*. With the time constraints imposed, it was later decided to reduce the `nBaseCellsPerLength` by 33% (down to 1.7 *million* mesh elements), which led to a reduced simulation time of less than 48 h. The maximum deviation from the original CFD results was less than 5%, which was approved by the stakeholders from DST.

Figure 4.6 visualizes the difference between wave profiles generated in deep water and shallow water scenarios. The colour scales are synchronized to facilitate an accurate comparison. It is obvious that the wave profile of shallow water is significantly more intense than that of deep water, leading to a proportionally higher wave resistance component acting on the ship.

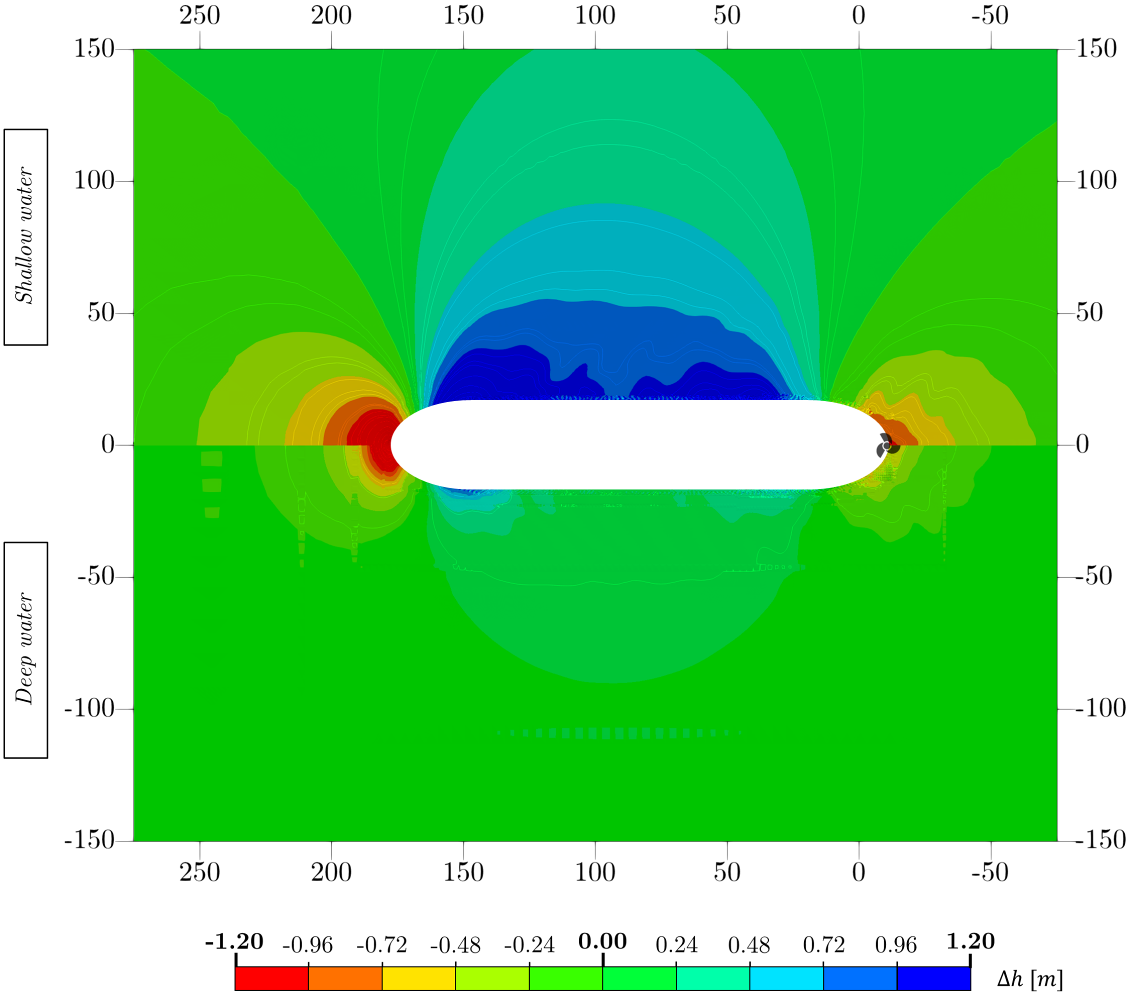

Figure 4.6: Comparison of the generated wave profiles for the ship operating at same draft and velocity $T = 10.5m$, $v = 5ms^{-1}$ but different water depths; shallow water condition $h = 12.5m$ vs. deep water condition $h = 50m$

Figure 4.7 demonstrates the comparison of pressure resistance components along the hull bottom for the same simulation case. The shallow water case shows a considerably higher pressure coefficient, attesting that the pressure resistance component will also be higher in shallow water.

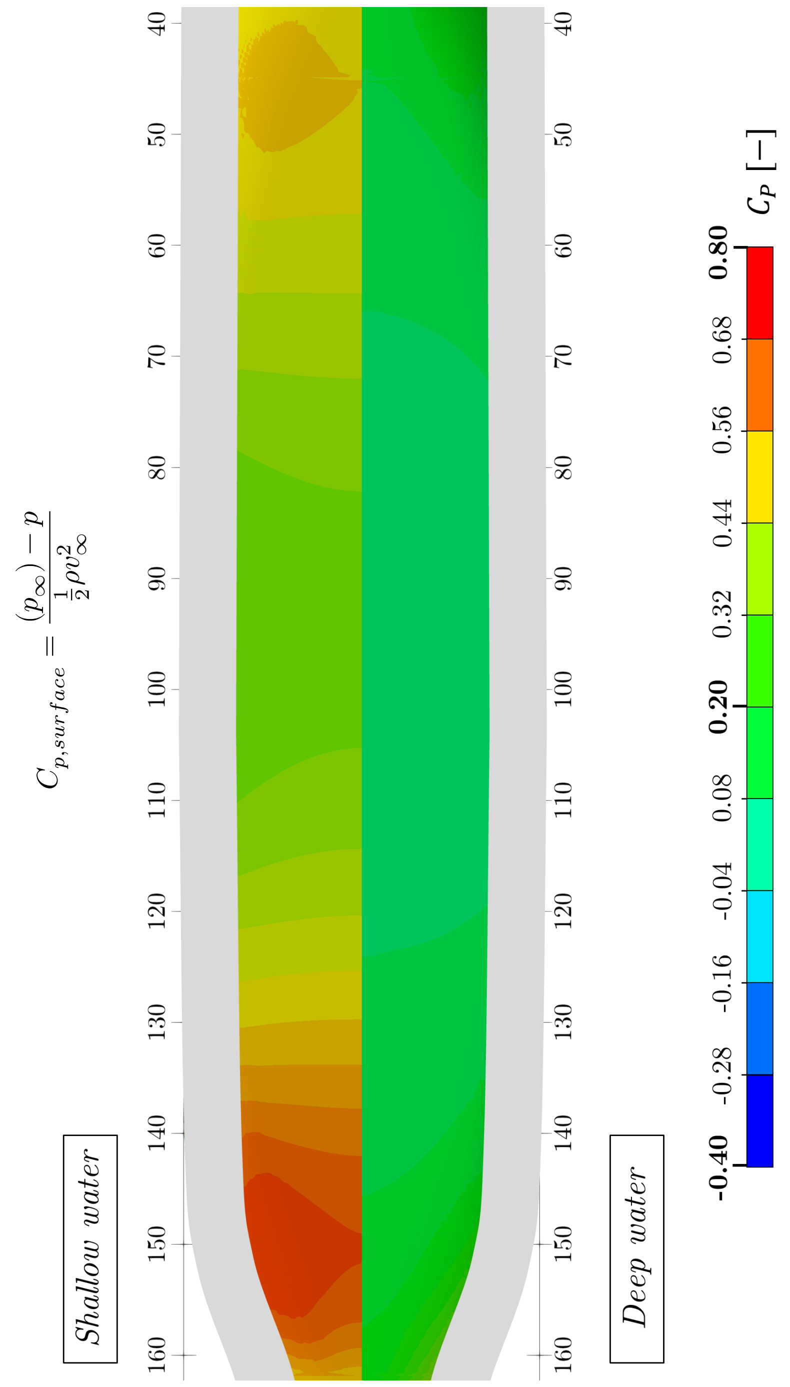

Figure 4.7: Comparison of the surface normalized pressure resistance coefficient for the ship operating at the same draft and velocity but different depth conditions; Shallow water: $[h = 12.5m, T = 10.5m,\ v = 5ms^{-1}]$ vs moderate deep water: $[h = 50.0m, T = 10.5m,\ v = 5ms^{-1}]$

Figure 4.8 demonstrates the comparison of friction resistance components along the hull bottom for the same simulation case. Coinciding with both above cases, the friction resistance component is also higher in the shallow water case.

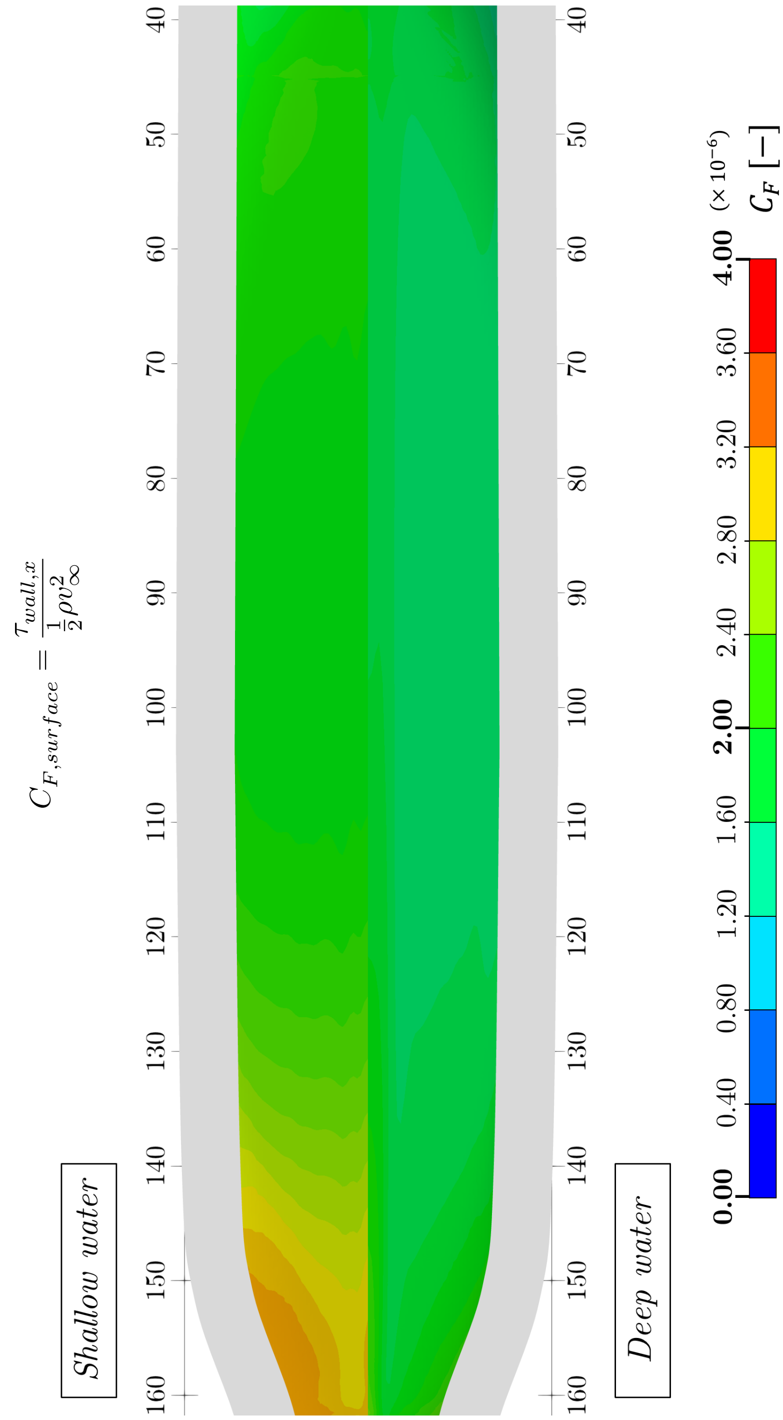

Figure 4.8: Comparison of the surface normalized skin friction resistance coefficient for the ship operating at the same draft and velocity but different depth conditions; Shallow water: $[h = 12.5m, T = 10.5m, v = 5ms^{-1}]$ vs moderate deep water: $[h = 50.0m, T = 10.5m, v = 5ms^{-1}]$

4.4.1 Concluding remarks

The summary of the chapter in terms of the observations made, and analyses carried out are presented with the conclusions.

- Development Centre for Ship Technology and Transport Systems already in possession of a reliable OpenFOAM setup that was already validated for its accuracy in shallow water simulations. It was possible to integrate the setup with a few adjustments.

- The adjusted and finalized CFD setup was operating on Reynolds Averaged Navier-Stokes numerical equations executed by the Semi-Implicit Method for Pressure Linked Equations (SIMPLE) algorithm. To model the turbulent flow, the $k{-}\omega SST$ turbulence model was used.

- The ship on which the intended surrogate model will be based is identified as the reference ship in this report. The reference ship is a medium-sized, modern chemical tanker. Due to its unique shape, the hull form of the reference ship will not be shown in the report. In such occasions where the whole geometry is required for visualizations, the well-known MOERI KVLCC2 tanker hull will be shown in place.

- The computational domain would be discredited using hexahedron mesh elements. An average shallow water simulation with fine mesh would require more than 72 h to converge. Considering the strict time restrictions, a coarser mesh was decided to be adopted with a lesser simulation time of less than 48 h. The maximum error of resistance calculations was under 5%.

- Side-by-side comparison of the CFD results between shallow water and deep water simulations (with all other parameters kept the same) proven that all wavemaking, pressure, and friction resistance components are significantly enhanced in shallow water.

- Therefore, the independent variable of the surrogate model can be defined as follows. Given the total ship resistance in shallow water (small h) is $F_{T,shallow}$ and the total ship resistance in deep water (large h while keeping the other two independent variables $\{v \text{ and } T\}$ the same for both cases), added resistance in shallow water is,

$$\Delta F_T = F_{T,shallow} - F_{T,deep} \ [N] \tag{4.14}$$

- The same can be expressed in the non-dimensional form as a resistance coefficient, where S is the wetter surface area of the ship.

$$\Delta C_T = \frac{\Delta F_T}{\frac{1}{2}\rho S v_2} \ [-] \tag{4.15}$$

CHAPTER

Data Preprocessing and surrogate model definition

5

The chapter is dedicated to explaining the how the initial dataset was preprocessed, and how boundary definition and data transformation carried out before the initialization of the surrogate model.

5.1 Boundaries of the surrogate model

The boundaries of the surrogate model were set based on a critical analysis of the operational capabilities of the reference ship (summarized with Table 4.1), and the theoretical findings made in Section 3.3.2. The clarifications are listed as follows:

- Depth of the water (h): the lower limit was set at 11 m based the design draft $T_{design} = 10.5\,m$ of the ship. The ship was presumed to operate at an 11 m draft occasionally, and hence any water depth below 11 m would risk grounding. The upper limit was set at $50m$ in order to impose a limitation on the size of the CFD domain, and keep it from becoming too large. Furthermore, the effects of shallow water appeared to start diminishing around the $h = 50\ m$ mark.
- Velocity of the vessel (v): The lower limit was intuitively set at 0 ms^{-1}. The upper limit was based on the design speed of the reference ship, $v_{design} = 15\,kn \rightarrow 7.8\,ms^{-1}$
- Draft of the ship (T): set between $[9,\ 11]m$ allowing a slight allowance from the T_{design} in both directions
- Depth to draft ratio (h/T): a lower limit was imposed following the experience-based instructions from DST, in order to eliminate the probability of non-converging simulation cases under $h/T \leq 1.2$. This would further ensure grounding of the ship is less probable
- Depth-based Froude number (Frh): According to the analysis of Figure 3.6, the

maximum feasible depth-based Froude number achieved by the reference ship would be $Frh_{design}{\approx}7.6$. However, the decision was taken to impose a maximum limitation at $Frh = 0.6$ to keep the scope of the SM in the far subcritical region. This would further guarantee the CFD calculations will not be burdened with extreme non-linearities.

Table 5.1: The lower and upper boundaries set on the basis of critical analysis on operational characteristics of the reference ship, and previous literature studies

Variable		$\text{Limit}_{\text{min}}$	$\text{Limit}_{\text{max}}$	Unit
Depth of the water	h	11.0	50.0	$[m]$
Draft of the ship	T	9.0	11.0	$[m]$
Velocity of the ship	v	0.0	7.8	$[ms^{-1}]$
Depth to draft ratio	h/T	1.2	–	$[-]$
Depth-based Froude number	Frh	–	0.6	$[-]$

The potential variable space made up of h, T and v values, but limited by the above boundaries is defined as the Domain of Interest (DoI) of the surrogate model.

5.2 Preprocessing of the initial dataset

At the onset of the surrogate development process, a complete dataset consisting of 56 CFD samples carrying resistance information of the reference ship was available. Unlike the CFD points used to validate the numerical setup in section 4.3, these points were calculated for the full-scale ship, enabling their direct adoption in surrogate development. The data was presented under two different drafts (T) values and six different depth-to-draft (h/T) ratios, in line with some prior model tests conducted on the reference ship. It is worth noting that the h/T parameter will be frequently used in the forthcoming sections of this thesis for data identification and classification. Furthermore, at this stage, the inclination was towards employing the added resistance coefficient(ΔC_T) as the independent predictive variable. Therefore, the immediate analyses are conducted on the basis of ΔC_T.

$$\Delta C_T = \frac{\Delta F}{\frac{1}{2}\rho v^2 s}$$

The distribution of the initial dataset with respect to h, T, v, and h/T variables is visualized by Figure 5.1. It is obvious that only the distribution of v represents at least half the domain of the variable space successfully. All the other variables are inadequately represented, either sparsely scattered as discrete values or small clusters within the respective variable space. Developing a Surrogate Model (SM) with such a weak initial dataset would lead to numerous problems such as prediction inaccuracies and overfitting as discussed in the state-of-the-art review. Nonetheless, it could merit investigating the capabilities of the dataset, as it constitutes a full-scale representation of systematic model tests previously conducted.

The Figure 5.2 illustrates how the sample points corresponding to each h/T value are interpolated as a cubic polynomial of the following form, with a_i representing the scaler weights of the interpolation:

$$\Delta C_{T_{cubic}} = a_0 + a_1 v + a_2 v^2 + a_3 v^3 \tag{5.1}$$

The decision to use a cubic function for the interpolation between velocity and added resistance coefficient was simply motivated by the first principle (rule of thumb) that exists within the maritime industry: the resistance of a ship is approximately proportional to the square or sometimes even the cube of the ship's velocity (MAN Energy Solutions, 2021). Figure 5.3 demonstrates the surfaces made by interpolating the cubic curves previously created in the aforementioned step (by interpolating through v values for each h/T). This interpolation was made to follow an exponential form and flexibly capture the non-linear curvature of shallow water resistance created by the variation of h (more specifically h/T in this context). When a, b and c are coefficients values for the best-fitting surface, the exponential interpolation follows the form:

$$\Delta C_{T_{exp}} = a \cdot e^{-b[h/T]} \tag{5.2}$$

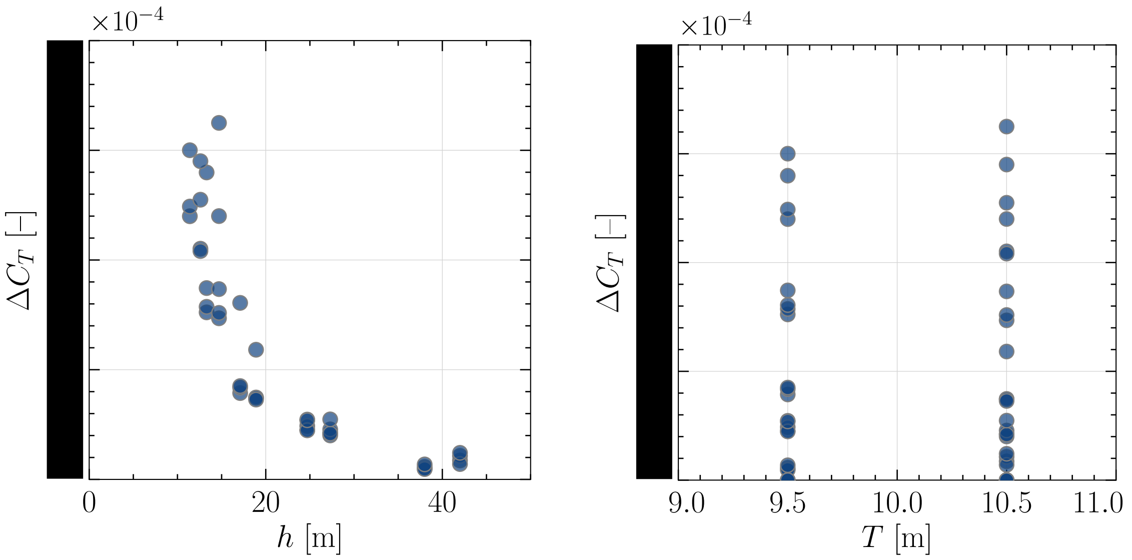

***(a)** Depth*

***(b)** Draft*

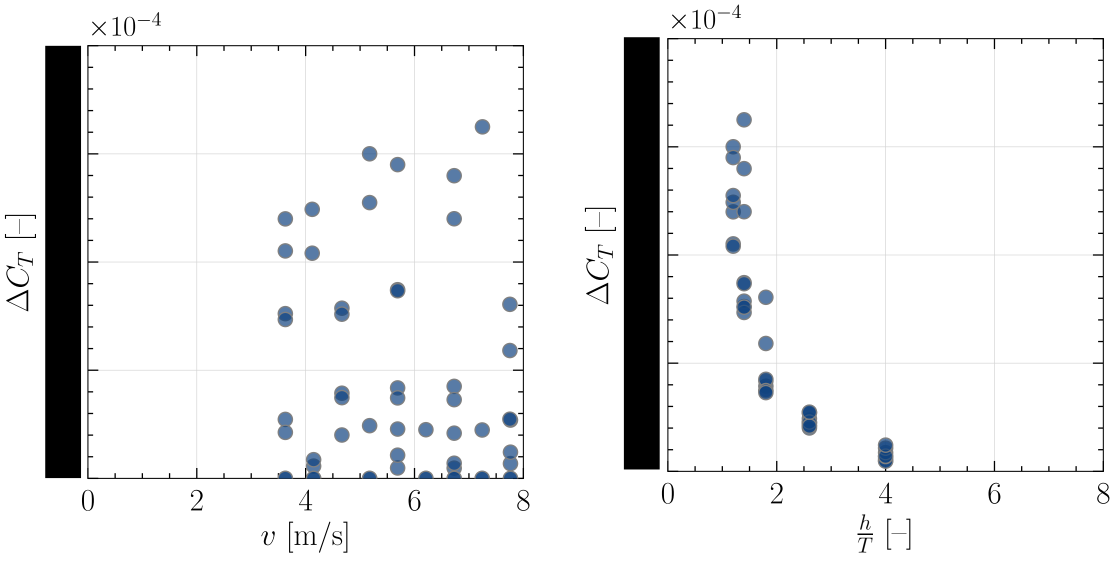

***(c)** Velocity*

***(d)** Depth to Draft ratio*

Figure 5.1: Distribution of the sample points of initial database in depth (h), draft (T), velocity (v) and depth to draft ratio (h/T) variable spaces

Although the initial dataset shows a highly sparse distribution across each variable domain (space), the cubic interpolation curves (Figure 5.2) appear to follow a general pattern that aligns with the theoretical findings on shallow water. For instance:

- at a high h/T values, the added resistance coefficient is close to zero, attesting that shallow water effects are negligible at greater depths.
- the gap between two adjacent h/T values increase with h, as shallow water effects become increasingly intense with decreasing depth.

At the same time, the exponential interpolation surfaces for the two draft values also demonstrate behaviours that reassure numerous theoretical and practical points.

- the added resistance coefficient starts to exponentially increase with the decreasing h. The ΔC_T values in regions with low velocity (v) and lower depth (h) are still higher than the ΔC_T values in regions with higher velocity (v) and higher depth (h). This conveys the idea that water depth is more influential than the vessel's velocity when it comes to added resistance due to shallow water.
- up until 25 m water depth, added resistance coefficient is very low. This validates the 50 m upper limit set on the water depth (h) variable. The added resistance starts to increase steeply at regions with low h and high v.

Overall, the two-step interpolation process led to the creation of a rudimentary mathematical model that could function as a basic response surface-based surrogate model on its own (predictions for different T values will be generated through linear interpolation). Upon further testing, this model was found to predict the added resistance coefficient with a relatively small error margin of 5% compared to the results obtained through CFD calculations, however, subjected to some strict limitations: $h = [11,\ 50]$, $T = [9.5,\ 10.5]$, $v = [0,\ 7.0]$, $Frh < 0.6$, $h/T > 1.2$.

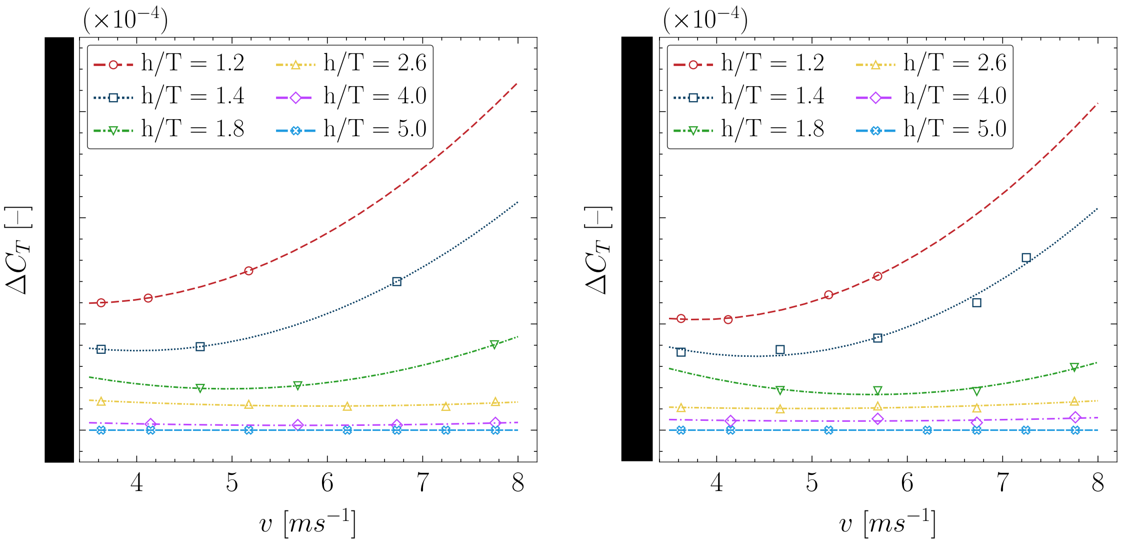

[redacted]

[redacted]

(a) $T = 9.5\,m$

(b) $T = 10.5\,m$

Figure 5.2: Curves created by the cubic interpolation of the initial sample points along v, for both $T = 9.5\,m$ and $T = 10.5\,m$ drafts and all the h/T categories

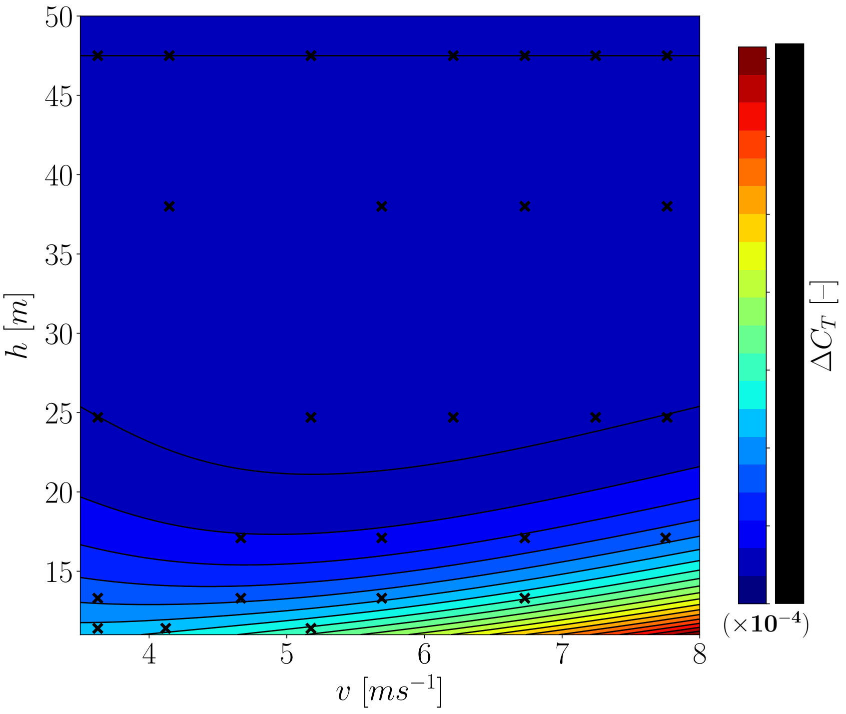

(a) $T = 9.5\,m$

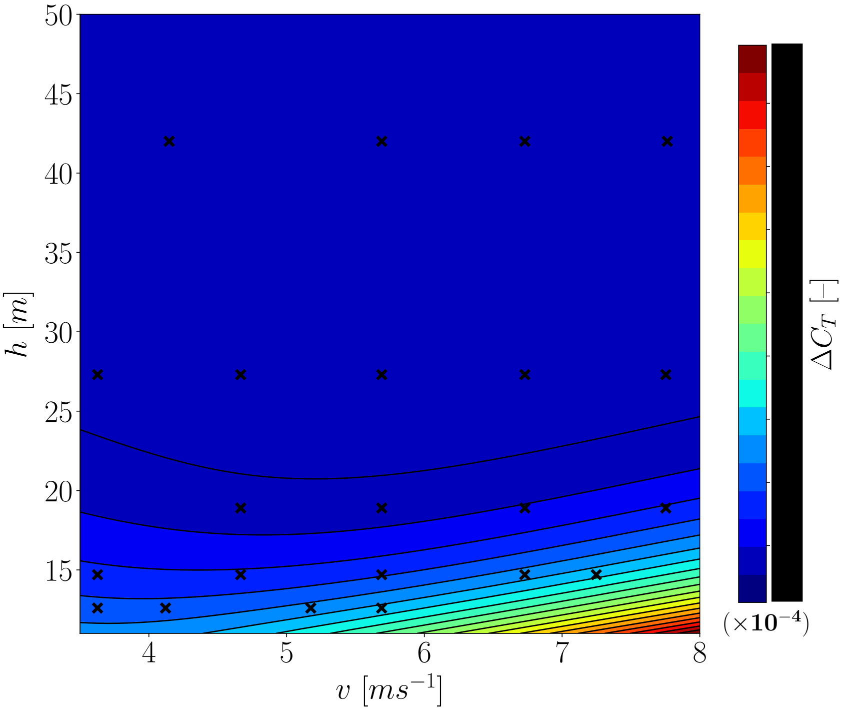

(b) $T = 10.5\,m$

Figure 5.3: Top view of the surfaces created by the logarithmic interpolation of the cubic interpolation curves belonging to all available h/T categories. The colour shading represents the ΔC_T magnitude and the sample points of the initial dataset are shown with ⟨✖⟩

It was decided to use this response surface to calculate added resistance, serving as a substitute for highly time-consuming CFD calculations. Given that computational capabilities are limited even on the High-Performance Cluster (HPC), and considering the time constraints, bottleneck situations are likely to arise in the future, especially when it is now proven that a larger training dataset is needed. However, as mentioned above, the accuracy of the model was only valid in a limited domain, thus it was not to be considered a prominent solution to address project objectives.

5.3 Generation of the extended dataset

Since the initial dataset was found to be falling short when representing the Domain of Interest (DoI) of the intended surrogate model, it became necessary to expand it with more added samples. Subsequently, an appropriate sampling method was required to facilitate this expansion. Among the sampling strategies discussed in the Section 2.1.2, ones like central composite design were deemed more suitable for optimization-based SMs as they were very methodical (Lu et al., 2021). But in this work, the SM would not be developed around one specific design point. Rather, as a prediction SM, the whole DoI would be important to keep its integrity throughout. Therefore, a simple randomized sampling strategy was decided to be used. Latin Hypercube Sampling (LHS) was identified as one of the most popular random sampling strategies used when developing SMs.

- LHS is a quasi-random sampling strategy. The randomized sample points generated by LHS are subjected to some conditions.
- Simply, the conditions of LHS dictate that, even though sample points are chosen randomly, they have to represent the whole DoI at the end.
- While a sampling strategy like SOBOL guarantees a more uniform distribution in the DoI according to Dige and Diwekar (2018), LHS sampling is superior at distributing sample points across the compound DoI made with all variables and along the space of each variable itself (overall better one-dimensional and multi-dimensional uniformity).
- There are combined methods that perform better with high-dimensional spaces with better efficiency (Latin Hypercube Hammersley Sampling) (Yasemin and Durmusoglu, 2022). But the intended SMs will be associated with only 3-independent and 1-dependent variables and a comparatively small number of sample points (in order of 1000s), thus the decision to use LHS was retained.

Algorithm 1 summarizes the process used to generate the extended initial dataset. As outlined in the section 2.3, `Python` was used to program most of the steps moving forward, unless otherwise stated. The `Python` programming language was particularly advantageous in this work, given the availability of numerous advanced libraries capable of executing algorithms like this. The number of samples (n) was set to 1000. The training dataset will ultimately contain an even lesser number of sample points after a part of the 1000 points is put aside for testing purposes (testing dataset). As concluded in the state-of-the-art analysis, such a training dataset would be small in comparison to very large training sets used in similar surrogate model development projects (see the analysis surrounding Figure 2.3). However, constrained to a very narrow timeframe, it was not feasible to aim for a larger dataset.

```
Algorithm 1: Latin Hypercube Sampling
Input: Number of samples $n$, Set of independent variables $X = [h, T, v]$
Input: Range of each variable np.array([[11, 50], [9, 11], [0, 7.8]])
Output: Matrix $X$ with $n$ random samples of each $h, T, v$ variable
Python packges import Pandas, numpy, lhs from pyDOE library
for $i \leftarrow 1$ to $n$ do
    for $j \leftarrow 1$ to $3$ do
        Pick a variable out of $[h, T, v]$ as $x_j$;
        Define the upper and lower boundaries based on the specific range;
        Partition the variable space of chosen variable $x_j$ into $n$ ranges of equal
          probability $1/n$;
        Generate a single random sample value $x_{j,j}$ for each range;
for $k \leftarrow 1$ to $n$ do
    Pick one random value from $n$ sample values generated for each
      $x_1, x_2, x_3 \mapsto [h, T, v]$ and combine them to generate $S_k$ sample;
    Append $S_k$ to $X$;
return $X$
```

Figure 5.4 simplifies the distributions of three main variables and the additions h/T variable in the generated dataset, as a pair-plot. The off-diagonal plots are presented with scatter distributions between pairs of those variables. These scatter plots covering the whole design space verify that the "space filling" characteristics of LHS sampling have been properly utilized. The diagonal plots are presented with the probability density function of each variable (h, T, v and h/T in that respective order). None of the probability distribution functions corresponds to a perfect Gaussian normal distribution. However, they can be roughly assumed as one[1]. If deemed required, these distributions could be transformed into close normal distributions thus the generated sample set was deemed acceptable.

5.3.1 Splitting of the extended dataset

As mentioned above, the complete initial dataset is not utilized to train the SM. A part of it is set aside to test the SM developed by the training set. In order to split the 1000-sample extended dataset, `sklearn.model_selection.train_test_split` Python library was used. The parameters were adjusted to have equally sized test/train sets at the end (50-50 split). The `train_test_split` library was able to split the initial dataset through a purely random selection, so it was highly probable that the roughly assumed Gaussian distribution for each variable was kept intact in training and testing subsets also. Later, the initial dataset was also appended to the training subset. From this point onward, these training/testing subsets will be directly addressed as "training dataset" and "testing dataset".

---

[1] For additional information, refer to https://www.mathworks.com

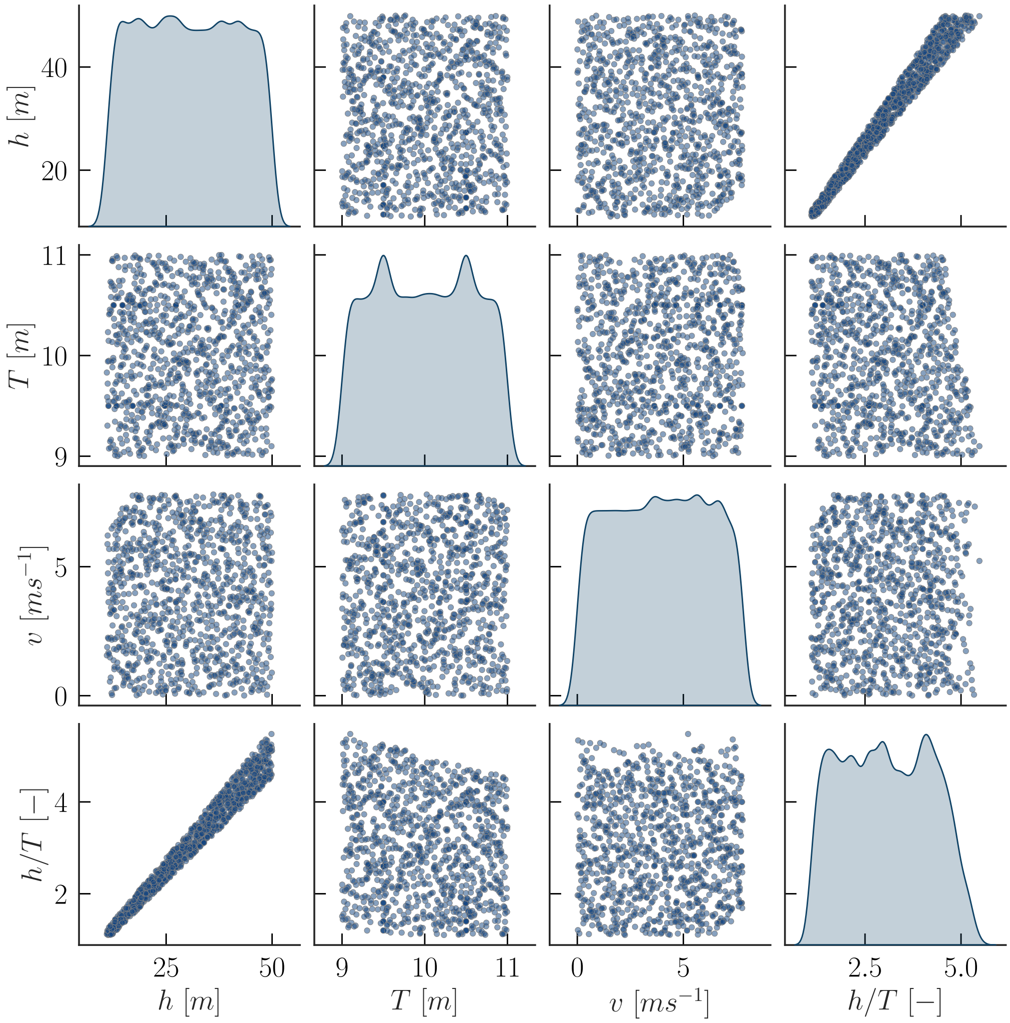

Figure 5.4: Pair-plot of the set of training samples generated with LHS and their probability density functions visualized along the diagonal

To complete the training/testing datasets, the added resistance (ΔC_T) was to be calculated for each sample. Having the "added" resistance in shallow water instead of the "simple absolute resistance" as the prediction variable imposed additional burdens in terms of computational time. For a given sample $[h_a, T_a, v_a]$, the corresponding resistance in deep water was also to be calculated (it was then subtracted from the shallow water resistance value to get the added resistance value). Generally, the water depth was set to around 365 m ($\approx 2\times$ ship length), a safe value that would exhibit negligible shallow water effects while preventing the computational domain from becoming excessively large, based on the recommendations from DST. Hence, for a single sample, the total calculation process would require the following steps:

$$
\begin{aligned}
CFD\,|_{h_a,v_a,T_a} &\Rightarrow F_{T,shallow} \\
CFD\,|_{365,v_a,T_a} &\Rightarrow F_{T,deep} \\
\Delta F_T\,|_{h_a,v_a,T_a} &= F_{T,shallow} - F_{T,deep}
\end{aligned}
\tag{5.3}
$$

While the CFD simulations were underway, with each simulation taking approximately 48 hours, a temporary workaround was employed to generate the ΔC_T values (which can be converted into ΔF_T easily) using the primary surrogate model developed in section 5.2. The primary SM was used to complete the training dataset and proceed with subsequent steps while overriding the heavy bottleneck caused by the lengthy CFD process. In the meantime, the completed CFD results would progressively replace the approximated ΔF_T values. This sub-optimal approach was mandatory to adopt with the very limited time available. Even though the accuracy of ΔF_T values predicted with the primary cubic-exponential SM were somewhat compromised (less than 5% error), the underlying trends and patterns in the data will be still captured by them. Ultimately, this will allow the development of a complete SM development framework to predict the added resistance in shallow water for the reference ship. The SMs created with this framework will be able to properly identify the linear and non-linear patterns between variables and model the whole shallow water resistance phenomena. Over time, as all the approximated ΔC_T values are gradually replaced with CFD results, the accuracy of the SM will further improve.

5.4 Standardization and normality transformation of variables

It is simply apparent that all the variables associated with the SM -independent and dependent alike- take only positive values. Only v can take negative values in an instance where the ship propels backwards, but such a specific scenario is not covered under the scope of intended SM. However, each variable can take values that can vastly differ in magnitude from one another. The 7^{th} and 18^{th} entries of the training dataset are presented with Table 5.2 to show how different these magnitudes can be. Having input variables with such different scales could lead to non-converging SM development algorithms and over-fitted SMs. Therefore, normalizing the scales of input variables can enhance the development process, interpretability, and accuracy of the intended SM (Davis, Cremaschi, and Eden, 2018; Khezri et al., 2021). As for the independent variable, pairing the scale normalization with a method that can transform the distribution of each variable into a Gaussian normal one, benefits will be further enhanced. According to the work done by Mittendorf (2023) and Fischer and Proppe (2023), a training set with normally distributed variables significantly enhanced the accuracy, while reducing the probability of overfitting.

Table 5.2: The 7^{th} and 18^{th} entries of the training dataset that shows the values of different magnitudes occupied by each variable

Entry	h $[m]$	T $[m]$	v $[ms^{-1}]$	ΔF_T $[kN]$	ΔC_T $[-]$
08	38.0	9.50	4.15	3.7	5.68E-05
18	17.1	9.51	6.73	73.1	4.25E-04

5.4.1 Standard scaler transformation of independent variables

According to the probability density functions of independent variables in the extended training dataset (refer to Figure 5.4), rough normal distributions were already evident. Also, it was assumed that this distribution was transferred to the training dataset through the purely randomized splitting process. The Python library `sklearn.preprocessing.StandardScaler` was used to normalize the scales of the variables with zero mean and unit variance. If the mean of all sample points in x variable space is μ and the standard deviation is σ, the transformation applied to x_i sample is,

$$z = \frac{x - \mu}{\sigma}$$

The values of independent variables corresponding to 7th and 18th entries after the transformation are tabulated in Table 5.3. It can be seen how the vastly different magnitudes seen in Table 5.2 are normalized across all variables (the values of two variables are not too far apart anymore).

Table 5.3: The 7th and 18th entries of the training dataset after the transformation

Entry	h $[m]$	T $[m]$	v $[ms^{-1}]$	F_T $[kN]$	C_T $[-]$
08	-1.698	-0.885	0.558	3.7	5.68E-05
18	-1.184	-0.886	1.712	73.1	4.25E-04

5.4.2 Normality transformation of dependent variable

The dependent variable was decided to be transformed into a standardized, but also a Gaussian normal distribution. Among many transformation techniques available in this regard, such as log transformation, and Box-Cox transformation, a method presented by Yeo and R. A. Johnson (2000) were frequently used in literature (Mittendorf, 2023; Lim et al., 2021). As a generalization of Box-Cox transformation, Yeo-Johnson does not demand a strictly-positive dataset, thus seemed optimal to deal with the dependent variables which could take zero values at high h values. A Python library was found for the Yeo-Johnson transformation (`scipy.stats.yeojohnson`), but the inverse transformation function was manually coded due to the unavailability of a dedicated library. Once the Yeo-Johnson transformation is applied to a particular dataset, the hyperparameter λ is returned. It should be reused in the inverse function to get the original values back.

$$x^{(\lambda)} = \begin{cases} \frac{[(x+1)^{\lambda}-1]}{\lambda} & \text{if } \lambda \neq 0, x \geq 0 \\ \ln(x+1) & \text{if } \lambda = 0, x \geq 0 \\ -\frac{[(-x+1)^{2}\lambda-1]}{2-\lambda} & \text{if } \lambda \neq 2, x < 0 \\ -\ln(-x+1) & \text{if } \lambda = 2, x < 0 \end{cases} \tag{5.4}$$

Figure 5.5 visualizes the distribution of two possible dependent variables ΔF_T and ΔC_T prior and after the Yeo-Johnson transformation. It can be seen that highly left-skewed initial distributions are transformed into close Gaussian normal distributions, making them more capable training sets.

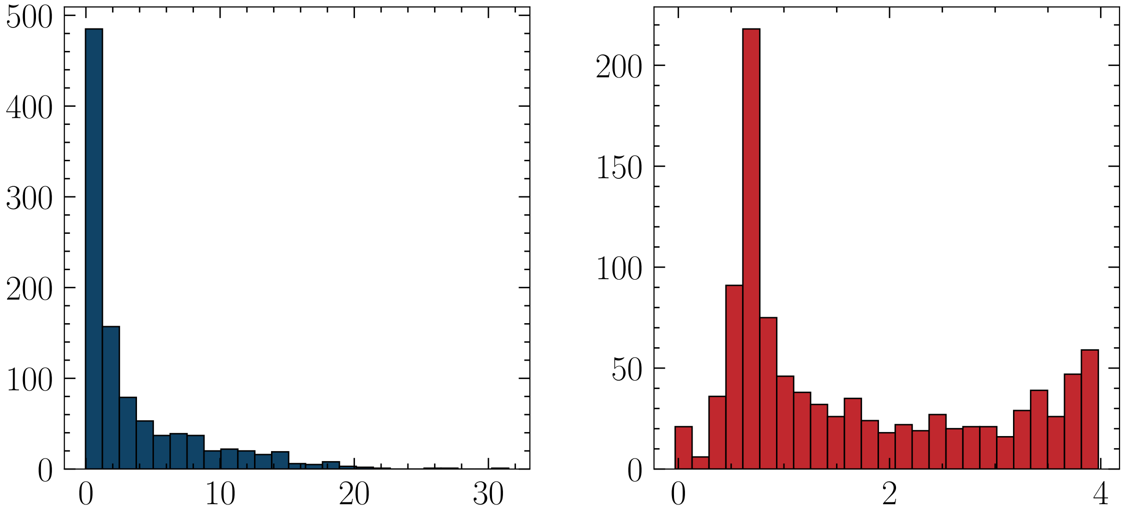

(a) *Initial* $\Delta C_T \times 10^{-4}$ $[-]$ ***(b)*** *Transformed* $\Delta C_T \times 10^{-4}$ $[-]$

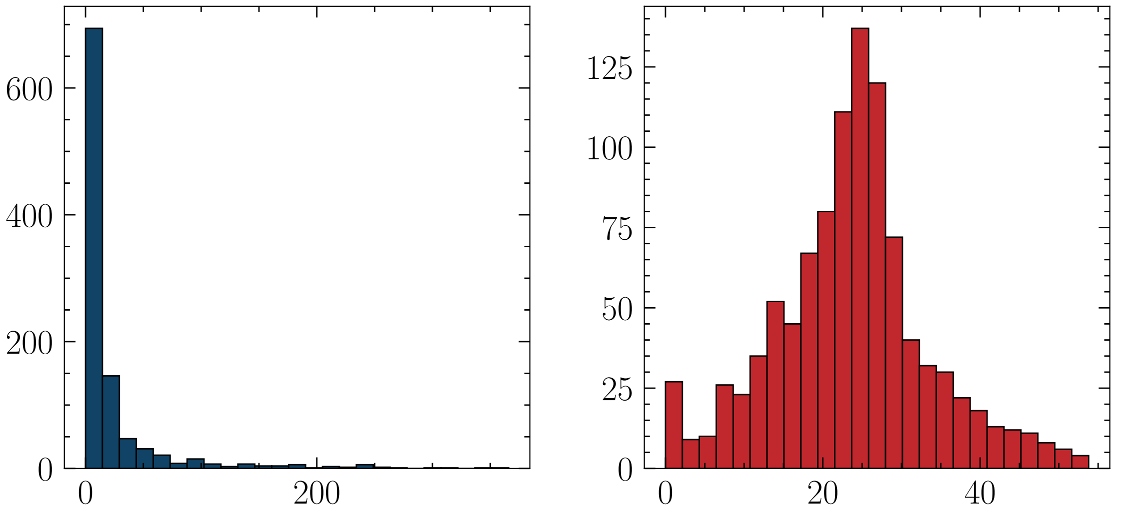

(c) *Initial* ΔF_T $[kN]$ ***(d)*** *Transformed* ΔF_T $[-]$

Figure 5.5: Comparison of the histogram distribution of possible dependent variables ΔC_T and ΔF_T in their,

- 🟦 Initial state
- 🟥 Yeo-Johnson transformed state

5.5 Feature expansion and selection

A Surrogate Model (SM) developed by using the three independent variables $\{h,\ T,\ v\}$ in their original linear form might not the best one in terms of accuracy and reliability. Since the shallow-water resistance is associated with non-linear patterns both with respect to the ship velocity (v) and water depth (h), the higher order forms of the initial independent variable could be better as independent variables of the SM. Feature expansion is simply the process used to expand original variables into all feasible combinations of their polynomial terms, to test this hypothesis. A third-order feature expansion was applied to the initial variable set as seen in Table 5.4. It should be remarked that expansion into rational powers was not considered to maintain simplicity. The third-order polynomial expansion resulted in 19 different variable combinations (features). Developing an SM with all of them as independent variables would be unnecessarily complex. At the same time counter-intuitive too since it is unlikely that all the variable forms that resulted in polynomial expansion would exhibit a strong relationship with the dependent variable.

Table 5.4: All the variable forms generated through the third-order polynomial feature expansion of initial three independent variables

Initial variables	x	xy	x^2	x^2y		xyz	x^3
Depth of water (h)	h	hT	h^2	h^2T	hv^2	hTv	h^3
Draft of the ship (T)	T	hv	v^2	hT^2	T^2v		h^3
Velocity of the ship (v)	v	Tv	T^2	h^2v	Tv^2		h^3

Therefore, selecting the most important features that possess a good relationship to the predictive variable and omitting the rest was to be done before the surrogate development. This process of choosing the most applicable set of features from a large pool of features is called feature expansion. Feature selection generally offers the following advantages (S. H. Kim and Boukouvala, 2020):

- Dimensionality reduction: when the engineering phenomena modelled by the SM is involved with a large number of independent variables, feature selection can be used to reduce the variable space, avoiding unnecessary complications in the development process
- Accuracy improvement of an SM: after eliminating irrelevant/redundant variables, the noise and unwanted bias will be removed from the SM
- Enhancing the interpretability: in an application like MARIDATA, the decision-making process would be more efficient if it is not clouded with irrelevant variables

Many methods were found in the literature to carry out feature selection. It was decided to use several of them and select the features based on their collective outcome.

5.5.1 Pearson correlation coefficient

Pearson correction coefficient, also known as bivariate correlation coefficient is a simple method of assessing the strength of the linear relationship between two variables. The state of linear correlation is indicated as a value between -1 and +1 when the Pearson formula is applied. (-1) corresponds to a perfectly negative linear relationship and (+1) corresponds to a perfectly positive linear relationship. Any of the Pearson coefficient values between the (-1 , +1) interval is corresponding to sub-perfect linear relationships with zero corresponding to a non-existing relationship between two variables. When the two variables are x and y, and number of samples available is n, and the Pearson coefficient is Pr,

$$Pr = \frac{n\sum xy - \left(\sum x\right)\left(\sum y\right)}{\sqrt{\left[n\sum x^2 - \left(\sum x\right)^2\right]\left[n\sum y^2 - \left(\sum y\right)^2\right]}} \tag{5.5}$$

The Python library `scipy.stats.pearsonr` was used to calculate the Pr between each feature and two potential predictive variables ΔF_T and ΔC_T.

5.5.2 LASSO L1 regularization

LASSO regression is a linear regression mechanism that is operated by adding penalty terms to weak correlations, ultimately forcing their importance to zero (Rehbach and Beielstein, 2019). The feature selection was carried out by letting the LASSO regularization fit a regression model between scaler-transformed independent variables and Yeo-Johnson-transformed dependent variable in the training dataset. The whole regression process is governed by the hyperparameter called α, and based on alpha value selection, two different approaches were available. With `sklearn.linear_model.Lasso` library, α was manually set to 0.0001 and the regression fit was assessed as the first step. With `sklearn.linear_model.LassoCV` library, α was set to be optimized using a grid search algorithm before generating the best fit. After both methods, the coefficient values assigned to each feature were examined.

5.5.3 Recursive feature elimination

Recursive Feature Elimination (RFE) selects the most important features through a backward selection algorithm. Unlike the previous two methods, the required number of features (n_R) can be specified in the beginning, and the result would be a list of rankings assigned to each feature with n_R most important features assigned the rank 1. The lowest ranking is assigned to the least important feature. The RFE algorithm was executed with the Python library `sklearn.feature_selection.RFE`.

5.5.4 Random Forests (RF) selector

Random Forests (RF) selector is a feature selecting tool integrated with the RF method used for SM development. Even though the RF method will probably not be used to develop the surrogate model, the recommendations of RF selector on important features would still be valid. The feature suggestions are made by identifying the underlying patterns between each feature and the dependent variables, thus those patterns are valid universally. For the feature selection procedure and extracting the selecting features, `sklearn.ensemble.RandomForestClassfier` and `sklearn.feature_selection` libraries were used.

5.5.5 Discussion of the feature selection

Feature selection was performed on both potential dependent variables, ΔC_T and ΔF_T. Except for the RF selector, all other feature selection methods provided either rankings or scores to indicate feature importance. The RF selector returned a list of the most important features. The normalized rankings and scores calculated by Pearson correlation, LASSO regularization with a manually chosen $\alpha \to 0.0001$, LASSO regularization with α optimized through grid search, and RFE are visualized in Figure 5.6. The features chosen by the RF selector are listed below.

$$\begin{array}{c|l} \Delta C_T & h, h^2, h^3, h^2 v \\ \\ \Delta F_T & h, h^2, h^3, h^2 T, v^2, v^3, Tv, T^2 v, Tv^2 \end{array}$$

Due to the distinct mechanisms used by each method, the scores assigned and features selected by each differed significantly. The aim was to consider all these results and intuitively select a set of independent variables. Key considerations:

- As a machine learning algorithm that is frequently used in SM development, the features selected by the RF were given more priority.
- Generally the first thing to notice is the rather higher overall scores associated with the ΔF_T. When the added resistance ΔF_T is non-dimensionalized as ΔC_T, additional v and wetted surface area (S) variables are added to the right side (Equation 4.15). This results in an implicit equation where independent variables v and T are available on both sides (T can directly influence S). Therefore, to simplify the surrogate model, it was decided to choose ΔF_T as the dependent (output/predictive) variable.
- As the intended SM is specific to one ship, using the non-dimensionalized added resistance is not necessary. In other words, added resistance need not be expressed in a non-dimensional form that normalizes across various ships. This insight further reinforced the decision to use ΔF_T.
- Shallow water resistance was found to vary non-linearly with v and h (findings of Section 3.3.2), prompting the selection of their higher-order forms.
- Therefore, the second- or third-order features of h and v were deemed more appropriate choices to effectively capture non-linear behaviours. The cubic feature of h^3 was chosen instead of h^2 since the shallow water resistance was found to be varying steeply with the water depth. Following this selection, all the features which contained lesser orders of h were eliminated. Due to the general belief of resistance being proportional to either the quadratic or cubic exponent of v (as mentioned in section 5.2 through the citation MAN Energy Solutions (2021)) both were deemed as viable options.
- The hull of the reference ship has a parallel, long, boxy midsection. It was assumed that variation in T would linearly modify the wetted surface area (S), hence skin friction drag. Consequently, T was kept in its linear form. Although the submerged

volume also would follow a close linear variation with the draft, pressure and wave-making drag would not demonstrate the same linear variation as the skin friction component. Despite this, the draft was still kept linear, since T was given higher scores than its higher orders, T^2 and T^3.

- Between T and v, combination Tv^2 was listed by the RF selector and scored higher by all 4 other methods. It was decided to choose it as a possible independent variable too.
- To summarize, it was decided to finalize ΔF_T as the dependent variable. Two different combinations were chosen as the independent variables. Both sets were viable options based on theoretical findings on hydrodynamics, general intuition and overall results of feature selection.

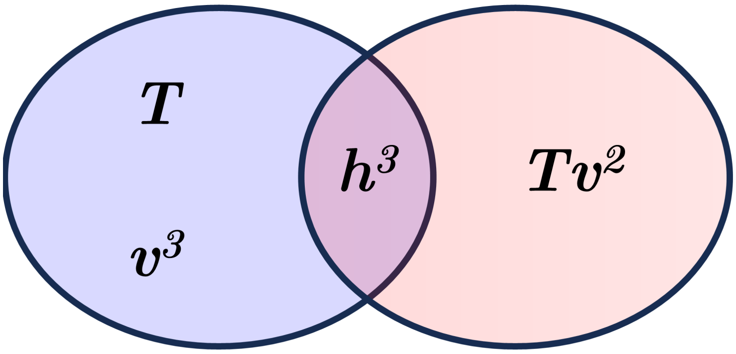

Set 1

Consists of all three initially intended variables, but T linear and h and v transformed into their cubic form.

Set 2

Consists of only two variables. T and quadratic form of v are combined together as a multiplication product

In the following steps, two distinct SMs will be constructed with a single SM development method. Each will employ one of the identified sets of independent variables, with ΔF_T serving as the dependent variable in each case. The performance of these two models will then be compared to determine which set of independent variables yields the best results. The expected terminology in the upcoming chapters is as follows.

- *(Independent) variable set 1/ Feature set 1/ Set 1*: The independent variable set representing $\{h^3, T, v^3\}$
- *Independent variable set 2/ Variable set 2/ Set 2*: The independent variable set representing $\{h^3, Tv^2\}$
- *Initial dataset*: The small dataset of 58 samples discussed in section 5.2 (mostly will be considered as a training dataset of its own)
- *Extended (training/test) dataset*: The two datasets created by splitting the large sample set generated using LHS in Section 5.3.1

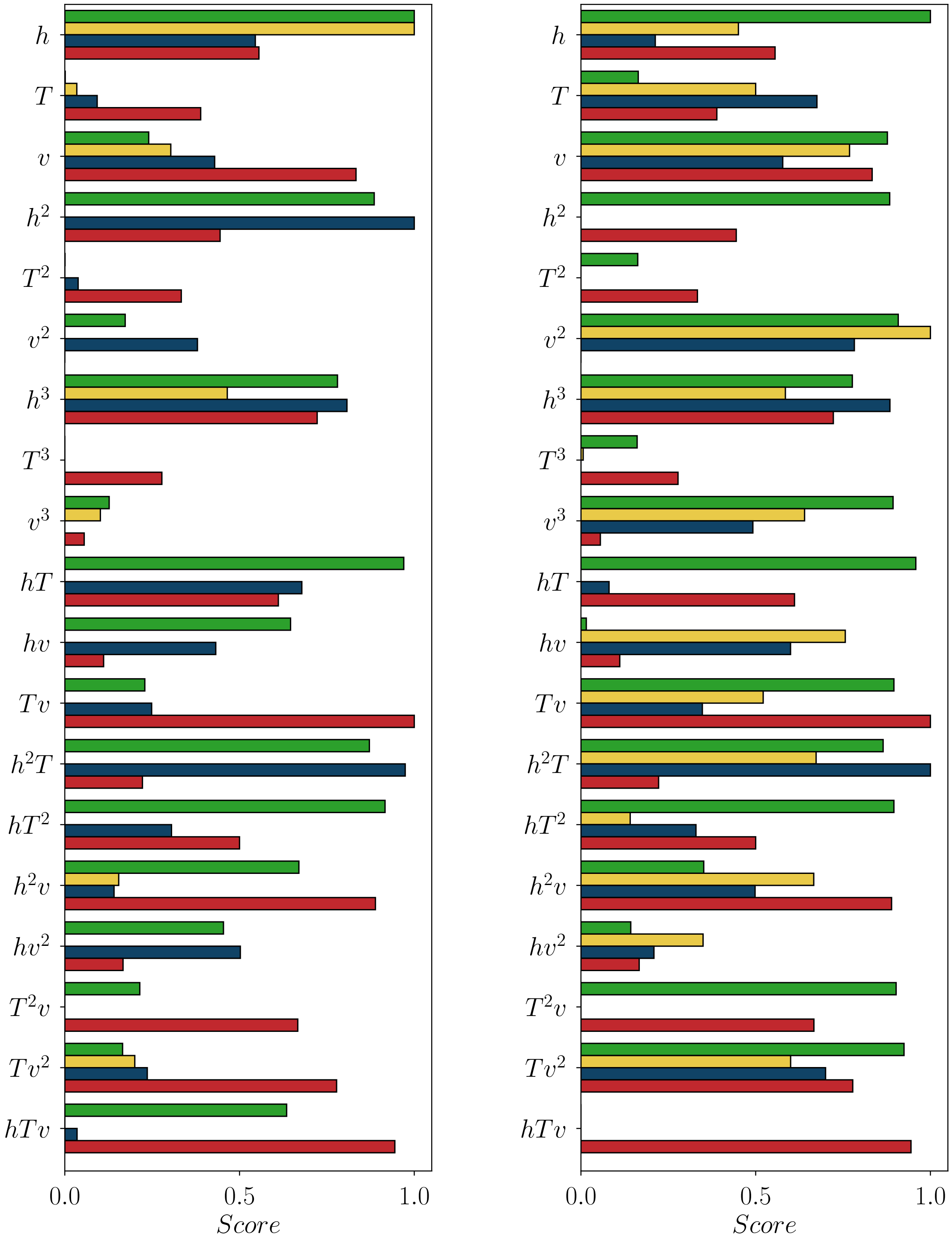

(a) ΔC_T ***(b)*** ΔF_T

Figure 5.6: Scores of feature importance normalized between the interval $\langle 0 \ \ 1 \rangle$, obtained through feature selection techniques,

- 🟥 Recursive feature elimination
- 🟦 LASSO L1 regularization ($\alpha \to \mathit{Optimized}$)
- 🟨 LASSO L1 regularization ($\alpha \to 0.0001$)
- 🟩 Pearson correlation

5.6 Concluding remarks

Some important points in the chapter that will lead up to the development of surrogate models are discussed.

- The Domain of Interest (DoI) of the intended surrogate model was set based on rational reasons. To summarize, $h \in \langle 11,\ 50 \rangle\ m$, $T \in \langle 9,\ 11 \rangle\ m$, $v \in \langle 0,\ 7.8 \rangle\ ms^{-1}$, $h/T > 1.2$, and $Frh < 0.6$.
- An initial dataset of complete 56 sample points was available at the beginning. However, the dataset was weak in representing the DoI for a machine learning-based surrogate model. Nevertheless, a primary response surface-based surrogate model developed through a combination of cubic and exponential interpolations between these points showed promising remarks of fairly accurate predictions.
- Due to the weak initial dataset, a proper training dataset was in demand. Latin Hypercube Sampling (LHS) sampling method was used to generate an extended dataset of 1000 sample points successfully covering the DoI. Later, it was split into two equal-sized training and testing datasets.
- To even the scales between different variable values, standard scaler transformation was applied to all independent variables in the extended training dataset. Subsequently, the Yeo-Johnson transformation was applied to the dependent variables to assume a Gaussian normal distribution.
- Results of five different feature selection methods were analysed with previous theoretical findings and general intuition to finalize two separate independent variable combinations; Set 01 $\{h^3,\ T,\ v^3\}$ and Set 02 $\{h^3,\ Tv^2\}$. The same findings also led to the conclusion that ΔF_T should be the dependent variable for the intended SM.

CHAPTER

Development of the surrogate model

6

The chapter is dedicated to explaining the process of developing the base surrogate model following preprocessing of the data, selection of variables steps and further tuning.

6.1 Kriging and ANN surrogate modelling techniques

Given the prevalent use of Kriging and Artificial Neural Networks (ANN) methodologies in the relevant resistance/power-related naval architecture literature (see discussions pertaining to Figure 2.3), it was decided to use both of them to develop the SMs, to assess and contrast their performance. As previously underscored, ANN is not a direct Response Surface (RS) method, but a machine learning algorithm that can demonstrate similar performance to RS methods on the surface. Hence, the definition of RS has been applied rather flexibly, encompassing the ANN methodology as well.

6.1.1 Kriging method

Kriging is a powerful machine learning tool that integrates the characteristics of Gaussian Process Regression (GPR) to carry out regression analysis. Recognized as a flexible algorithm, Kriging is proficient at discerning underlying patterns between a series of spatially or temporally distributed random data points, related to a certain phenomena (stochastic data) and interpolating between those data points (Erickson, Ankenman, and Sanchez, 2018). These stochastic data points carry information on multiple dimensions of input variables and their corresponding response. In the context of this project, the training dataset encompasses numerous combinations of h, T, and v as input variables, with the added resistance in shallow water experienced by the reference ship serving as the output response variable. Kriging method assumes that there exists a relationship between the datapoints belonging to any subset of the training dataset, and generates a Surrogate Model (SM) to mathematically represent that relationship. Since the GPR-based Kriging method assumes the physical phenomena represented by the training dataset as a Gaussian process -a stochastic process with a multivariate Gaussian normal distribution- the scaler and normality transformations carried out on the independent/dependent variables were proven to be a good preprocessing decision. The prediction at any point is calculated with the combination of two terms, the mean value of the Gaussian process at that point (determined by the mean function) and a deviation term determined by the covariance function.

- Mean function ($\mu(x)$): represents the expected value of mean/average of a Gaussian process at any given point. The GPR-based regression model was employed as the specific version named ordinary Kriging, which assumed a constant, yet unknown mean values for specific local regions of the DoI (Daya and Bejari, 2015). The local constant mean was to be calculated. Ordinary Kriging has proven to boast better accuracy compared to simple or universal Kriging models in many engineering applications (Kleijnen, 2009; Kleijnen, 2017).
- Covariance function (δ): adds on top of the mean and defines the overall smoothness of the Kriging response surface. It generally defines the relationship between input and output variables along the DoI. Therefore, a combination of independent variable values within the DoI is fed into the covariance function, it calculates the deviation of corresponding output values (independent variable value) with respect to the mean. The covariance function is also known as the kernel of the Kriging process.

6.1.1.1 Ordinary Kriging framwork

When an already calculated sample set (training dataset) m number of samples is available in the form $y = G(\mathbf{x})$,

- Independent and dependent variable samples can be represented as follows. Here x_i is a single vector containing n number of variables.

$$\begin{aligned} X &= (\mathrm{x}_1, \mathrm{x}_2, \dots, \mathrm{x}_m)^\top \\ y &= (\mathrm{y}_1, \mathrm{y}_2, \dots, \mathrm{y}_m)^\top \\ &= (G(\mathrm{x}_1), G(\mathrm{x}_2), \dots, G(\mathrm{x}_m))^\top \end{aligned} \tag{6.1}$$

- The Kriging model is defined by the combination of mean and covariance functions as follows. $\hat{y}$ is the value of the dependent variable as predicted by the model.

$$\begin{aligned} y(x) &\sim \mathcal{GP}\left(\mu(x), \mu\left(x, x'\right)\right), \\ \hat{y}(x) &= \mu(x) + \delta(x) \end{aligned} \tag{6.2}$$

- In ordinary Kriging, the locally constant man function is represented as a linear combination of β constant coefficients and $f(x)$ known functions, all are determined by the Kriging protocol to minimize the error of estimation (of $\hat{y}(x)$).

$$\mu(x) = \sum_{j=1}^{n} \beta_j f_j(x) \tag{6.3}$$

- Covariance function is represented as a matrix that contains the relationship between all possible pairs of input variable samples.

$$\delta_{ij} = \delta\left(x_i, x_j\right) = \mathrm{Cov}\left[\delta\left(\mathrm{x}_i\right), \delta\left(\mathrm{x}_j\right)\right] = \sigma^2 \mathcal{R}\left(\mathrm{x}_i, \mathrm{x}_j\right) \tag{6.4}$$

- σ^2 is the process variance, where σ_{ij} is standard deviation between x_i and x_j sample vectors. $\mathcal{R}\left(\mathrm{x}_i, \mathrm{x}_j\right)$ is a unique function based on the kernel chosen for the Kriging model. Finally, the covariance matrix takes the form,

$$\delta = \begin{bmatrix} \delta\left(x_1, x_1\right) & \cdots & \delta\left(x_1, x_N\right) \\ \vdots & \ddots & \vdots \\ \delta\left(x_N, x_1\right) & \cdots & \delta\left(x_N, x_N\right) \end{bmatrix} \tag{6.5}$$

6.1.1.2 Kriging kernels and covariance functions

The kernels are defined at the beginning of Kriging initiation. Each kernel carries different covariance functions which boast different qualities. As the mean function is assumed to be constant within local regions (implying a flat surface), the shape and smoothness of the final RS, and consequently the SM, are determined by the covariance function defined by the kernel. The following list summarizes 5 commonly used Kriging kernels (Beckers, 2021; Cui, Pagendam, and Gilfedder, 2021). Here, $h = \left\|x_i - x_j\right\|$ is the Euclidean distance between two sample points, and l is the length parameter that decides how far away the influence of a single sample extends[1].

- Constant kernel: Assumes a constant value for the covariance at any point within DoI.

$$\mathcal{R}\left(\mathrm{x}_i, \mathrm{x}_j\right) = k \ \forall x_i, x_j$$

- White kernel: Specifically used to represent the noise existing in the training dataset. When σ_n^2 is the covariance of noise, and $\delta(x_i, x_j)$ is Kronecker delta,

$$\mathcal{R}\left(\mathrm{x}_i, \mathrm{x}_j\right) = \sigma_n^2 \delta\left(x_i, x_j\right)$$

- Radial Basis Function (RBF): Also known as Gaussian/squared exponential kernel, a popular choice due to its smoothness.

$$\mathcal{R}\left(\mathrm{x}_i, \mathrm{x}_j\right) = \exp\left(-\frac{1}{2l^2}\left\|x_i - x_j\right\|^2\right)$$

- Matérn Kernel: another generalised version of RBF kernel, Matérn Kernel is integrated with the parameter ν that allows controlling of the smoothness. When $\nu \to \infty$, RBF kernel is returned,

$$k\left(x_i, x_j\right) = \frac{1}{\Gamma(\nu)2^{\nu-1}}\left(\frac{\sqrt{2\nu}}{l} d\left(x_i, x_j\right)\right)^{\nu} K_\nu\left(\frac{\sqrt{2\nu}}{l} d\left(x_i, x_j\right)\right) \tag{6.6}$$

---

[1] For additional information, refer to https://scikit-learn.org/stable/modules/gaussian_process.html

6.1.2 Artificial Neural Networks (ANN)

Artificial Neural Networkss are computational models inspired by the operational patterns of biological neural networks found in animals. Analogous to a complex animal brain, ANNs employ interlinked information channels which function as neurons. These pathways are arranged in single or multiple layers. Each neuron pathway can receive an input, perform a computation, and subsequently output the result of that computation. These calculations include matrix manipulation, modelling non-linearities through activation functions, and basic arithmetic operations. When a large number of such neurons work together, each executes some kind of mathematical operation; a sophisticated system is established, equipped to handle an extensive range of tasks. These tasks include classification with missing inputs, synthesis and sampling, regression, prediction, anomaly detection, and many others that are challenging to execute via straightforward programming scripts devised by humans.

In this project, particular architecture of ANN called Multi-Layer Perceptron (MLP) will be used to develop the SM. The neurons in MLP ANNs are arranged in three primary layers, namely, the input layer, the hidden layer, and the output layer. If explained from the SM perspective, every neuron in the hidden layer will receive data from all the neurons in the preceding hidden layer, with the first hidden layer receiving data directly from the input layer. However, in each instance, a neuron transmits the data forward as a linear weighted combination, the weights of which are determined based on the information learnt from preceding hidden layers. Finally, the output layer receives data from the last hidden layer, combines them linearly, and delivers the final outcome. The coefficients of the linear regression act as weights that represent the feature importance of each independent variable. When the non-linearities need to be added, the weighted combination is squeezed through an entity known as an activation function, which adds curvature to the linear model (Abinaya and Devi, 2022). The versatility of ANNs is validated by the Universal Approximation theorem, which dictates that any continuous function can be modelled with an ANN with at least a single layer (Goodfellow, Bengio, and Courville, 2016). The following Figure 6.1 provides a simple schematic on the mechanism of an MLP ANN.

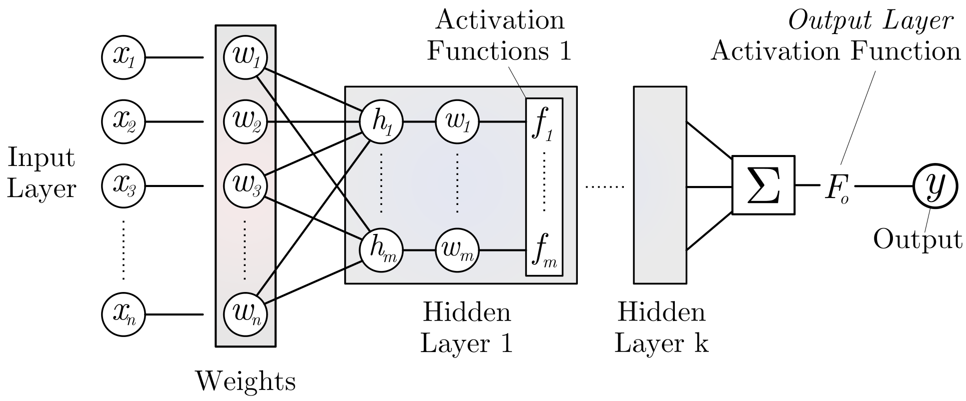

Figure 6.1: Schematic layout of a typical MLP-based ANN model with multiple layers and activation functions established after each layer, inspired by D.-H. Lee, Y.-T. Kim, and S.-R. Lee (2020); and Razavipour et al. (2022)

6.1.2.1 Activation functions used in ANNs

Activation functions are used to induce non-linearities to the layer outputs formed as linear weighted combinations. Based on the arrangement of the ANN, activation functions are used only before the output layer, or following each hidden layer as well as before the output layer (Dubey, Singh, and Chaudhuri, 2022).

- Linear functions: as the name suggests, only used to scale the output. The linearity of the output is preserved, thus only used in rudimentary models.

$$f(x) = x$$

- Sigmoid functions: scale up or down the weighted combined output into a value between the interval [0, 1]. This value can be identified as a representation of probability or confidence. Moreover, since all the output values are modified between 0 and 1, normalization across all layers is achieved.

$$f(x) = \frac{1}{1 + e^{-x}}$$

- Tanh function: also known as the hyperbolic tangent activation function, maps the outputs between the interval [−1, 1]. Since negative values are allowed, and the range is symmetric around zero, more versatile than the Sigmoid function.

$$f(x) = \tanh(x) = \frac{e^{x} - e^{-x}}{e^{x} + e^{-x}}$$

- Rectified Linear Unit (ReLU) function: sets all negative outputs to zero. When the desired output is certain to be a positive value, the outputs of some neurons will be set to zero, which accelerates the learning process. With zeroed-out values in the middle, the final output will be piecewise linear, which can act as a non-linearity.

$$f(x) = \max(0, x)$$

- Softmax function: mostly used in classification problems. Scales the output between the interval [0, 1], and creates a probability density function.

$$\sigma(x)_j = \frac{e^{x_j}}{\sum_{k=1}^{K} e^{x_k}} \quad \text{for } j = 1, \ldots, K$$

6.2 Development of the base and optimized surrogate models

6.2.1 Base surrogate models

Base surrogate models were established utilizing both the initial dataset (56 samples) and the extended training dataset (≈500+56 samples), separately. As explained throughout the report, the simple procedure was to feed the training dataset into the surrogate development algorithm in a Python environment. The result was a surrogate model that has "learnt" to interpolate between the training data points by recognizing the underlying patterns between variables. No hyperparameters were optimized for the baseline models. The values of independent variables $\{h, T, v\}$ were modified to represent the form of variable sets chosen through the feature selection, set 1: $\{h^3, T, v^3\}$ and set 2: $\{h^3, Tv^2\}$. The normalization transformation (scaler transformation) was then applied to both independent variable sets, followed by the application of normality transformation (Yeo-Johnson) to the dependent variable ΔF_T.

In order to predict the ΔF_T values corresponding to the sample set $\{h_s, T_s, v_s\}$ using a developed surrogate model, a specific protocol was to be followed; (1) deciding which SM developed with which independent variable set should be used, (2) converting the $\{h_s, T_s, v_s\}$ values to either $\{h_s^3, T_s, v_s^3\}$ or $\{h_s^3, T_s v_s^2\}$ based on the choice, (3) use the same exact scaler transformation used on them at the beginning of surrogate development, (4) feed the values to SM and get the prediction, and finally (5) apply inverse Yeo-Johnson transformation with the same λ hyperparameter used at the beginning to get the predicted ΔF_T value in real scale. The `sklearn.gaussian_process.GaussianProcessRegressor` library was used to establish the Kriging SM and `sklearn.neural_network.MLPRegressor` library was used for the MLP ANN model.

6.2.2 Performance validation criteria

Among the performance evaluation methods described in Table 2.1, Coefficient of Determination (CoD) (r^2) was decided to be used to evaluate the performance. Basically, the predictions were generated for all the independent variable combinations available in the testing dataset, and each predicted value was compared against its CFD calculated counterpart (or the value evaluated with cubic-exponential primary SM). The output of r^2 is a score between $[0,\ 1]$, where the highest represents a perfect correlation. The normalized performance score facilitates the convenience of comparing different surrogate models. Thus, r^2 has been used in numerous surrogate development projects such as Cai et al. (2021) and Xu et al. (2021). The equation of r^2 is repeated below for convenience, where y_i is the true value, $\hat{y}_i$ is the predicted value, $\bar{y}$ is the mean of the true values and n is the number of samples in the test dataset. `sklearn.metrics.r2_score` library was used to conveniently calculate r^2 values.

$$R^2 = 1 - \frac{\sum_{i=1}^{N_{\text{test}}} \left(y_i - \hat{y}_i\right)^2}{\sum_{i=1}^{N_{\text{test}}} \left(y_i - \bar{y}\right)^2} \tag{6.7}$$

6.2.3 Stacking regressor and hyperparameter optimization

With the purpose of defining further optimized series of SMs from baseline models, the methods of stacking and hyperparameter optimisation were adopted.

6.2.3.1 Kernel definition for Kriging SMs

The standard kernel for GPR-based Kriging models is the Radial Basis Function (RBF) kernel with hyperparameter length scale $l = 1$. However, it was later decided to merge the RBF kernel with the White kernel to infuse noise management properties into the Kriging model. Kernels can be combined with simple summing or even multiplication, and the former option was chosen for simplicity (Cui, Pagendam, and Gilfedder, 2021). The hyperparameter of the White kernel (*noise_level*) serves as an indicator of the kernel's sensitivity to noise and was originally kept at $noise\_level = 1$. During the hyperparameter optimization phase, both l and *noise_level* were also considered for tuning, among other parameters. The Kriging SM definition with default hyperparameters is stated as follows. Note that this definition is applicable to both Kriging models developed with both independent variable sets.

```
GaussianProcessRegressor(kernel= RBF(length_scale=1)
                                     + WhiteKernel(noise_level=1))
```

6.2.3.2 Process and results of hyperparameter optimization

The randomized search optimization algorithm was used to evaluate the best set of hyperparameters for both Kriging and ANN SMs created from both independent variable sets. The preference was set on the randomized search algorithm for the optimization process over the other popular algorithm grid search mainly due to its reduced processing time. Moreover, the randomized search has been found to offer greater flexibility and exploration capabilities than grid search (Yang and Shami, 2020). In order to execute the algorithm, the `sklearn.model_selection.RandomizedSearchCV` library was used. Within the algorithm, a number of random hyperparameter combinations are created based on a predefined number of iterations (n_iter). Then SMs are developed corresponding to each combination and their performances are compared. The model development and evaluation criteria were set to be carried out with the five-fold cross-validation scheme complimented with the mean square error parameter selected. Finally, the hyperparameter values corresponding to the best performing SM were selected.

Figure 6.2 visualizes the flow chart of the randomised search hyperparameter optimization process for the Kriging SM. Hyperparameter bounds set at the initiation are also listed in the figure. Besides the l and *noise_level* parameters linked with kernel definition, the "alpha" parameter influences the SM's robustness against noise, and the "optimizer" parameter decides whether to employ the Broyden–Fletcher–Goldfarb–Shanno (BFGS) minimization algorithm to determine the form of the covariance function. As for the activation function options of the ANN model, Tanh and ReLU functions were chosen. Tanh was preferred for its versatile operation compared to the Sigmoid function, while ReLu was chosen considering that ΔF_T would always be a positive value within the DoI. The optimized hyperparameters corresponding to the extended training dataset are tabulated in Table 6.1[1] .

---

[1] To read more about the additional hyperparameters which were not extensively discussed in the re-

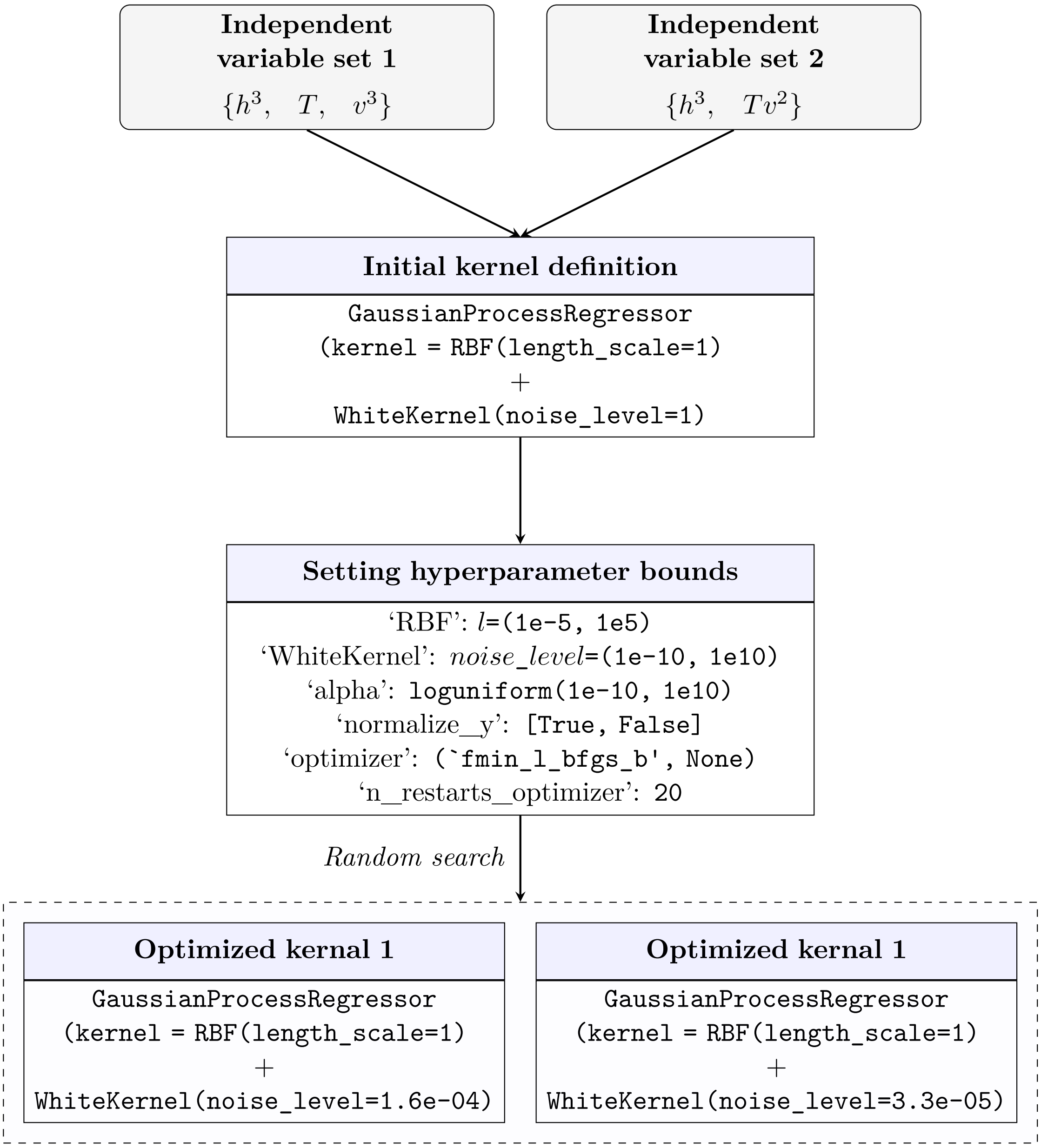

```
GaussianProcessRegressor
(kernel = RBF(length_scale=1)
+
WhiteKernel(noise_level=1)
```

‘RBF’: l=`(1e-5, 1e5)`
‘WhiteKernel’: *noise_level*=`(1e-10, 1e10)`
‘alpha’: `loguniform(1e-10, 1e10)`
‘normalize_y’: `[True, False]`
‘optimizer’: ``(`fmin_l_bfgs_b', None)``
‘n_restarts_optimizer’: `20`

```
GaussianProcessRegressor
(kernel = RBF(length_scale=1)
+
WhiteKernel(noise_level=1.6e-04)
```

```
GaussianProcessRegressor
(kernel = RBF(length_scale=1)
+
WhiteKernel(noise_level=3.3e-05)
```

Figure 6.2: Flowchart of the hyperparameter optimization process carried out using the five-fold cross-validation scheme and kernel definitions before and after the optimization. The specific values correspond to the Kriging SMs developed with an extended training dataset

Table 6.1: Summarization of the result of the hyperparameter optimization process for both Kriging and ANN surrogate models associated with independent variable sets: Set 1 $\{h^3, T, v^3\}$ and Set 2 $\{h^3, Tv^2\}$. Note that these values are corresponding to the SMs developed using the extended training set.

Hyperparameter	Defaul value	Bounds	Optimized value	
			Set 1	*Set 2*
		Kriging model		
length_scale	1	[1e-5, 1e5]	1.6e-04	3.3e-05
noise_level	1	[1e-10, 1e10]	1	1
alpha	1e-10	[1e-10, 1e10]	1e-8	1e-7
normalize_y	False	[True, False]	True	True
optimizer	None	[fmin_l_bfgs_b, None]	None	None
		ANN Model		
hidden_layers	64	[64, 256]	256	64
activation	relu	[relu, tanh]	relu	tanh
alpha	0.001	[0.0001, 0.01]	0.0001	0.0001
learning_rate	constant	[constant, adaptive]	adaptive	adaptive
learning_rate	0.001	[0.001, 0.1]	0.01	0.01
max_iter	100	[100, 300]	100	200

6.2.3.3 Stacking of surrogate models

Stacking, also known as stacked generalization is a machine learning algorithm used to improve the performance of a pre-established set of SMs. As the name suggests, the parent SMs are “stacked” or combined to create a consolidated meta-model. It is expected that, after learning the patterns from all the parent models, the meta-model would have enhanced capabilities of prediction (B. T. Bartz, 2016). The combination of parent models can be carried out through known SM methods such as linear regression, Random Forests (RF) regression, etc. The stacking model was developed using the `sklearn.ensemble.StackingRegressor` library. Here, stacking was applied solely to the hyperparameter-optimized SMs, with the Kriging and ANN models developed using the two sets of independent variables separately stacked together.

---

port, please refer to Yang and Shami (2020), https://scikit-learn.org/gaussian_process.html, and https://scikit-learn.org/sklearn.neural_network.MLPRegressor.html

6.3 Results and discussion

The final representation, performances, and limitations of the base surrogate models (SMs) develop with Kriging and ANN methods are discussed in the chapter. Due to the small size (56 samples), only the Kriging method was used to develop SM with the initial dataset. However, both Kriging and ANN methods were used to develop SMs using the extended training dataset ($\approx$500+56 samples). All the models were evaluated for performance using the Coefficient of Determination (CoD) (r^2) criteria, against the extended testing dataset (500 samples).

6.3.1 Inconsistencies in Kriging SMs trained on initial dataset

Even though it was established in section 5.2 that the initial dataset was too sparse to perform as a capable training set, two SMs were developed with the intention of analysing how a weak training set would impact the final outcome. The attempt to incorporate ANN failed due to the non-converging development process, possibly due to the sparse nature of the dataset. The Kriging SMs developed are depicted in Figure 6.3 and Figure 6.4. Representing the SMs in a standardized 3-dimensional graphical form was quite challenging at first, since the ones corresponding to the independent variable set 1 had four dimensions $\{h^2, T, v^3, \Delta F_T\}$. Ultimately, the decision was made to fix the T value and represent the models with h and v in x and y axes, while ΔF_T is represented in the z axis. To facilitate the convenience of reading the plots, the ΔF_T value is represented as a colour map. The standard `Jet` colourmap available with `matplotlib.colors.ListedColormap` library was used.

The behaviour of the SMs for $T = 9.5\ m$ and $T = 10.5\ m$ shows several characteristics that contradict the theoretical and literature findings made in earlier chapters. At the same time, some sensible characteristics were observed too. For instance,

- ΔF_T value corresponding to a given v value is kept constant throughout the whole h range. This means that water depth has no influence on the added resistance, which clearly violates shallow water hydrodynamic theories.
- SMs developed with both independent variables exhibit the same behaviour at both draft values. They start from $\Delta F_T = 0\ kN$ when $v = 0\ ms^{-1}$ and establish maxima close to $v \approx [6,\ 7] ms^{-1}$ interval, then drops steeply.
- As previously discussed in relation to Figure 3.6, the far subcritical region, where the Domain of Interest (DoI) of the SM belongs, does not contain a maxima. The whole form of the SM model is therefore invalidated due to the existing maxima around higher v values.
- At very low v values, the ship experience little to no resistance due to the negligible relative motion between the hull and water, irrespective of the water depth, $\lim_{v \to 0} \Delta F_T = 0$. This property is somehow established in both models developed with both independent variable sets, at both draft values.

Aside from adhering to the zero boundary condition at $v = 0\ ms^{-1}$, the SMs developed from the initial dataset largely violates rules of shallow water hydrodynamics. The use of an extended training set was decided to be adopted in future steps.

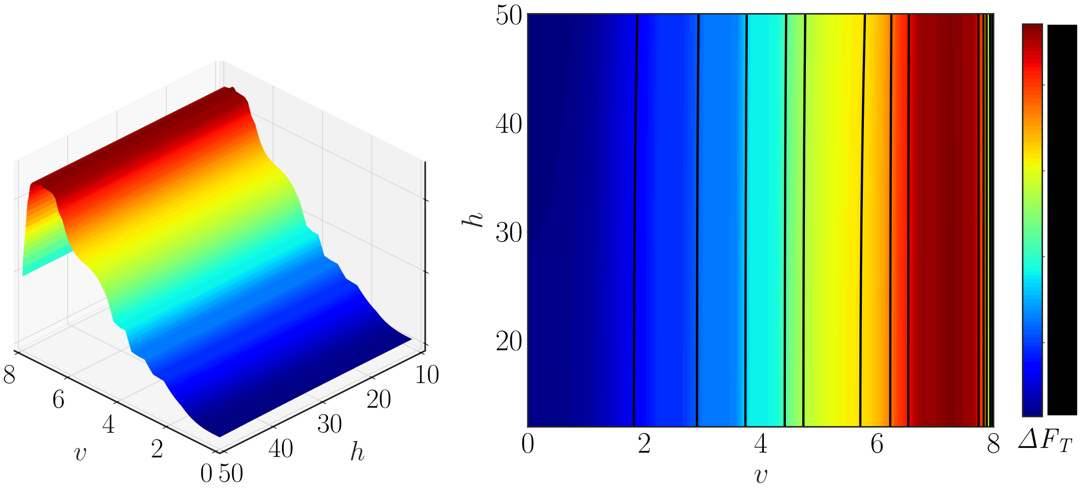

(a) *3D surface for* $\{h^3, T, v^3\}$ ***(b)*** *Contour plot for* $\{h^3, T, v^3\}$

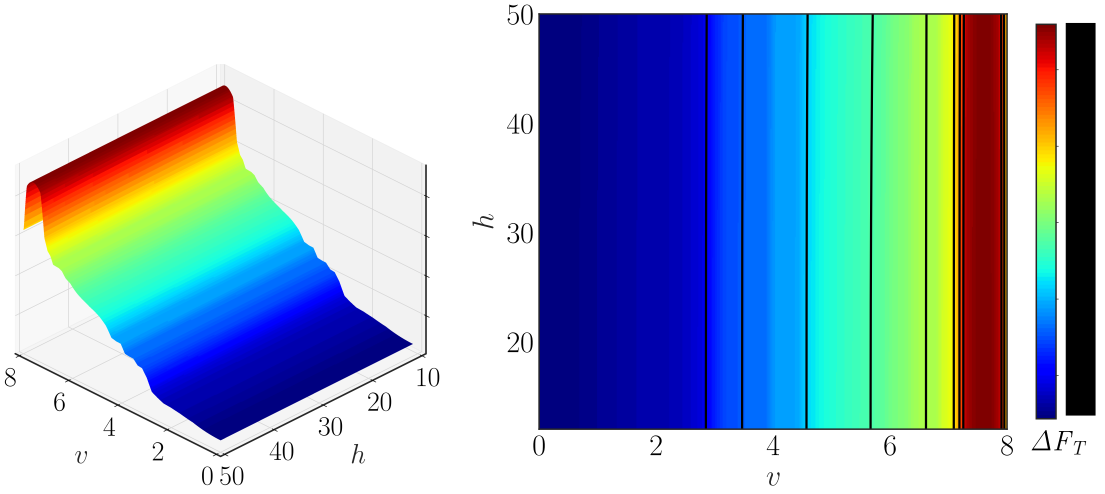

(c) *3D surface for* $\{h^3, Tv^2\}$ ***(d)*** *Contour plot for* $\{h^3, Tv^2\}$

Figure 6.3: Visualization of Kriging SMs developed with the initial dataset, using both independent variable sets, plotted at $T = 9.5\ m$. Units of the variables are, $h\ \{m\}$, $v\ \{ms^{-1}\}$, and $F_T\ \{kN\}$

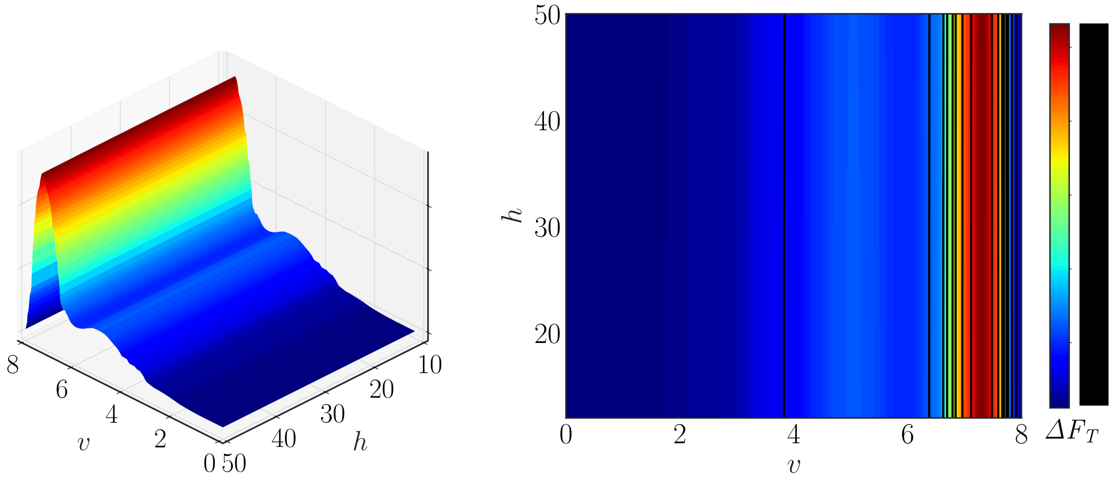

(a) *3D surface for* $\{h^3, T, v^3\}$

(b) *Contour plot for* $\{h^3, T, v^3\}$

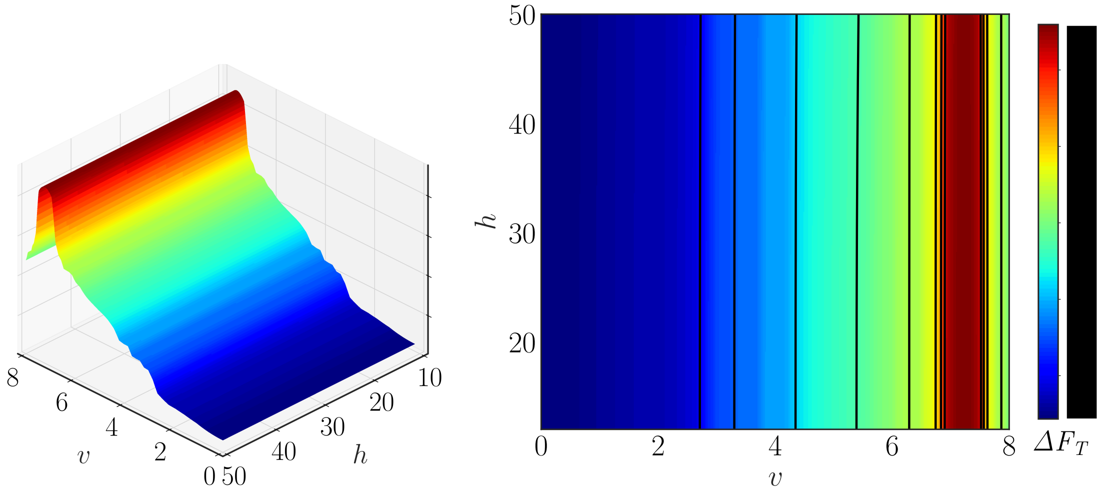

(c) *3D surface for* $\{h^3, Tv^2\}$

(d) *Contour plot for* $\{h^3, Tv^2\}$

Figure 6.4: Visualization of Kriging SMs developed with the initial dataset, using both independent variable sets, plotted at $T = 10.5\,m$. Units of the variables are, $h\,\{m\}$, $v\,\{ms^{-1}\}$, and $F_T\,\{kN\}$

6.3.2 Arrangement of SMs trained on extended dataset

The Kriging and ANN SMs developed using the extended dataset are evaluated in this subsection following the hyperparameter optimization stage. The performance of all the SMs generated in this regard will be discussed in the subsequent subsection.

The Kriging SMs generated for both sets of independent variables at draft values of $T = 9.5\ m$ and $T = 10.5\ m$ are illustrated in Figure 6.5 and Figure 6.6 respectively. The corresponding plots for the ANN SMs are presented in Figure 6.7 and Figure 6.8. The 3D views and contour plots reveal an obvious similarity between the shapes and overall behaviours of the models, along with some promising coherences with shallow water hydrodynamics.

- When v is increased and h is decreased, added resistance starts to steeply rise. This behaviour is consistent with the previously developed cubic-exponential interpolation surface created from the initial dataset (Figure 5.3). However, it is important to note that the independent variable in the cubic-exponential surface was ΔC_T, not ΔF_T. Regardless of the independent variable, this pattern aligns with the hydrodynamic theoretical findings established in earlier sections.
- The variation of shallow water resistance against depth-based Froude number can be used to further substantiate the above claim. The depth-based Froude number increases with either decreasing depth or increasing ship velocity, and along with that, the ship resistance increases as illustrated in Figure 3.5.
- Along the boundary of highest depth 50 m, ΔF_T becomes significantly small as the shallow water effects start to disappear at higher water depths. ΔF_T is also negligible along the boundary of $v = 0\ ms^{-1}$ as the suspended relative motion between hull and water leads to null resistance.

Although all the SMs show overall complying shapes with shallow water hydrodynamics, some details are not conforming at an intricate level. Among two Kriging models, the one corresponding to independent variable set 1 $\{h^3,\ T,\ v^2\}$ shows a number of local distortions (Figure 6.5a and Figure 6.5a). This becomes clearer when observing the wavy contour lines of Figure 6.5b and Figure 6.5d. It is not intuitively expected ΔF_T to exhibit such abrupt peaks and troughs, indicating that these distortions could potentially introduce local inaccuracies into the model. Also, the steep local rise of ΔF_T when $T = 9.5\ m$, within $h = [40,\ 50]\ m$ range is not valid (Figure 6.5a). While there should be a continuous rise in ΔF_T with increasing v, such an abrupt jump is not intuitive. Compared to the Kriging SM developed with the independent variable set 1, the one corresponding to independent variable set 2 looks more reliable. Its less wavy, smooth contour lines are arranged parallelly, and the presence of local ripples (deformities) is minimal.

While local deformities are less prevalent in both ANN models, their contour lines do exhibit noticeable waviness in areas of moderate v and h values. It is also questionable as to why the steep rise of ΔF_T seems to be approaching what seems to be a plateau at high v, low h regions (clearly seen on the ANN SM trained with independent variable set 2). Overall, the Kriging SM developed with the independent variable set 2 shows promising performance visually. However, this fact could be invalidated by the results of performance evaluation with Coefficient of Determination (CoD) indicator.

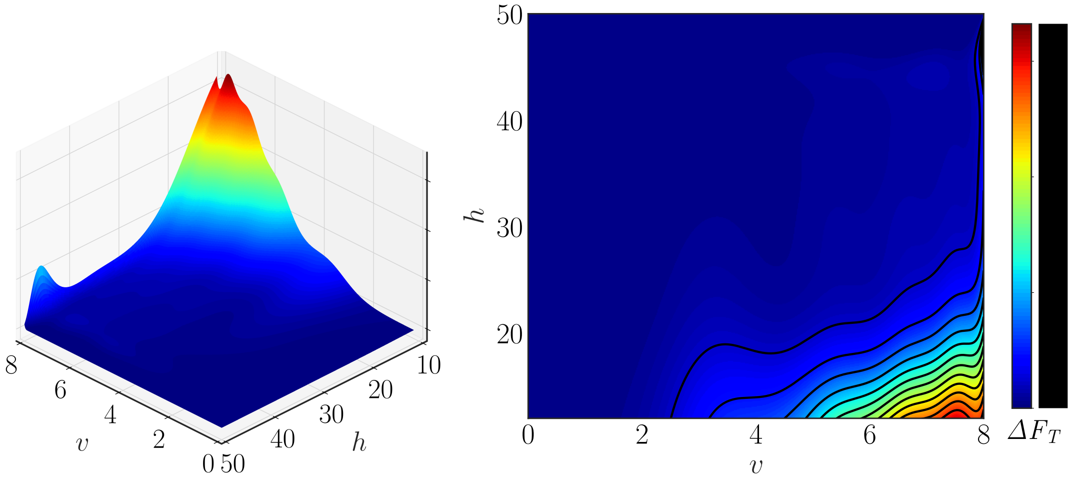

(a) 3D surface for $\{h^3, T, v^3\}$

(b) Contour plot for $\{h^3, T, v^3\}$

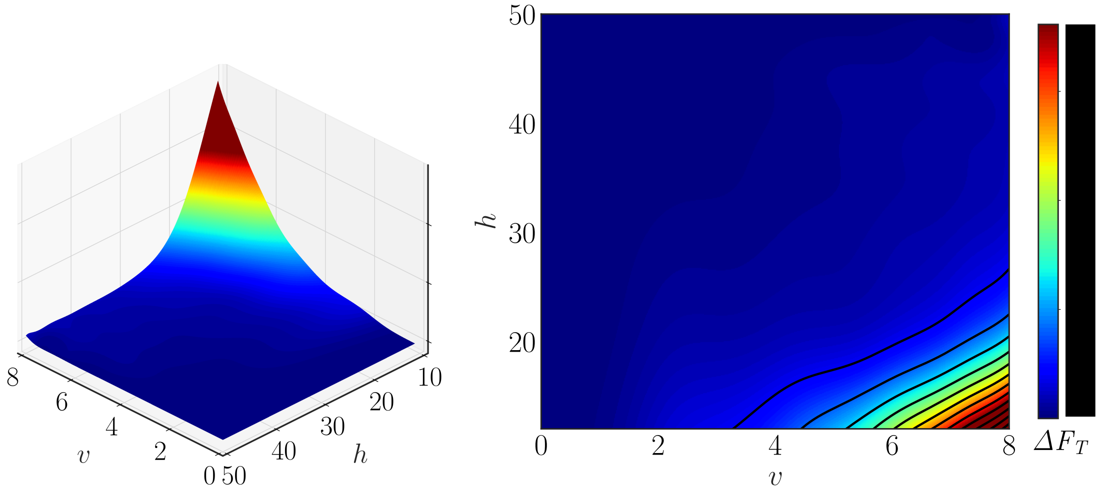

(c) 3D surface for $\{h^3, Tv^2\}$

(d) Contour plot for $\{h^3, Tv^2\}$

Figure 6.5: Visualization of hyperparameter optimized Kriging SMs developed with the extended dataset, using both independent variable sets, plotted at $T = 9.5\,m$. Units of the variables are, $h\,\{m\}$, $v\,\{ms^{-1}\}$, and $F_T\,\{kN\}$

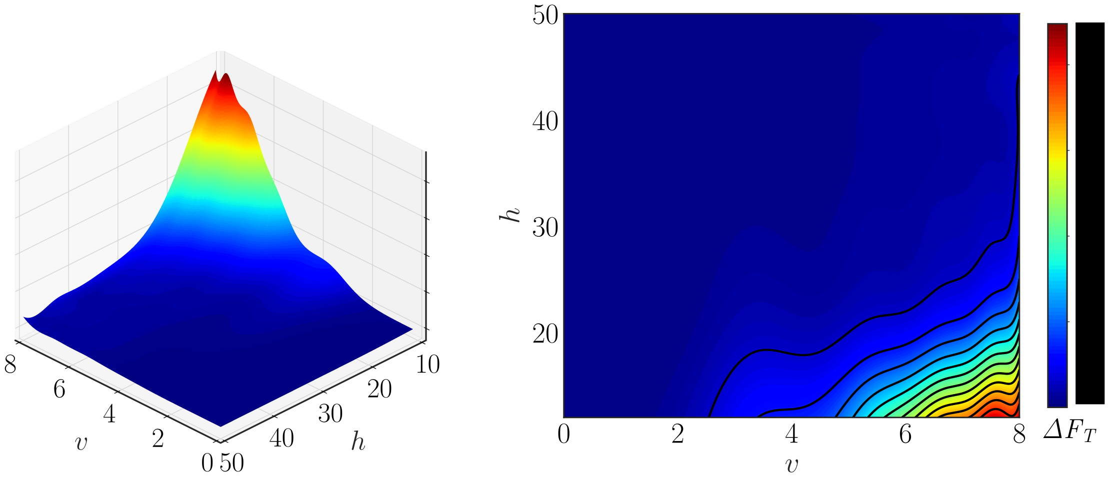

(a) *3D surface for* $\{h^3, T, v^3\}$ ***(b)*** *Contour plot for* $\{h^3, T, v^3\}$

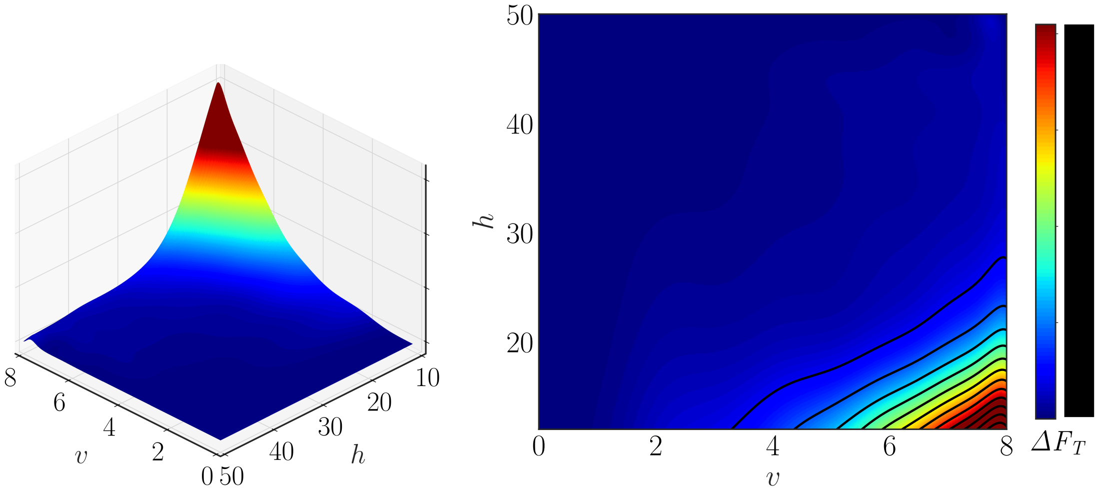

(c) *3D surface for* $\{h^3, Tv^2\}$ ***(d)*** *Contour plot for* $\{h^3, Tv^2\}$

Figure 6.6: Visualization of hyperparameter optimized Kriging SMs developed with the extended dataset, using both independent variable sets, plotted at $T = 10.5\,m$. Units of the variables are, $h\,\{m\}$, $v\,\{ms^{-1}\}$, and $F_T\,\{kN\}$

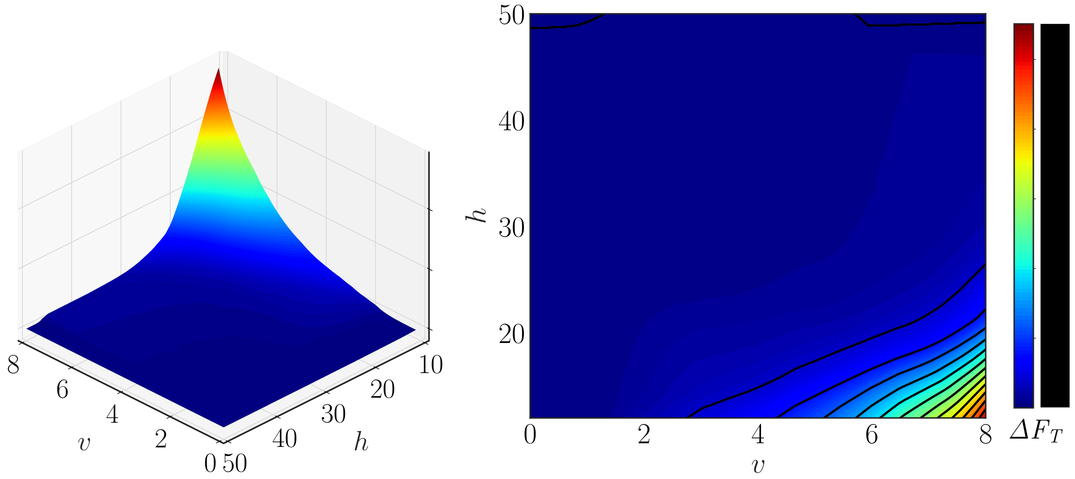

(a) *3D surface for* $\{h^3, T, v^3\}$ ***(b)*** *Contour plot for* $\{h^3, T, v^3\}$

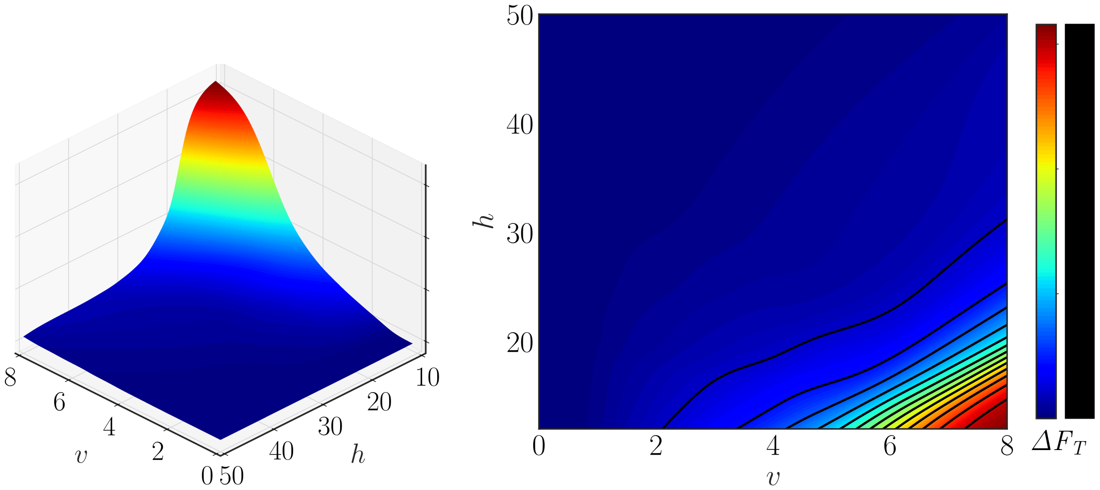

(c) *3D surface for* $\{h^3, Tv^2\}$ ***(d)*** *Contour plot* $\{h^3, Tv^2\}$

Figure 6.7: Visualization of hyperparameter optimized ANN SMs developed with the extended dataset, using both independent variable sets, plotted at $T = 9.5\,m$. Units of the variables are, $h\,\{m\}$, $v\,\{ms^{-1}\}$, and $F_T\,\{kN\}$

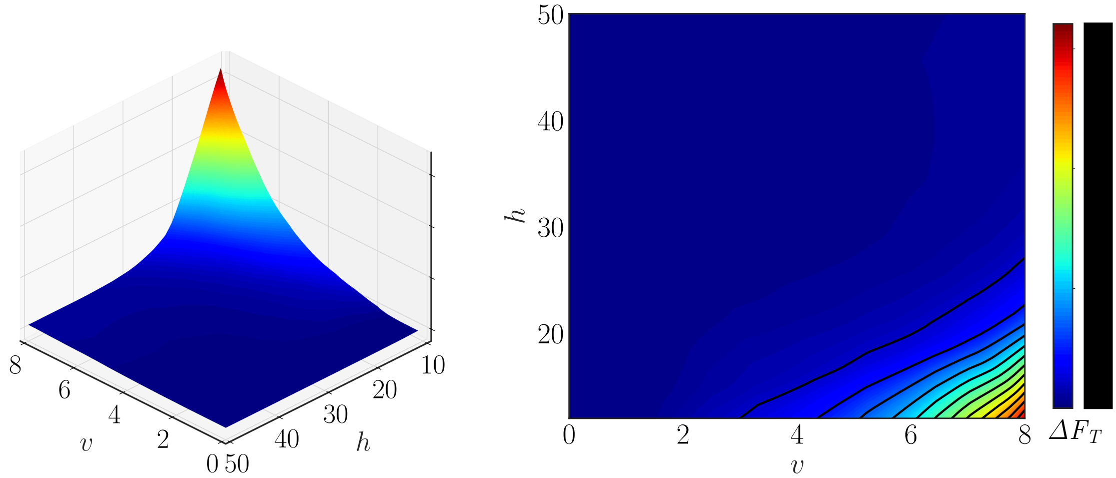

(a) *3D surface for* $\{h^3, T, v^3\}$ ***(b)*** *Contour plot for* $\{h^3, T, v^3\}$

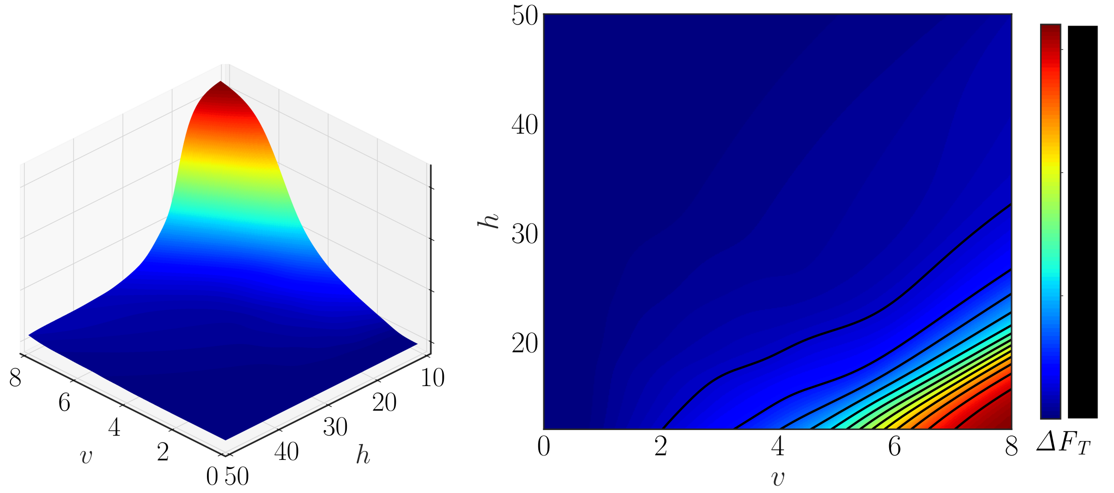

(c) *3D surface for* $\{h^3, Tv^2\}$ ***(d)*** *Contour plot for* $\{h^3, Tv^2\}$

Figure 6.8: Visualization of hyperparameter optimized ANN SMs developed with the extended dataset, using both independent variable sets, plotted when $T = 10.5\,m$. Units of the variables are, $h\,\{m\}$, $v\,\{ms^{-1}\}$, and $F_T\,\{kN\}$

6.3.3 Comparison of resistance curves

To further the understanding of the shape and arrangement of SMs, resistance curves were generated from two different slices of the DoI. The first set of resistance curves depicted in Figure 6.9 corresponds to the slice $\{h = 15\ m,\ T = 10.5\ m\}$. The second set of resistance curves depicted in Figure 6.10 corresponds to the slice $\{h = 50\ m,\ T = 10.5\ m\}$. In other words, the figures facilitate the comparison between resistance curves predicted by each SM, against the corresponding resistance curves generated from CFD results, at the design draft. Both a shallow water depth ($h = 15\ m$) and a moderate water depth ($h = 50\ m$) are considered to gain a better comprehension of surrogate models' reliability.

- Resistance curves predicted from the Kriging SMs and trained by the initial dataset largely deviate from the CFD curve, irrespective of the independent variable set employed. This deviation becomes more pronounced at the moderate water depth (Figure 6.10a). On top of that, resistance curves are posed with humps and hollows, or abrupt patterns, further adding to the conclusion that SMs developed using the initial dataset is inaccurate and unreliable.
- All other Kriging and ANN models trained by the extended dataset show a good correlation with the CFD resistance curve at shallow water depth. Among them, the Kriging curve corresponding to the independent variable set 2 almost coincides with the CFD curve, implying the best performance at shallow water depths (Figure 6.9b). Conversely, the ANN resistance curve corresponding to variable set 2 demonstrates the worst performance due to comparatively high deviations, especially at a high Frh range. (Figure 6.9c).
- At the moderate depth ($50\ m$), resistance curves of all four hyperparameter-optimized SMs trained with the extended training set are notably more deviated from the CFD resistance curve. The only curve that shows a fair correlation is again the one predicted from the Kriging model trained by variable set 2. At low Frh (< 0.15) range, ANN curve corresponding to variable set 2 shows a good correlation, but only to diverge significantly away and underpredict the resistance at higher Frh values.

From these observations, it becomes clear that the extended training dataset was somehow lacking in representing the shallow water resistance behavior around high velocity and high depth regions in DoI. This finding is further validated since not one, but all the SMs trained with the extended dataset exhibit increased deviations at $h = 50\ m$. With time, more sample points should be added to the training dataset, specifically around high h region.

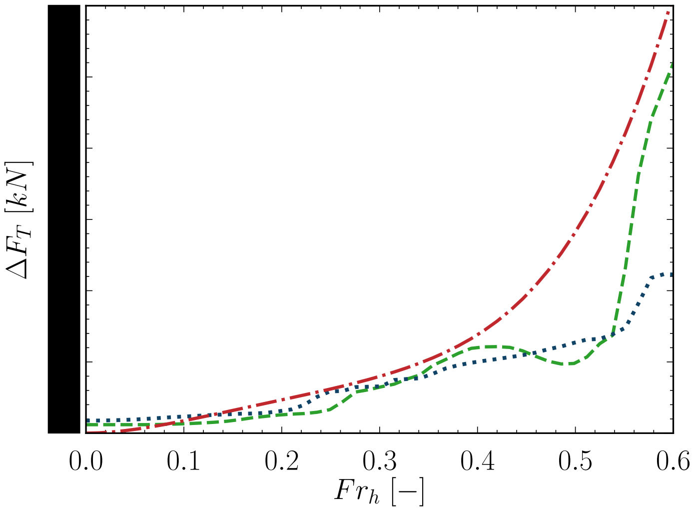
[redacted]

***(a)** Initial dataset - Kriging*

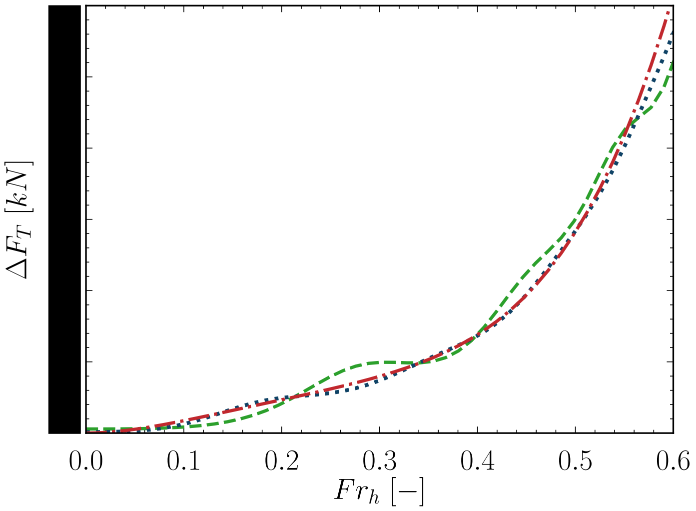
[redacted]

***(b)** Extended set - Kriging*

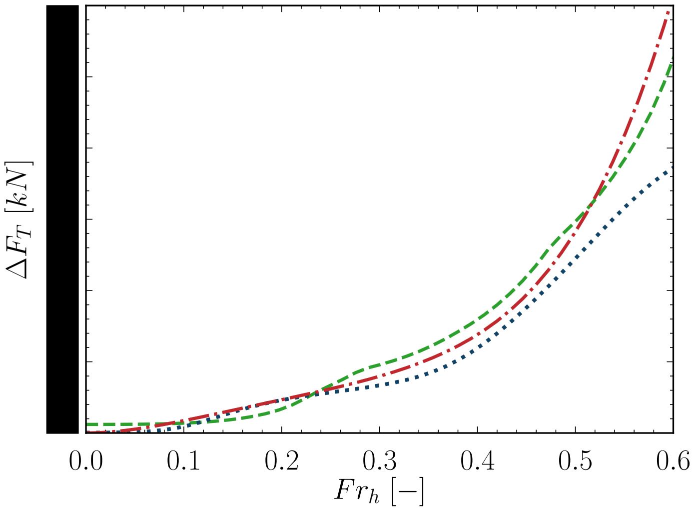
[redacted]

***(c)** Extended dataset - ANN*

Figure 6.9: Comparison of the real resistance curve with the predicted resistance curves generated through different surrogate models at $h = 15\,m$ and $T = 10.5\,m$. (- - - -) CFD calculated, (··········) Set $\{h^3, T, v^3\}$, (-·-·-·-) Set $\{h^3, Tv^2\}$

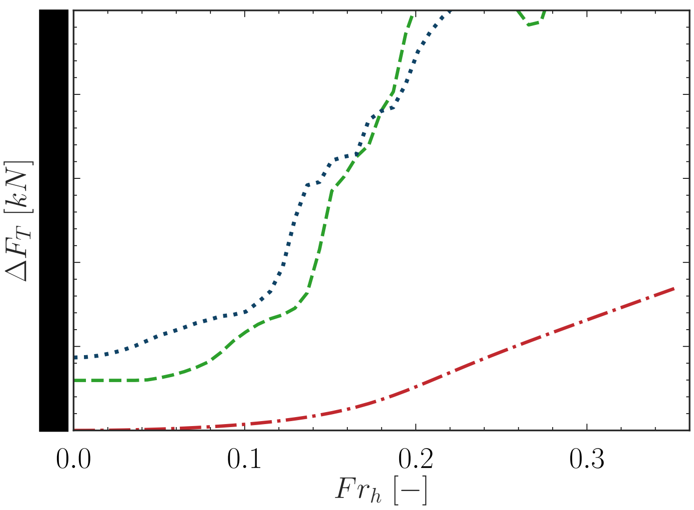
[redacted]

(a) *Initial dataset - Kriging*

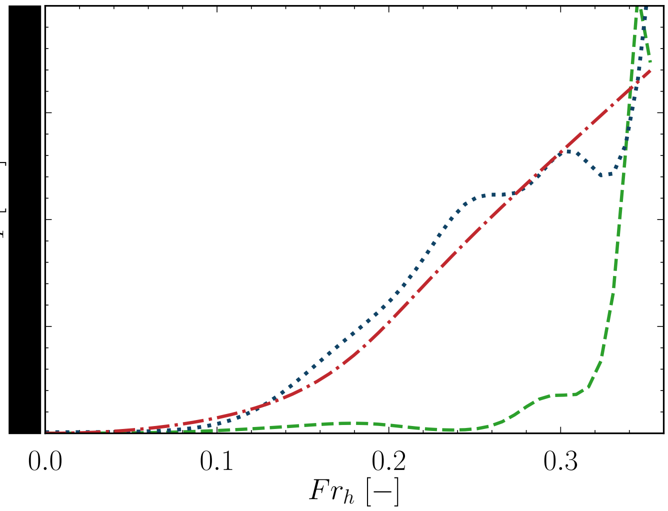
[redacted]

(b) *Extended set - Kriging*

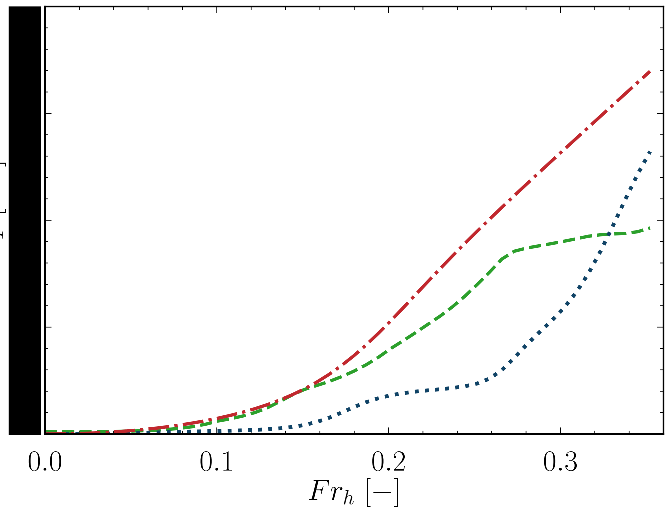
[redacted]

(c) *Extended dataset - ANN*

Figure 6.10: Comparison of the real resistance curve with the predicted resistance curves generated through different surrogate models at $h = 50\,m$ and $T = 10.5\,m$. (- - - -) CFD calculated, (⋯⋯⋯) Set $\{h^3, T, v^3\}$, (-·-·-·) Set $\{h^3, Tv^2\}$

6.3.4 Performance evaluation of SMs

The performance of each SM was evaluated against the Coefficient of Determination (CoD) r^2 criteria discussed in Section 6.2.2. The results are summarized in Figure 6.11.

- The accuracies of Kriging models developed with the initial dataset are the lowest ($r^2 < 0.5$) underscoring the inadequacy of 56 samples to represent complex underlying patterns in shallow water resistance phenomena.
- The role of hyperparameter optimization in improving model performance is evident for both Kriging and ANN models. The r^2 values for Kriging models (trained with set 1 and set 2) have been improved by 9% and 10% after the hyperparameter optimization. Even more significant 37% and 25% improvements have been achieved by the ANN models.
- The stacking regressor proves effective only with the ANN SMs, where it provides at least a 5% performance enhancement compared to the hyperparameter-tuned models. For the Kriging SMs, the stacked model exhibits lesser performance than both hyperparameter-tuned models.
- Validating the observations and insinuations made in previous analyses, the Kriging model trained with independent variable set 2 $\{h^3, Tv^2\}$ demonstrates the highest performance in terms of accuracy.

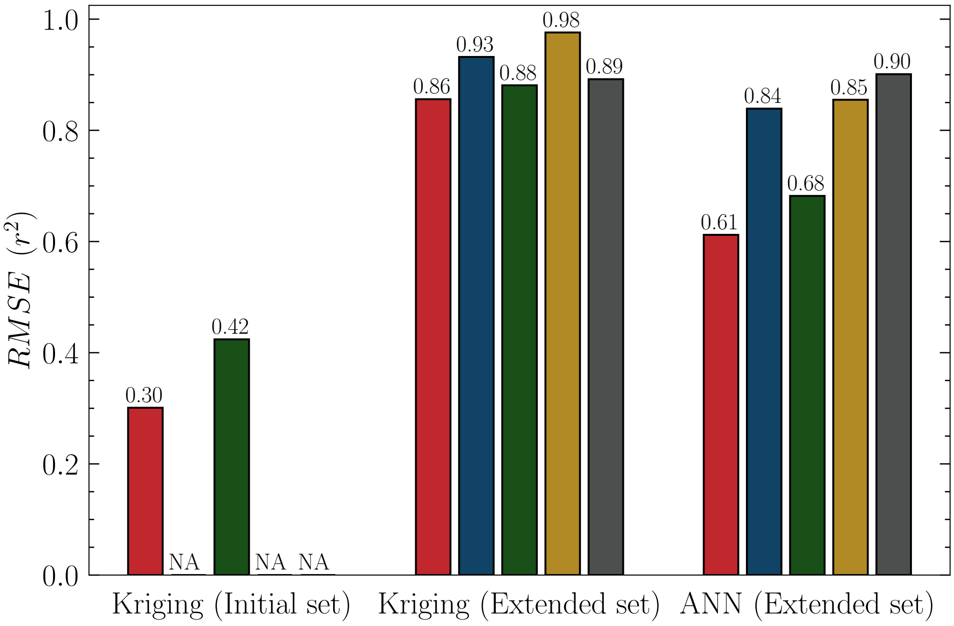

Figure 6.11: Performance of the Kriging SMs trained with initial dataset, and Kriging and ANN SMs trained with extended dataset, evaluated under the CoD (r^2) criteria,

🟥 Base SM with $\{h^3, T, v^3\}$
🟦 Hyperparameter tuned SM with $\{h^3, T, v^3\}$
🟩 Base SM with $\{h^3, Tv^2\}$
🟨 Hyperparameter tuned SM with $\{h^3, Tv^2\}$
⬛ Stacked SM with linear regression

6.4 Concluding remarks

The current chapter summarized the actions taken to successfully achieve the 1st and 2nd main objectives of the project. A number of base "Surrogate Models" (SMs) were developed to predict the added resistance in shallow water (ΔF_T) on the reference ship. These base SMs were subsequently optimized for enhanced performance using various tools observed in the literature.

- As highlighted throughout the report, the time constraints imposed restrictions on the size of the training set that could be used to develop the SMs. Therefore, a limited training set of ≈556 sample points was used to generate all SMs, except for those developed with the even more limited initial sample set of 56 samples.
- The Kriging SMs developed with the initial dataset proved to be markedly underperforming in terms of accuracy, and their characteristics were not even adhering to principles of shallow water resistance. This was the anticipated outcome given that the initial dataset was too sparse and small to adequately capture the DoI.
- All four hyperparameter-optimized Kriging and ANN SMs trained with the extended dataset, even with a sub-optimal number of sample points, exhibited more than 80% prediction accuracy as per the r^2 metric. Moreover, visual representations of all models demonstrated a good agreement with the principles of shallow water resistance. Therefore, the 1st and 2nd main objectives regarding the development of SMs and optimizing them are considered to be successfully achieved from the perspective of all the developed models.

The Kriging model corresponding to the independent variable set 2 $\{h^3, Tv^2\}$ and extended training dataset is concluded here as the best performing SM. It demonstrated a significant 97.5% (≈98%) prediction accuracy at the testing stage. Moreover, the overall shape of the model was intuitively better than other models, with the presence of local deformities at the lowest. In conclusion, it proves to be a dependable tool for predicting added resistance in shallow water within the context of the MARIDATA project, thereby satisfying the 2nd main objective. Nevertheless, additional refinements are suggested to ensure that the model maintains its prediction accuracy on a local scale:

- More training points should be introduced around the local regions with the presence of deformities (ripples on the surface). The method proposed in the next chapter directly addresses this problem to a satisfactory extent.
- The above-suggested actions are also intended to make the contour lines of the surface more parallel and smooth. Currently, the smooth and parallel contour lines at high velocity (v)-low depth (h) region start to deviate from this pattern when v decreases and h increases, as shown in Figure 6.5d and Figure 6.6d.
- The comparison of the resistance curves in Figure 6.9b and Figure 6.10b reaffirms that this SM is the "best performer" among all the SMs developed. The resistance curves predicted by this SM align more closely with the actual CFD generated curves than those generated by the other SMs. The increased deviation at the higher water depth should eventually diminish with the inclusion of additional training points, as recommended in Section 6.3.3.

CHAPTER

Development of the adaptive refinement loop

7

The chapter is dedicated to explaining the mechanism of the adaptive refinement loop developed to iteratively improve the base surrogate models.

The first and main phase of the surrogate development process was successfully concluded in the previous chapter. All four hyperparameter-optimized Kriging and ANN ANN models showed potential to serve as independent SMs for predicting added resistance in shallow water (with different accuracies). However, in terms of local and global accuracy, the Kriging model associated with the independent variable set 2 was marked as the best performer among the lot. Both ANN SMs were found to exhibit generally underwhelming performance compared to their Kriging counterparts. Therefore, it was decided to not consider them in further improvements. The focus will be exclusively on the "best performer" in future steps. The other Kriging model was also considered with the purpose of assessing its iterative improvement. The aim of this chapter is to develop a framework to iteratively improve the performance of Kriging models and fully automate it. Essentially, the workflow proposed with the Figure 2.5 is realized in the chapter.

7.1 Adaptive sampling strategies

As the name implies, the adaptive sampling concept is used to generate a set of sample points through dynamically updating criteria. Therefore, the main mechanism of adaptive sampling can be summarized as (1) identifying the regions of interest in a given surrogate model utilizing a dynamic criterion (which typically correlates to a performance evaluation metric such as RMSE), and (2) subsequently generating additional sampling points within the identified regions (Franzoi et al., 2021). Two more steps need to be introduced after the adaptive sampling process. These are (3) calculating the dependent variable for new sample points, and finally (4) appending the new sample points to the existing training set and retraining the SM. By setting this four-step process to execute in a recurring manner, the desired iterative development loop can be effectively established. Numerous adaptive sampling methods were discovered in the literature (X. Wang et al., 2021; Fuhg, Fau, and Nackenhorst, 2021). These methods stand apart from each other based on the dynamic criterion utilized to identify the regions of interest, as well as the method employed to generate the new sample points. Four different adaptive sampling methods and general LHS method were tested to determine the best sampling strategy to plan the iterative loop.

7.1.1 Iteratively established general LHS method

The general LHS method was considered to assess the effectiveness of the iterative loop with a non-adaptive sampling strategy. The algorithm is outlined in Algorithm 2. For further clarification, one can refer to Figure 2.5. In each iteration, a small set of sample points (with a desired number of samples n_{LHS}) is generated within the DoI. Following this, a Python script executing the iterative loop on the local computer initiates a `BASH` script, which runs on `Ubuntu 20.04.6`. This script handles the subsequent steps: (1) accessing the High-Performance Cluster (HPC), (2) launching CFD simulations corresponding to each new sample point, (3) monitoring until all the simulations reach completion, (4) retrieving the results and computing the ΔF_T values, and finally, (5) copying the completed sample dataset back to local Python script. The Python script then appends the new sample set with the current training dataset and retrains the Kriging model. Even without a dynamically updating adaptive criterion, the iterative expansion of the training set may lead to improved performance.

```
Algorithm 2: Iterative sampling with simple LHS
Input: Current training dataset, testing dataset, and surrogate model
for $i \leftarrow 1$ to $n_{iter}$ do
    Generate a desired number of ($n_{LHS}$) sample points in the DoI $\{h, T, v\}$
        $S_{LHS,k} = \{h_{LHS,k}, T_{LHS,k}, v_{LHS,k}\}$; with $k = 1, 2, \ldots, n_{LHS}$ ;
    Calculate $\Delta F_T$ for each $S_{LHS,k}$ and complete the sample set $S_{train,i}$;
    Append $S_{train,i}$ to the current training dataset and retrain the SM;
    Calculate the $r^2$ for the retrained model to check the performance ;
Output: An iteratively refined surrogate model
```

7.1.2 LHS sampling with uncertainty regions

The concept behind this adaptive sampling strategy revolves around supplementing the regions with the highest uncertainties with new training data points. With the new points introduced, the Kriging method will have more information to gather insights about the places where it had previously fallen short in maintaining its nominal prediction accuracy. The regions of interest are identified with the square error metric, which is simply the squared deviation between real and predicted values. For a single sample in the testing dataset, when the real ΔF_T calculated with CFD is $\Delta F_{T,i}$ and the corresponding predicted value is $\Delta \hat{F}_{T,i}$, the square value is given with, $SE_i = \left(\Delta F_{T,i} - \Delta \hat{F}_{T,i}\right)^2$. The uncertain regions are defined by isolating the coordinated of the test samples with 1% highest errors and setting upper and lower boundaries equally apart with respect to each dimension (the test set of 500 samples will generate 5 regions in each iteration). For instance, if the depth value corresponding to the test sample (i) is h_i, boundaries along the h dimension will be $[h_i + \delta_h,\ h_i - \delta_h]$. Then a random LHS point is generated for each region of interest. The rest of the steps follow the same procedure as general LHS sampling (Algorithm 3).

```
Algorithm 3: Adaptive sampling uncertainty regions and LHS
Input: Current training dataset, Current testing dataset
Input: Current surrogate model
for $i \leftarrow 1$ to $n_{iter}$ do
    Generate predictions for all test samples Calculate the square value of each test sample $SE_k = (y_k - \hat{y}_k)^2$; for $k = 1, 2, \ldots, n$ ;
    Isolate test point if $SE_k \in SE_{0.01} = \{1\%\ \text{highest errors}\}$ ;
    Extract sample coordinates corresponding to each $SE$ value in $SE_{0.01}$ from the test set $\rightarrow \{h_{0.01,k}, T_{0.01,k}, v_{0.01,k}\}$ ;
    Define small regions around each $\{h_{0.01,k}, T_{0.01,k}, v_{0.01,k}\}$. Each dimension is added and subtracted by $\delta$ value to define upper and lower limits.
        $R_{0.01,k} = \{[h_{0.01,k} \pm \delta_h]\ \ [T_{0.01,k} \pm \delta_T]\ \ [v_{0.01,k} \pm \delta_v]\}$ ;
    Generate a single sample point within each $R_{0.01,k}$ using LHS,
        $S_{SqLHS,k} = \{h_{SqLHS,k}, T_{SqLHS,k}, v_{SqLHS,k}\}$;
    Same 3-5 steps from the simple LHS algorithm
Output: An iteratively refined surrogate model
```

7.1.3 Voronoi tessellation with uncertainty regions

Voronoi Tessellation (VT) is a mathematical tool used to partition a given variable space into a series of convex cells (refer to Du and Gunzburger (2002) for further information). In this Voronoi-based adaptive sampling strategy, the whole DoI is partitioned into Voronoi cells before executing the loop. The 1% of most isolated points are identified through the same square error-based criteria as before. Then, the Voronoi cells each uncertain point located in are identified. A new sample point is generated for each identified cell by calculating the mean of all the vertices of that particular cell.

```
Algorithm 4: Adaptive sampling loop with Voronoi tessellation
Input: Current training dataset, Current testing dataset
Input: Current surrogate model
Partition the DoI of $\{h, T, v\}$ into a set of Voronoi cells $C = \{C_1, C_2, \ldots C_m\}$;
for $i \leftarrow 1$ to $n_{iter}$ do
    Generate predictions for all test samples Calculate the square value of each test sample $SE_k = (y_k - \hat{y}_k)^2$; for $k = 1, 2, \ldots, n$ ;
    Isolate test point if $SE_k \in SE_{0.01} = \{1\%\ \text{highest errors}\}$ ;
    Extract Voronoi cells each $SE$ value in $SE_{0.01}$ located in along with their vertices (when the number of vertices in a Voronoi cell is nv,
        $C_{0.01,k} = \{(h_{0.01,k,1}, T_{0.01,k,1}, v_{0.01,k,1}) \ldots (h_{0.01,k,nv}, T_{0.01,k,nv}, v_{0.01,k,nv})\}$ ;
    Calculate the mean of the vertices for each cell $C_{0.01,k}$ and declare them as new sample points $\rightarrow S_{VT,k} = \{h_{VT,k}, T_{VT,k}, v_{VT,k}\}$ ;
    Repeat 3-5 steps from the simple LHS algorithm
Output: An iteratively refined surrogate model
```

7.2 Results and discussion

The results of the adaptive refinement loop continued for 20 consecutive iterations are captured in Figure 7.1. The graphs show the development of performance for both Kriging SMs after each iterative retraining step using the r^2 metric as the performance indicator.

- Despite being an adaptive sampling method, Voronoi tessellation (VT) failed to deliver effective results. Except for a few minor improvements in certain iterations, the overall performances experienced a decline in both Kiriging models.
- Unexpectedly, the general LHS sampling, which merely adds new sample points without any adaptive criteria, outperformed the VT method. However, the model improvement with LHS appears to be erratic (suddenly drops with Kriging SM 1).
- The adaptive method of LHS combined with uncertainty regions yielded the best results, showing consistent improvement throughout the entire loop for both SMs. Therefore, it was finalized as the best solution to implement with the adaptive loop.

The Kriging SM 1 retained its status of "best performer" after the 20-step test run of the iterative loop (with ≈0.6% r^2 improvement). Therefore, the loop was set to continue with this model while iteratively improving it without any manual intervention (fully automated). The 3rd main objective of the thesis is thereby achieved.

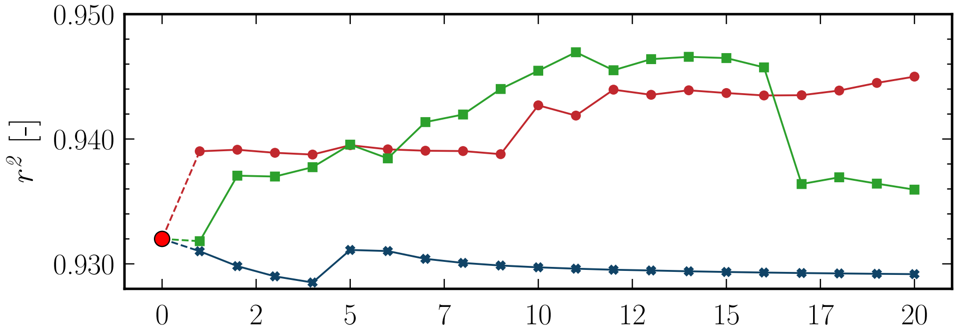

***(a)** Kriging SM with $\{h^3, T, v^3\}$*

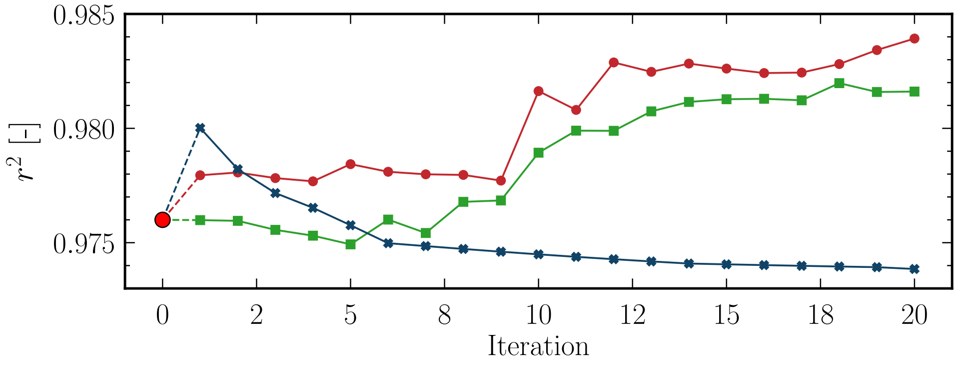

***(b)** Kriging SM with $\{h^3, Tv^2\}$*

Figure 7.1: Variation of the coefficient of determination (r^2) evaluated through 30 iterative steps for sampling strategies tested; (—■—) general LHS sampling, (—●—) LHS sampling with uncertainty regions, and (—×—) Voronoi tessellation, ⟨●⟩ r^2 values of base models

CHAPTER

Conclusion and outlook

8

The chapter is dedicated to providing a concise summary of the whole report along with the conclusions drawn in the end. Some insights for prospective extensions are also presented.

As the global outcry for sustainability grows louder and concerns about global warming and climate change become more pressing, the global shipping industry is undergoing a significant transformation aimed towards a more sustainable and greener status. The MARIDATA initiative is a project funded by the German Federal Ministry of Economic Affairs and Climate Action that aims to provide a substantial boost to this transformation by integrating the power of big data and artificial intelligence. Essentially, MARIDATA is envisioned as a digital twin-driven decision support system that provides rapid predictions for various ship operational conditions. This thesis presents a project specifically designed to address the MARISHALLOW component, a critical subset within the broader MARIDATA system.

8.1 Summary of the workflow and remarks

This thesis is founded on a convergence of ship hydrodynamics, numerical simulations, data analysis, and machine learning disciplines. The primary target was to develop a fast, efficient and reliable method to predict the added resistance on the reference ship –a medium-sized, modern chemical oil tanker of 192 m– when it is operating in shallow water conditions. The method will eventually be integrated into the MARIDATA system to aid the decision-support process surrounding shallow water ship operations. Through the application of response surface methodology and surrogate modelling techniques, this objective has been successfully achieved. The report discusses all the work carried out since the initiation of the project. Detailed observations and conclusions drawn from each chapter are provided at the end of the respective chapters. However, the following summary revisits the most noteworthy remarks:

- Theoretical studies: Comprehensive theoretical studies were carried out to understand the concepts surrounding the ship resistance and effects of shallow water, and Response Surface (RS) based surrogate modelling methods. The operational profile of the reference ship was found to mostly lie within the far-subcritical shallow water region with $Frh_{RefShip} < 0.76$. Therefore, regions with extreme non-linear resistance fluctuations were deemed to be not covered by the prospective surrogate model, highlighting a potential opportunity to adopt a more relaxed approach to calculate the training samples. Water depth (h), draft of the ship (T), and velocity of the ship (v) were chosen as the independent variables for the intended surrogate model. Among the numerous resistance calculation methods reviewed, Computational Fluid Dynamics (CFD) simulations were identified as the most suitable method to generate training points for the surrogate model.

- Literature review: The literature review was manoeuvred toward summarizing the crucial information regarding surrogate modelling. Most of the prediction-focused surrogate models, developed for non-linear phenomena of similar nature to shallow water ship resistance, were discovered to have employed substantially large training datasets, in the order of $[10^3 - 10^4]$. However, with the time constraints imposed, it was not feasible to generate a dataset of that magnitude with CFD calculations. Thus, the requirement devise a method for constructing a reliable and accurate surrogate model with an affordable training set was highlighted. This realization led to a thorough state-of-the-art review that focused on exploring the tools and methods available to tune the performance of a surrogate model. As a result, several important tools such as hyperparameter optimization, data normalization and transformation, and adaptive sampling were pegged to be integrated into the development process.
- Numerical setup: A CFD setup previously utilized by DST was adopted and fine-tuned to calculate the shallow water resistance, following a cross-validation step with model test results (97% agreement). This OpenFOAM setup operated on RANS equations implemented by the PIMPLE algorithm. By leveraging the fact that steep non-linear simulations (in near subcritical regions) were not considered within the work scope, the CFD setup was further simplified. After reducing the mesh elements by 33% followed by other simplifications, simulation time was reduced to 48 *hours* from the initial 72 *hours*, with a tolerable compromise of less than 5% accuracy drop. This efficiency gain facilitated the generation of more sample points within the limited time frame. A comparison of the CFD results between shallow water and deep water operational conditions (while keeping T and v unchanged) revealed a dramatic increment in all friction, pressure and wavemaking resistance components in shallow water conditions. This led to the declaration of two potential candidates for the independent variable: added resistance in shallow water ΔF_T ($= F_T^{shallow} - F_T^{deep}$) and its non-dimensional form ΔC_T.
- Surrogate definition and preprocessing of data: The Domain of Interest (DoI) of the intended surrogate model was defined by utilizing the knowledge gained through theoretical and literature results, and general intuition: $DoI_{SM} \rightarrow \{h = [11,\ 50]m,\ T = [9,\ 11]m,\ v = [0,\ 7.8]ms^1,\ h/T > 1.2,\ Frh < 0.6\}$. An already available initial dataset of 58 complete CFD calculated points was used to generate a primary surrogate model with combined cubic and exponential interpolation. This model demonstrated good predictive performance for ΔC_T within less than 5% error compared to real, CFD calculated values, in the region defined by the boundaries of the initial dataset. However, the sparse nature of this dataset raised concerns about its ability to act as an independent training set for a real machine learning surrogate model. Therefore, Latin Hypercube Sampling (LHS) strategy was used to generate an extended dataset of 1000 samples that were well distributed across the DoI. Later it was split in half, to declare the training

and test datasets and CFD simulations were commenced to calculate ΔF_T values for sample point h, T, v. The initial dataset was combined with this training dataset.

- Base surrogate model development: Both Kriging and Artificial Neural Networks (ANN) methods, which are frequently used in naval architecture-related literature to develop prediction surrogate models, were decided to be utilized. Prior to training the SMs, magnitudes of independent variables were normalized using scaler transformation (applied on both initial and extended training datasets, separately). The prospective dependent variables, ΔF_T and ΔC_T were transformed through Yeo-Johnson transformation to resemble a Gaussian normal distribution. These steps were the first of many performance-tuning strategies adopted from the state-of-the-art review. Using the collective outcome of four different feature selection methods, two different independent variable sets were defined. Due to the better correlation with selected independent variable sets, ΔF_T was finalized as the sole independent variable. The following six base surrogate models were then developed: two (ordinary) Kriging models corresponding to each independent variable set, trained with the small initial dataset, and two (ordinary) Kriging and two (multi-layer perceptron) ANN models corresponding to each independent variable set, but all trained with the extended training dataset.
- Optimized surrogate model development: Numerous hyperparameters associated with Kriging and ANN methods were optimized using a randomized search exploration method. Relevant optimal hyperparameters were separately sought for two Kriging and two ANN surrogate models trained with the extended dataset. Then the four models were retrained with optimized hyperparameters, resulting in four new surrogate models. Following that, hyperparameter-optimized Kiriging and ANN models were combined separately, through the linear regression-based stacking. With these additions, a set of 12 surrogate models was available for performance evaluation using the Coefficient of Determination (CoD) (r^2) criteria (results are presented in the next section).
- Initiation of the iterative refinement loop: As the second phase of the thesis, an iterative refining loop was established to refine the performance of the highest performing hyperparameter optimized Kriging surrogate models. At each iterative step, the loop was designed to identify areas with the highest prediction uncertainty (defined by the highest squared error of prediction) and generate new sample points around each region. Then, CFD simulations were run for each sample point generated. With the corresponding ΔF_T values calculated, the newly completed dataset would be added to the current training dataset, introducing more information about the previously uncertain regions. With this new information, the surrogate model would be retrained, thus progressively improving its accuracy and reliability.

8.2 Observations, conclusions and implications

The results of the performance evaluation of surrogate models with the r^2 matric are presented with the conclusions drawn.

- Ship hydrodynamic conditions in shallow water significantly deviate from the conditions in deep water. As the passage between the hull bottom and the seabed narrows, the flow beneath the hull accelerates significantly. The increased relative motion between water and the hull leads to higher skin friction resistance. Moreover, the wave profile of the hull forms larger amplitude waves in shallow water, causing the ship to disperse more propulsion energy to generate them. These notable effects, coupled with other hydrodynamic changes lead to a substantial increment in the total resistance acting on the hull, compared to the resistance in deep water conditions.

- The feature selection process concluded with the selection of two independent variable sets. Interestingly, both sets included the ship draft (T) in its original linear state. However, the water depth (h) and ship velocity (v) were transformed into their cubic or quadratic powers: Set $1\{h^3, T, v^3\}$ and Set $2\{h^3, Tv^2\}$. This highlights the non-linear behaviour of shallow water with respect to water depth (h) and ship velocity (v) and underscores the effectiveness of considering non-linear transformations of variables when modelling complex phenomena like shallow water resistance.
- The Kriging models trained with the small initial database demonstrated underwhelming low prediction accuracies with r^2 values of 0.30 and 0.42 for independent variable sets 1 and 2 respectively. The significant importance of having an adequately large training dataset that covers the whole DoI is highlighted by this. With more information fed into the surrogate model in the training phase, it will be able to identify the intricate patterns between variables, leading to higher prediction capabilities.
- Exceptional prediction performances were observed from the hyperparameter-optimized Kriging (0.93 and 0.98) and ANN (0.84 and 0.85) surrogate models. All these models, when visualized as 3D surfaces (with T considered as a fixed value and $h,\ v,\ \Delta F_T$ respectively represented in $x,\ y,\ z$ axes) were found to comply with theoretical, practical, and intuitive findings related to shallow water resistance behaviours. However, local deformities were present in all the models, highlighting possible weak points of the training dataset. It should be noted that the best affordable training dataset had already been utilized, considering the restrictive timeframe.
- The hyperparameter optimization led to 9% and 10% performance improvements in Kriging models. With ANN models, even higher 37% and 25% improvements were seen. The number of optimized hyperparameters was higher with the ANN models, which may have contributed to the refinement of a greater number of nuanced characteristics in the optimized models, leading to this significant jump in performance.
- With the presence of the least amount of local deformities, and with the highest prediction accuracy $r^2 = 0.98$, the Kriging model associated with the independent variable set 2 was finalized as the best performer. Further improvements were suggested to improve the local prediction accuracy, such as infusing more sample points around local deformities and higher-depth operational regions.

Achievement of the 1st main objective: *Develop a surrogate model using a dataset consisting of the best affordable number of sample points, that guarantees accurate prediction of added resistance exerting in the reference ship when it is operating in limited water depths with different drafts and velocities.*

The first objective has been achieved with the development of base-level Kriging and ANN surrogate models. The base Kriging models demonstrated prediction accuracies of 86% and 88% while ANN models demonstrated 61% and 68% predictive accuracies. The actions that were taken to achieve the second main objective called for further refinements to these base models.

Achievement of the 2nd main objective: *Explore the accuracy and limitations of the initial surrogate model and apply tools and techniques available in the literature to further tune its performance.*

The second objective is deemed to have been successfully achieved with any of the Kriging or ANN surrogate models improved with the hyperparameter optimisation. These models were direct results of the effective application of a variety of surrogate model performance tuning methods, which were identified through the literature review and the state-of-the-art survey, such as data normalization and transformation, hyperparameter optimization, and adaptive sampling. Each of the hyperparameter-optimized models possessed the capability to predict the added resistance in shallow water with more than 80% accuracy, within the domain of interest. However, since MARIDATA is supposed to be a high-end, reliable decision support system, the “best performer” Kriging model with 97.5% (≈98%) prediction accuracy is nominated here as the final outcome with respect to the second objective.

Achievement of the 3rd main objective: *Developing an iterative loop to continuously improve the already created base surrogate model by adding new sample points.*

The third objective was introduced to further improve the minor flaws of the outcome of the second objective. The solution was introduced as an adaptive refinement loop which can improve the performance of surrogate models with each iterative step. The concept of adaptive sampling was incorporated into the loop to identify areas of high prediction uncertainty and generate additional sample points in those regions. The refinement loop was tested with three distinct sampling strategies. These included the general LHS sampling and two adaptive sampling methods which focused on areas of high uncertainty identified through the squared error of prediction. The adaptive methods were either combined with Voronoi tessellation or LHS sampling for sample generation.

After conducting a test run of 20 iterations, it was observed that the LHS sampling combined with uncertainty regions yielded the most consistent and effective results. The test run was conducted on the two hyperparameter-optimized Kriging models which were chosen due to their superior performance characteristics compared to the other models. The finalized loop structure, which combined LHS sampling with uncertainty regions, resulted in performance improvements of 2% and 0.6% for the Kriging models, as measured by the r^2 metric. The “best performer” Kriging model associated with the independent variable set two retained its status with 98.2% improved prediction accuracy after the rest run. Therefore, it was decided to only use the loop on that model in the future.

Most importantly, this entire loop was developed to run in a fully automated manner, without any manual intervention. Letting the loop continue would eventually help eliminate local deformities in the surrogate model by reinforcing the weak areas of the original training set, thus assuring local prediction accuracy. The continuous operation of this loop, even beyond the conclusion of this thesis, and the work associated with it, will serve as a strategic measure to counteract the disadvantages imposed by the limited time frame.

Answers sought for the research question
How to use surrogate modelling techniques to develop a comprehensive framework that can replace computationally and economically expensive calculation methods like numerical simulations or model testing, when predicting non-linear hydrodynamic parameters of a ship?

The completion of the three main objectives and various sub-objectives has led to the synthesis of a comprehensive framework for generating surrogate models. This framework, which is a combination of the schematic flow diagrams presented in Figure 2.4 and Figure 2.5, is implemented as a Python script. External steps like running the CFD simulations are conducted through OpenFOAM and Ubuntu, making the whole framework completely open-source. This allows unrestricted access to future adaptations. The framework's versatility allows it to be easily tailored to model other ship-related phenomena, such as added resistance in waves or power consumption at high speeds. Simple initiating steps like redefining the variables and surrogate model limitations would be sufficient to launch the Python script. However, there are still some instances that require logical intervention, such as selecting the best features from feature selection results. It is believed that the discussions made available throughout this report would provide a guide to aid these interventions also. Generating surrogate models for added resistance in shallow water (same focus area as this work) acting on ships other than the reference ship is expected to be even more straightforward as most of the logic related to the hydrodynamics of shallow water applies universally. In other words, the majority of logical decisions already made thought this thesis would remain valid for most other ships too.

In conclusion, the developed framework presented in this thesis, aided by the theoretical, practical and logical insights provided throughout this report could serve as an important starting point to develop shallow water resistance prediction models for a variety of vessel types. With careful integration and logical decision-making, this use case can be extended into modelling other non-linear ship phenomena too. The future implications of this thesis and the work presented by it, therefore, extend even beyond the reference ship, and shallow water resistance applications. As per the specific focus of the MARISHALLOW project, the "best performer" Kriging model with a 97.6% prediction accuracy is nominated as a capable shallow water prediction model to be used in the MARIDATA decision support system. It is recommended to let the automated refining loop run for an adequate duration of time to further improve the local prediction accuracy of the model.

8.3 Recommendations for future work

With the lessons learnt, the following recommendations are given for prospective extensions of the project.

- The Python framework proposed and developed through this thesis can be readily utilized to generate a new surrogate model with a larger training dataset. Although calculating the added resistance for a large number of sample points would require a significant investment of time, the resulting surrogate model could offer more refined predictions at both global and local levels. Given that the parameters such as independent and dependent features would likely remain the same as in the current model, the training process for the new model will simply involve replacing the existing training dataset with the larger one and running the script.
- With a sufficiently large dataset, cross-validation schemes such as K-fold cross-validation could be employed to iteratively select the optimal training dataset for better performance. In this approach, a large sample set is partitioned into multiple subsets. Surrogate models are then trained with each subset, and the instance that performs the best is selected (S. H. Kim and Boukouvala, 2020).
- The stacking method, which was only used with a simple linear combination, could be further explored. The stacking regressor was only proved to be effective with the ANN methods. However, stacking of existing surrogate models can be done with more advanced methods than linear regression. The effectiveness of stacking with these other methods such as Random Forests (RF) and LASSO regression, should be assessed in future work.
- By leveraging the independence of resistance components from each other, the idea of developing separate surrogate models for each Viscous, pressure, and wavemaking resistance component should be explored. Each surrogate model could be developed with its own optimal characteristics (most relevant independent variable features and most suitable hyperparameters), which would allow them to more effectively capture the behaviours of their respective resistance component. Ultimately, the total resistance prediction could be obtained by simply adding the predictions from all three models.

Bibliography

Abdulkareem, S. H., Tech, D., and Gotman, A. (2002). “Study Of Michell’s Integral And Influence Of Viscosity And Ship Hull Form On Wave Resistance”. In.

Abinaya, S. and Devi, M. K. K. (2022). “Enhancing crop productivity through autoencoder-based disease detection and context-aware remedy recommendation system”. In: *Application of Machine Learning in Agriculture*. Ed. by Khan, M. A., Khan, R., and Ansari, M. A. Academic Press, pp. 239–262. ISBN: 978-0-323-90550-3. DOI: https://doi.org/10.1016/B978-0-323-90550-3.00014-X.

Alexiou, K., Pariotis, E. G., Leligou, H. C., and Zannis, T. C. (2022). “Towards data-driven models in the prediction of ship performance (speed-power) in actual seas: a comparative study between modern approaches”. In: *Energies* 15.16. ISSN: 1996-1073. DOI: 10.3390/en15166094.

Antony, J. (2014). “Fundamentals of design of experiments”. In: *Design of experiments for engineers and scientists*. Elsevier, pp. 7–17. ISBN: 978-0-08-099417-8. DOI: 10.1016/B978-0-08-099417-8.00002-X.

Asher, M. J., Croke, B. F. W., Jakeman, A. J., and Peeters, L. J. M. (2015). “A review of surrogate models and their application to groundwater modeling”. In: *Water Resources Research* 51.8, pp. 5957–5973. DOI: https://doi.org/10.1002/2015WR016967.

Baba, E. (1969). “Study on Separation of Ship Resistance Components”. In: *Journal of the Society of Naval Architects of Japan* 1969.125, pp. 9–22. DOI: 10.2534/jjasnaoe1968.1969.9.

Bai, Y., Sun, Z., Zeng, B., Long, J., Li, L., Oliveira, J. V. de, and Li, C. (2019). “A comparison of dimension reduction techniques for support vector machine modeling of multi-parameter manufacturing quality prediction”. In: *Journal of Intelligent Manufacturing* 30.5, pp. 2245–2256. ISSN: 1572-8145. DOI: 10.1007/s10845-017-1388-1.

Balduin, S., Tröschel, M., and Lehnhoff, S. (2019). “Towards domain-specific surrogate models for smart grid co-simulation”. In: *Energy Informatics* 2.1, p. 27. ISSN: 2520-8942. DOI: 10.1186/s42162-019-0082-2.

Barnes, E. C. and McArthur, J. (2019). “Building energy use surrogate model feature selection – a methodology using forward stepwise selection and LASSO regression methods”. In: *Proceedings of the 16th IBPSA Conference*. Rome, Italy: International Building Performance Simulation Association, pp. 3078–3085. DOI: https://doi.org/10.26868/25222708.2019.211250.

Bartz, B. T. (2016). “Stacked generalization of surrogate models-a practical approach”. In: URL: https://api.semanticscholar.org/CorpusID:54002531.

Bartz, T. B. (2021). “Surrogate model based hyperparameter tuning for deep learning with SPOT”. In: *Computer Science* abs/2105.14625.

Bastin, L., Cornford, D., Jones, R., Heuvelink, G. B. M., Pebesma, E., Stasch, C., Nativi, S., Mazzetti, P., and Williams, M. (2013). “Managing uncertainty in integrated environmental modelling: The UncertWeb framework”. In: *Environmental Modelling & Software* 39, pp. 116–134. ISSN: 1364-8152. DOI: https://doi.org/10.1016/j.envsoft.2012.02.008.

Beckers, T. (2021). *An Introduction to Gaussian Process Models*. arXiv: `2102.05497 [eess.SY]`.

Bennett, N. D., Croke, B. F. W., Guariso, G., Guillaume, J. H. A., Hamilton, S. H., Jakeman, A. J., Marsili-Libelli, S., Newham, L. T. H., Norton, J. P., Perrin, C., Pierce, S. A., Robson, B., Seppelt, R., Voinov, A. A., Fath, B. D., and Andreassian, V. (2013). “Characterising performance of environmental models”. In: *Environmental Modelling & Software* 40, pp. 1–20. ISSN: 1364-8152. DOI: https://doi.org/10.1016/j.envsoft.2012.09.011.

Bertram, V. (2012). “Chapter 3 - Resistance and Propulsion”. In: *Practical Ship Hydrodynamics (Second Edition)*. Ed. by Bertram, V. Second Edition. Oxford: Butterworth-Heinemann, pp. 73–141. ISBN: 978-0-08-097150-6. DOI: https://doi.org/10.1016/B978-0-08-097150-6.10003-X.

Birk, L. (2019). “Potential Flow”. In: *Fundamentals of Ship Hydrodynamics*. John Wiley & Sons, Ltd. Chap. 15, pp. 177–190. ISBN: 9781119191575. DOI: https://doi.org/10.1002/9781119191575.ch15.

Birkhoff, G. (1983). “Numerical fluid dynamics”. In: *SIAM Review* 25.1, pp. 1–34. ISSN: 00361445. URL: http://www.jstor.org/stable/2030018.

Bouman, E. A., Lindstad, E., Rialland, A. I., and Strømman, A. H. (2017). “State-of-the-art technologies, measures, and potential for reducing GHG emissions from shipping – A review”. In: *Transportation Research Part D: Transport and Environment* 52, pp. 408–421. ISSN: 1361-9209. DOI: https://doi.org/10.1016/j.trd.2017.03.022.

Box, E. P. G. and Draper, N. R. (1987). “Introduction to response surface methodology”. In: *Empirical Model-Building and Response Surfaces*. New York: John Wiley & Sons, p. 15. ISBN: 0471810339.

Box, E. P. G. and Tidwell, P. W. (1962). “Transformation of the Independent Variables”. In: *Technometrics* 4.4, pp. 531–550. DOI: 10.1080/00401706.1962.10490038.

Box, E. P. G. and Wilson, K. B. (1951). “On the Experimental Attainment of Optimum Conditions”. In: *Journal of the Royal Statistical Society. Series B (Methodological)* 13.1, pp. 1–45. ISSN: 00359246. URL: http://www.jstor.org/stable/2983966.

Breidenthal, R. E. (2005). “Featured review: recent books on fluid mechanics”. In: *SIAM Review* 47.3. Ed. by Mulley, R., Feireisl, E., Novotny, A., Straskraba, I., Zeytounian, R. K., Kundu, P. K., Cohen, I. M., and Oertel, H., pp. 579–582. ISSN: 00361445. URL: http://www.jstor.org/stable/20453670.

Breiman, L. (2001). “Random Forests”. In: *Machine Learning* 45.1, pp. 5–32. ISSN: 1573-0565. DOI: 10.1023/A:1010933404324.

BSRA (1971). *Methodical series experiments on single-screw oceangoing merchant ship forms: extended and revised overall analysis*. Tech. rep. Wallsend, UK: Wallsend Research Station, pp. 5–7.

Cai, L., Ren, L., Wang, Y., Xie, W., Zhu, G., and Gao, H. (2021). "Surrogate models based on machine learning methods for parameter estimation of left ventricular myocardium". In: *Royal Society Open Science* 8.1, p. 201121. DOI: 10.1098/rsos.201121.

Carlton, J. S. (2007). "Ship resistance and propulsion". In: *Marine Propellers and Propulsion (Second Edition)*. Ed. by Carlton, J. S. Second Edition. Oxford: Butterworth-Heinemann, pp. 286–318. ISBN: 978-0-7506-8150-6. DOI: https://doi.org/10.1016/B978-075068150-6/50014-0.

Chen, G., Zhang, K., Xue, X., Zhang, L., Yao, C., Wang, J., and Yao, J. (2022). "A radial basis function surrogate model assisted evolutionary algorithm for high-dimensional expensive optimization problems". In: *Applied Soft Computing* 116, p. 108353. ISSN: 1568-4946. DOI: https://doi.org/10.1016/j.asoc.2021.108353.

Chorin, A. J. (1968). "Numerical solution of the Navier-Stokes equations". In: *Mathematics of Computation* 22.104, p. 745. ISSN: 00255718. DOI: 10.2307/2004575.

Constantin, P. (2008). "Euler and Navier-Strokes equations". In: *Publicacions Matemàtiques* 52.2, pp. 235–265. ISSN: 02141493, 20144350. URL: http://www.jstor.org/stable/43736891.

Coppedè, A., Gaggero, S., Vernengo, G., and Villa, D. (2019). "Hydrodynamic shape optimization by high fidelity CFD solver and Gaussian process based response surface method". In: *Applied Ocean Research* 90, p. 101841. ISSN: 0141-1187. DOI: https://doi.org/10.1016/j.apor.2019.05.026.

Corrales, D. C., Schoving, C., Raynal, H., Debaeke, P., Journet, E.-P., and Constantin, J. (2022). "A surrogate model based on feature selection techniques and regression learners to improve soybean yield prediction in southern France". In: *Computers and Electronics in Agriculture* 192, p. 106578. ISSN: 0168-1699. DOI: https://doi.org/10.1016/j.compag.2021.106578.

Cui, T., Pagendam, D., and Gilfedder, M. (2021). "Gaussian process machine learning and Kriging for groundwater salinity interpolation". In: *Environmental Modelling & Software* 144, p. 105170. ISSN: 1364-8152. DOI: https://doi.org/10.1016/j.envsoft.2021.105170.

Darmon, A., Benzaquen, M., and Raphaël, E. (2014). "Kelvin wake pattern at large Froude numbers". In: *Journal of Fluid Mechanics* 738, R3. ISSN: 0022-1120. DOI: 10.1017/jfm.2013.607.

Davis, S. E., Cremaschi, S., and Eden, M. R. (2018). "Efficient Surrogate Model Development: Impact of Sample Size and Underlying Model Dimensions". In: *13th International Symposium on Process Systems Engineering (PSE 2018)*. Ed. by Eden, M. R., Ierapetritou, M. G., and Towler, G. P. Vol. 44. Computer Aided Chemical Engineering. Elsevier, pp. 979–984. DOI: https://doi.org/10.1016/B978-0-444-64241-7.50158-0.

Daya, A. A. and Bejari, H. (2015). "A comparative study between simple kriging and ordinary kriging for estimating and modeling the Cu concentration in Chehlkureh deposit, SE Iran". In: *Arabian Journal of Geosciences* 8.8, pp. 6003–6020. ISSN: 1866-7538. DOI: 10.1007/s12517-014-1618-1.

Dias, F. (2014). "Ship waves and Kelvin". In: *Journal of Fluid Mechanics* 746, pp. 1–4. ISSN: 0022-1120. DOI: 10.1017/jfm.2014.69.

Dige, N. and Diwekar, U. (2018). “Efficient sampling algorithm for large-scale optimization under uncertainty problems”. In: *Computers & Chemical Engineering* 115, pp. 431–454. ISSN: 0098-1354. DOI: https://doi.org/10.1016/j.compchemeng.2018.05.007.

DNV (2022). *Ship energy efficiency management plan (SEEMP)*. URL: https://www.dnv.com/maritime/hub/decarbonize-shipping/key-drivers/regulations/imo-regulations/seemp.html [visited on 05/18/2023].

Du, Q. and Gunzburger, M. (2002). “Grid generation and optimization based on centroidal Voronoi tessellations”. In: *Applied Mathematics and Computation* 133.2, pp. 591–607. ISSN: 0096-3003. DOI: https://doi.org/10.1016/S0096-3003(01)00260-0.

Dubey, S. R., Singh, S. K., and Chaudhuri, B. B. (2022). *Activation Functions in Deep Learning: A Comprehensive Survey and Benchmark*. arXiv: 2109.14545 `[cs.LG]`.

Durighetto, N., Mariotto, V., Zanetti, F., McGuire, K. J., Mendicino, G., Senatore, A., and Botter, G. (2022). “Probabilistic description of streamflow and active length regimes in rivers”. In: *Water Resources Research* 58.4, e2021WR031344. DOI: https://doi.org/10.1029/2021WR031344.

Erickson, C. B., Ankenman, B. E., and Sanchez, S. M. (2018). “Comparison of Gaussian process modeling software”. In: *European Journal of Operational Research* 266.1, pp. 179–192. ISSN: 0377-2217. DOI: https://doi.org/10.1016/j.ejor.2017.10.002.

Faber, J. and Hoen, M. T. (2015). *Historical trends in ship design efficiency*. Tech. rep. Delft, NL: CE Delft, pp. 27–28. URL: https://www.transportenvironment.org/wp-content/uploads/2021/07/CE_Delft_7E50_Historical_trends_in_ship_design_efficiency_DEF.pdf.

Feng, D., Ye, B., Zhang, Z., and Wang, X. (2020). “Numerical Simulation of the Ship Resistance of KCS in Different Water Depths for Model-Scale and Full-Scale”. In: *Journal of Marine Science and Engineering* 8.10. ISSN: 2077-1312. DOI: 10.3390/jmse8100745.

Fischer, M. and Proppe, C. (2023). “Enhanced universal kriging for transformed input parameter spaces”. In: *Probabilistic Engineering Mechanics* 74, p. 103486. ISSN: 0266-8920. DOI: https://doi.org/10.1016/j.probengmech.2023.103486.

Forrester, A. I. J. and Keane, A. J. (2009). “Recent advances in surrogate-based optimization”. In: *Progress in Aerospace Sciences* 45.1, pp. 50–79. ISSN: 0376-0421. DOI: https://doi.org/10.1016/j.paerosci.2008.11.001.

Franzoi, R. E., Kelly, J. D., Menezes, B. C., and Swartz, C. L. E. (2021). “An adaptive sampling surrogate model building framework for the optimization of reaction systems”. In: *Computers & Chemical Engineering* 152, p. 107371. ISSN: 0098-1354. DOI: https://doi.org/10.1016/j.compchemeng.2021.107371.

Friedhoff, B., Hoyer, K., List, S., and Tenzer, M. (2019). “Investigation of the nominal and effective propeller inflow for a family of inland waterway vessels”. In: *Ocean Engineering* 187, p. 106180. ISSN: 0029-8018. DOI: https://doi.org/10.1016/j.oceaneng.2019.106180.

Fuhg, J. N., Fau, A., and Nackenhorst, U. (2021). “State-of-the-art and comparative review of adaptive sampling methods for Kriging”. In: *Archives of Computational Methods in Engineering* 28.4, pp. 2689–2747. ISSN: 1886-1784. DOI: 10.1007/s11831-020-09474-6.

Gao, L. (2020). “Towing Tank Test”. In: *Encyclopedia of Ocean Engineering*. Ed. by Weicheng, C., Shixiao, F., and Zhiqiang, H. Singapore: Springer Singapore, pp. 1–9. ISBN: 978-981-10-6963-5. DOI: 10.1007/978-981-10-6963-5.

Geiger, E. O. (2014). “Statistical methods for fermentation optimization”. In: *Fermentation and Biochemical Engineering Handbook (Third Edition)*. Ed. by Vogel, H. C. and Todaro, C. M. Third Edition. Boston: William Andrew Publishing, pp. 415–422. ISBN: 978-1-4557-2553-3. DOI: https://doi.org/10.1016/B978-1-4557-2553-3.00021-0.

George, A. (2012). “Anomaly detection based on machine learning dimensionality reduction using PCA and classification using SVM”. In: *International Journal of Computer Applications* 47, pp. 5–8.

Gertler, M. (1976). *Methods for the new analysis of the original data for the Taylor standard series*. Tech. rep. Washington D.C.: David W. Tayolor Model Basis.

Goodfellow, I., Bengio, Y., and Courville, A. (2016). *Deep Learning*. http://www.deeplearningbook.org. MIT Press.

Gotman, A. (2020). “Residual Resistance of Displacement Vessels”. In: *Journal of Marine Science and Engineering* 8.6. ISSN: 2077-1312. DOI: 10.3390/jmse8060400.

Gourlay, T. P. (2014). “ShallowFlow: A Program to Model Ship Hydrodynamics in Shallow Water”. In: *Volume 1A: Offshore Technology*. San Francisco, California: American Society of Mechanical Engineers, p. 8. ISBN: 978-0-7918-4537-0. DOI: 10.1115/OMAE2014-23291.

Grabowska, K. and Szczuko, P. (2015). “Ship resistance prediction with Artificial Neural Networks”. In: *2015 Signal Processing: Algorithms, Architectures, Arrangements, and Applications (SPA)*, pp. 168–173. DOI: 10.1109/SPA.2015.7365154.

Graff, W. (1964). “Some extensions of DW Taylor’s standard series”. In: *The Annual Meeting of The Society of Naval Architects and Marine Engineers, SNAME Transactions.*

Guerrero, J., Cominetti, A., Pralits, J., and Villa, D. (2018). “Surrogate-based optimization using an open-source framework: the bulbous bow shape optimization case”. In: *Mathematical and Computational Applications* 23.4. ISSN: 2297-8747. DOI: 10.3390/mca23040060.

Hadiyat, M. A., Sopha, B. M., and Wibowo, B. S. (2022). “Response Surface Methodology Using Observational Data: A Systematic Literature Review”. In: *Applied Sciences* 12.20. ISSN: 2076-3417. DOI: 10.3390/app122010663.

Harries, S. and Uharek, S. (2021). “Application of radial basis functions for partially-parametric modeling and principal component analysis for faster hydrodynamic optimization of a catamaran”. In: *Journal of Marine Science and Engineering* 9.10. ISSN: 2077-1312. DOI: 10.3390/jmse9101069.

Hauke, G. (2008). “Introduction to the Boundary Layer”. In: *An Introduction to Fluid Mechanics and Transport Phenomena*. Dordrecht: Springer Netherlands, pp. 187–197. ISBN: 978-1-4020-8537-6. DOI: 10.1007/978-1-4020-8537-6{_}11.

Hirt, C. W. and Nichols, B. D. (1981). “Volume of fluid (VOF) method for the dynamics of free boundaries”. In: *Journal of Computational Physics* 39.1, pp. 201–225. ISSN: 0021-9991. DOI: https://doi.org/10.1016/0021-9991(81)90145-5.

Hoffer, J. G., Geiger, B. C., and Kern, R. (2022). “Gaussian Process Surrogates for Modeling Uncertainties in a Use Case of Forging Superalloys”. In: *Applied Sciences* 12.3. ISSN: 2076-3417. DOI: 10.3390/app12031089.

Holtrop, J. and Mennen, G. G. J. (1982). “An approximate power prediction method”. In: *International shipbuilding progress* 29, pp. 166–170.

Hou, C. K. J. and Behdinan, K. (2022). “Dimensionality reduction in surrogate modeling: a review of combined methods”. In: *Data Science and Engineering* 7.4, pp. 402–427. ISSN: 2364-1541. DOI: 10.1007/s41019-022-00193-5.

IMO (2020). *Improving the energy efficiency of ships*. URL: https://www.imo.org/en/OurWork/Environment/Pages/Improving%5C%20the%5C%20energy%5C%20efficiency%5C%20of%5C%20ships.aspx [visited on 05/18/2023].

IMO (2023). *International convention for the prevention of pollution from ships (MARPOL)*. URL: https://www.imo.org/en/About/Conventions/Pages/International-Convention-for-the-Prevention-of-Pollution-from-Ships-(MARPOL).aspx [visited on 05/16/2023].

ITTC (2008). *ITTC-Recommended procedures and guidelines: model manufacture, propeller models terminology and nomenclature for propeller geometry*. Tech. rep., pp. 1–20. URL: https://ittc.info/media/1203/75-01-02-01.pdf.

ITTC (2011). *Practical guidelines for ship CFD spplications*. Tech. rep. Rio de Janeiro, Brazil: 26th ITTC Specialist Committee on CFD in Marine Hydrodynamics. URL: https://ittc.info/media/1357/75-03-02-03.pdf.

ITTC (2017). *Preparation, conduct and analysis of speed/power trials: recommended procedures and guidelines*. Tech. rep. Specialist Committee on Ships in Operation at Sea of the 29th ITTC.

Janson, C. and Larson, L. (1997). “A method for the optimization of ship hulls from a resistance point of view”. In: *Symposium on Naval Hydrodynamics*. Washington, DC: The National Academic Press. DOI: https://doi.org/10.17226/5870.

Jiang, T. (2001). “A new method for resistance and propulsion prediction of ship performance in shallow water”. In: *Practical Design of Ships and Other Floating Structures*. Ed. by Wu, Y.-S., Cui, W.-C., and Zhou, G.-J. Shanghai, Chaina: Elsevier Science Ltd, pp. 509–515. ISBN: 978-0-08-043950-1. DOI: https://doi.org/10.1016/B978-008043950-1/50064-8.

Johnson, R. W. (1998). “The handbook of fluid dynamics”. In.

Kamath, C. (2022). “Intelligent sampling for surrogate modeling, hyperparameter optimization, and data analysis”. In: *Machine Learning with Applications* 9, p. 100373. ISSN: 2666-8270. DOI: https://doi.org/10.1016/j.mlwa.2022.100373.

Khezri, V., Panahi, M., Yasari, E., and Skogestad, S. (2021). “Application of Surrogate Models as an Alternative to Process Simulation for Implementation of the Self-Optimizing Control Procedure on Large-Scale Process Plants—A Natural Gas-to-Liquids (GTL) Case Study”. In: *Industrial & Engineering Chemistry Research* 60.13, pp. 4919–4929. ISSN: 0888-5885. DOI: 10.1021/acs.iecr.0c05715.

Kim, S. H. and Boukouvala, F. (2019). “Machine learning-based surrogate modeling for data-driven optimization: a comparison of subset selection for regression techniques”. English. In: 14. DOI: 10.1007/s11590-019-01428-7.

Kim, S. H. and Boukouvala, F. (2020). “Machine learning-based surrogate modeling for data-driven optimization: a comparison of subset selection for regression techniques”. In: *Optimization Letters* 14.4, pp. 989–1010. ISSN: 1862-4480. DOI: 10.1007/s11590-019-01428-7.

Kleijnen, J. P. C. (2009). “Kriging metamodeling in simulation: a review”. In: *European Journal of Operational Research* 192.3, pp. 707–716. ISSN: 0377-2217. DOI: https://doi.org/10.1016/j.ejor.2007.10.013.

Kleijnen, J. P. C. (2017). “Regression and Kriging metamodels with their experimental designs in simulation: a review”. In: *European Journal of Operational Research* 256.1, pp. 1–16. ISSN: 0377-2217. DOI: https://doi.org/10.1016/j.ejor.2016.06.041.

Koenhardono, E. S., Djatmiko, E. B., Soeprijanto, A., and Irawan, M. I. (2014). “Neural Network-Based Engine Propeller Matching (NN-EPM) for Trimaran Patrol Ship”. In: *Applied Mechanics and Materials* 493, pp. 388–394. ISSN: 1662-7482. DOI: 10.4028/WWW.SCIENTIFIC.NET/AMM.493.388.

Lackenby, H. (1961). *Note on the effect of shallow water on ship resistance.* Tech. rep. London, UK: British Shipbuilding Research Association.

Langtangen, H. P. (2012). *Numerical methods for the Navier Stokes equations.* Tech. rep. Oslo: University of Oslo, pp. 2–4. URL: http://hplgit.github.io/INF5620/doc/pub/main_ns.pdf.

Larsson, L., Regnström, B., Broberg, L., Li, D. Q., and Janson, C. E. (1999). “Failures, Fantasies, and Feats in the Theoretical/Numerical Prediction of Ship Performance”. In: *Hydrodynamics in Ship Design.* The National Academics Press. Chap. 3. DOI: https://doi.org/10.17226/9771.

Larsson, L. and Raven, C. H. (2010). “Inviscid flow around the hull, wave making, and wave resistance”. In: *The principles of naval architecture series: ship resistance and flow.* Ed. by Randolph, J. P. Jersey City, NJ: The Society of Naval Architects and Marine Engineers. Chap. 5. ISBN: 978-0-939773-76-3.

Laurie, A., Anderlini, E., Dietz, J., and Thomas, G. A. (2021). “Machine learning for shaft power prediction and analysis of fouling related performance deterioration”. In: *Ocean Engineering*, p. 108886.

Lee, D.-H., Kim, Y.-T., and Lee, S.-R. (2020). “Shallow landslide susceptibility models based on artificial neural networks considering the factor selection method and various non-linear activation functions”. In: *Remote Sensing* 12.7. ISSN: 2072-4292. DOI: 10.3390/rs12071194.

Lei, B., Kirk, T. Q., Bhattacharya, A., Pati, D., Qian, X., Arroyave, R., and Mallick, B. K. (2021). “Bayesian optimization with adaptive surrogate models for automated experimental design”. In: *npj Computational Materials* 7.1, p. 194. ISSN: 2057-3960. DOI: 10.1038/s41524-021-00662-x.

Lewis, E. V. (1989). *Principals of naval architecture.* Vol. 3. Alexandria, VA, USA: SNAME (The Society of Naval Architects and Marine Engineers).

Ley, J. and Moctar, O. el (2021). “A Comparative Study of Computational Methods for Wave-Induced Motions and Loads”. In: *Journal of Marine Science and Engineering* 9.1. ISSN: 2077-1312. DOI: 10.3390/jmse9010083.

Li, Q., Wang, J., and Su, G. (2022). “A Grasshopper optimization algorithm-based response surface method for non-probabilistic structural reliability analysis with an implicit performance function”. In: *Buildings* 12.7. ISSN: 2075-5309. DOI: 10.3390/buildings/12071061.

Lim, Y.-F., Ng, C. K., Vaitesswar, U. S., and Hippalgaonkar, K. (2021). “Extrapolative Bayesian optimization with Gaussian process and neural network ensemble surrogate models”. In: *Advanced Intelligent Systems* 3.11, p. 2100101. DOI: https://doi.org/10.1002/aisy.202100101.

Lin, Y., He, J., and Li, K. (2018). “Hull form design optimization of twin-skeg fishing vessel for minimum resistance based on surrogate model”. In: *Advances in Engineering Software* 123, pp. 38–50. ISSN: 0965-9978. DOI: https://doi.org/10.1016/j.advengsoft.2018.05.010.

Liu, Z., Lesselier, D., Sudret, B., and Wiart, J. (2020). “Surrogate modeling based on resampled polynomial chaos expansions”. In: *Reliability Engineering & System Safety* 202, p. 107008. ISSN: 0951-8320. DOI: https://doi.org/10.1016/j.ress.2020.107008.

Lu, J., Wang, Q., Zhang, Z., Tang, J., Cui, M., Chen, X., Liu, Q., Fei, Z., and Qiao, X. (2021). “Surrogate modeling-based multi-objective optimization for the integrated distillation processes”. In: *Chemical Engineering and Processing - Process Intensification* 159, p. 108224. ISSN: 0255-2701. DOI: https://doi.org/10.1016/j.cep.2020.108224.

MAN Energy Solutions (2021). *Basic principles of ship propulsion.* Tech. rep. MAN Energy Solutions, pp. 9–10.

Marion, M. and Temam, R. (1998). “Navier-stokes equations: Theory and approximation”. In: *Handbook of Numerical Analysis.* Vol. 6. Elsevier, pp. 503–689. ISBN: 1570-8659. DOI: https://doi.org/10.1016/S1570-8659(98)80010-0.

Masood, Z., Khan, S., and Qian, L. (2021). “Machine learning-based surrogate model for accelerating simulation-driven optimisation of hydropower Kaplan turbine”. In: *Renewable Energy* 173, pp. 827–848. ISSN: 0960-1481. DOI: https://doi.org/10.1016/j.renene.2021.04.005.

Massachusetts Institute of Technology, Department of Mechanical Engineering (2006). *Lecture notes on marine hydrodynamics.* Tech. Rep. Cambridge, MA: Massachusetts Institute of Technology. URL: https://web.mit.edu/13.021/demos/lectures/lecture2.pdf.

McKee, K. (2022). “Boundary Effects on Ideal Fluid Forces and Kelvin’s Minimum Energy Theorem”. In: *Journal of Fluid Mechanics* 959. DOI: 10.1017/jfm.2023.174.

Meng, X.-J., Jing, S.-K., Zhang, L.-X., Liu, J.-H., and Yang, H.-C. (2015). “A New Sampling Approach for Response Surface Method Based Reliability Analysis and Its Application”. In: *Advances in Mechanical Engineering* 7.1, p. 305473. DOI: 10.1155/2014/305473.

Menter, F. R. (1994). “Two-equation eddy-viscosity turbulence models for engineering applications”. In: *AIAA Journal* 32.8, pp. 1598–1605. DOI: 10.2514/3.12149.

Mikhailov, G. K. (2005). “Daniel Bernoulli, Hydrodynamica (1738)”. In: *Landmark Writings in Western Mathematics 1640-1940.* Ed. by Grattan-Guinness, I., Cooke, R., Corry, L., Crépel, P., and Guicciardini, N. Amsterdam: Elsevier Science. Chap. 9, pp. 131–142. ISBN: 978-0-444-50871-3. DOI: https://doi.org/10.1016/B978-044450871-3/50090-5.

Milaković, A.-S., Li, F., Marouf, M., and Ehlers, S. (2020). “A machine learning-based method for simulation of ship speed profile in a complex ice field”. In: *Ships and Offshore Structures* 15.9, pp. 974–980. DOI: 10.1080/17445302.2019.1697075.

Mittendorf, M. (2023). “Data-driven prediction of added resistance on ships in waves ”. PhD thesis. Lyngby, Denmark: Technical University of Denmark. ISBN: 978-87-7475-721-4.

Mittendorf, M., Nielsen, U. D., and Bingham, H. B. (2022). "Data-driven prediction of added-wave resistance on ships in oblique waves—A comparison between tree-based ensemble methods and artificial neural networks". In: *Applied Ocean Research* 118, p. 102964. ISSN: 0141-1187. DOI: https://doi.org/10.1016/j.apor.2021.102964.

Mittendorf, M. and Papanikolaou, A. D. (2021). "Hydrodynamic hull form optimization of fast catamarans using surrogate models". In: *Ship Technology Research* 68.1, pp. 14–26. DOI: 10.1080/09377255.2020.1802165.

Molland, A. F., Turnock, S. R., and Hudson, D. A. (2011). "Restricted Water Depth and Breadth". In: *Ship Resistance and Propulsion*. Cambridge University Press, pp. 97–107. DOI: 10.1017/CBO9780511974113.009.

Molland, A. F., Turnock, S. R., and Hudson, D. A. (2017). "Components of Hull Resistance". In: *Ship Resistance and Propulsion*. Cambridge University Press, pp. 12–69. DOI: 10.1017/9781316494196.005.

Montewka, J., Sinclair, H. R., Kujala, P., Haapala, J., and Lensu, M. (2013). "Modelling ship performance in ice using Bayesian networks". In.

Moriasi, D. N., Arnold, J. G., Liew, M., Bingner, R. L., Harmel, R. D., and Veith, T. L. (2007). "Model Evaluation Guidelines for Systematic Quantification of Accuracy in Watershed Simulations". In: *Transactions of the ASABE* 50, pp. 885–900.

Mucha, P., Moctar, O. el, Dettmann, T., and Tenzer, M. (2018). "An experimental study on the effect of confined water on resistance and propulsion of an inland waterway ship". In: *Ocean Engineering* 167, pp. 11–22. ISSN: 0029-8018. DOI: https://doi.org/10.1016/j.oceaneng.2018.08.009.

Nyshadham, C., Rupp, M., Bekker, B., Shapeev, A. V., Mueller, T., Rosenbrock, C. W., Csányi, G., Wingate, D. W., and Hart, G. L. W. (2019). "Machine-learned multi-system surrogate models for materials prediction". In: *Computational Materials* 5.1, p. 51. ISSN: 2057-3960. DOI: 10.1038/s41524-019-0189-9.

Oh, S. (2020a). "Comparison of a Response Surface Method and Artificial Neural Network in Predicting the Aerodynamic Performance of a Wind Turbine Airfoil and Its Optimization". In: *Applied Sciences* 10.18. ISSN: 2076-3417. DOI: 10.3390/app10186277.

Oh, S. (2020b). "Comparison of a response surface method and artificial neural network in predicting the aerodynamic performance of a wind turbine airfoil and its optimization". In: *Applied Sciences* 10.18. ISSN: 2076-3417. DOI: 10.3390/app10186277.

Oliveira, L. G., Paiva, A. P., Balestrassi, P. P., Ferreira, J. R., Costa, S. C., and Silva, C. P. H. (2019). "Response surface methodology for advanced manufacturing technology optimization: theoretical fundamentals, practical guidelines, and survey literature review". In: *The International Journal of Advanced Manufacturing Technology* 104.5, pp. 1785–1837. ISSN: 1433-3015. DOI: 10.1007/s00170-019-03809-9.

Papanikolaou, N. and Anyfantis, K. (2022). "Construction of surrogate models for predicting the buckling strength of stiffened panels through DoE and RSM methods". In: *Engineering Computations (Swansea, Wales)* 39.4, pp. 1374–1406. ISSN: 02644401. DOI: 10.1108/EC-03-2021-0176.

Petersen, J. P., Jacobsen, D. J., and Winther, O. (2012). "Statistical modelling for ship propulsion efficiency". In: *Journal of Marine Science and Technology* 17, pp. 30–39.

PIANC (1992). *Capability of ship manoeuvring simulation models for approach channels and fairways in harbours.* Tech. rep. Brussels: The World Association for Waterborne Transport Infrastructure.

Poorarbabi, A., Ghasemi, M., and Azhdary, M. (2020). "Concrete compressive strength prediction using neural networks based on non-destructive tests and a self-calibrated response surface methodology". In: *Journal of Nondestructive Evaluation* 39.4, p. 78. ISSN: 1573-4862. DOI: 10.1007/s10921-020-00718-w.

Queipo, N. V., Haftka, R. T., Shyy, W., Goel, T., Vaidyanathan, R., and Kevin Tucker, P. (2005). "Surrogate-based analysis and optimization". In: *Progress in Aerospace Sciences* 41.1, pp. 1–28. ISSN: 0376-0421. DOI: https://doi.org/10.1016/j.paerosci.2005.02.001.

Rawson, K. J. and Tupper, E. C. (2001). "Powering of ships: general principles". In: *Basic Ship Theory (Fifth Edition).* Ed. by Rawson, K. J. and Tupper, E. C. Fifth Edition. Oxford: Butterworth-Heinemann, pp. 365–410. ISBN: 978-0-7506-5398-5. DOI: https://doi.org/10.1016/B978-075065398-5/50013-3.

Razavi, S., Tolson, B. A., and Burn, D. H. (2012). "Numerical assessment of metamodelling strategies in computationally intensive optimization". In: *Environmental Modelling & Software* 34, pp. 67–86. ISSN: 1364-8152. DOI: https://doi.org/10.1016/j.envsoft.2011.09.010.

Razavipour, M., Legoux, J.-G., Poirier, D., Guerreiro, B., Giallonardo, J. D., and Jodoin, B. (2022). "Artificial neural networks approach for hardness prediction of copper cold spray laser heat treated coatings". In: *Journal of Thermal Spray Technology* 31.3, pp. 525–544. ISSN: 1544-1016. DOI: 10.1007/s11666-021-01311-x.

Rehbach, F. and Beielstein, B. T. (2019). "Feature selection for surrogate model-based optimization". In: *Proceedings of the Genetic and Evolutionary Computation Conference Companion.* GECCO '19. New York, NY, USA: Association for Computing Machinery, pp. 399–400. ISBN: 9781450367486. DOI: 10.1145/3319619.3322020.

Rosenbaum, B. and Schulz, V. (2012). "Efficient response surface methods based on generic surrogate models". In: *SIAM J. Sci. Comput.* 35.

Sarabia, L. A. and Ortiz, M. C. (2009). "Response Surface Methodology". In: *Comprehensive Chemometrics.* Ed. by Brown, S. D., Tauler, R., and Walczak, B. Oxford: Elsevier, pp. 345–390. ISBN: 978-0-444-52701-1. DOI: https://doi.org/10.1016/B978-044452701-1.00083-1.

Savasta, T. D. and Sobey, A. J. (2021). "Efficient vessel power prediction in operational conditions using machine learning". In: *Practical Design of Ships and Other Floating Structures.* Ed. by Okada, T. and Kawamura, Y. Singapore: Springer Singapore, pp. 350–367. ISBN: 978-981-15-4624-2.

Schiestel, R. and Chaouat, B. (2022). "Turbulence modeling and simulation advances in CFD during the past 50 years". en. In: *Comptes Rendus. Mécanique.* DOI: 10.5802/crmeca.114.

Schlichting, O. (1940). *Ship resistance in water of limited depth: resistance of seagoing vessels in shallow water.* Tech. rep. Washington DC: US Experimental Wave Tank. URL: https://dome.mit.edu/handle/1721.3/51252.

Segota, S. B., Anđelić, N., Kudláek, J., and Ep, R. (2019). “Artificial neural network for predicting values of residuary resistance per unit weight of displacement”. In: *Journal of Maritime & Transportation Science*.

Simpson, T., Toropov, V., Balabanov, V., and Viana, F. (2012). “Design and analysis of computer experiments in multidisciplinary design optimization: a review of how far we have come - or not”. In: *12th AIAA/ISSMO Multidisciplinary Analysis and Optimization Conference*. DOI: 10.2514/6.2008-5802.

Soares, C. (2015). “Gas Turbines: An Introduction and Applications”. In: *Gas Turbines (Second Edition)*. Ed. by Soares, C. Second Edition. Oxford: Butterworth-Heinemann, pp. 27–28. ISBN: 978-0-12-410461-7. DOI: https://doi.org/10.1016/B978-0-12-410461-7.00001-8.

Song, S., Terziev, M., Tezdogan, T., Demirel, Y. K., De Marco Muscat-Fenech, C., and Incecik, A. (2023). “Investigating roughness effects on ship resistance in shallow waters”. In: *Ocean Engineering* 270, p. 113643. ISSN: 0029-8018. DOI: https://doi.org/10.1016/j.oceaneng.2023.113643.

Stone, H. A. and Moin, P. (2023). “Introduction”. In: *Annual Review of Fluid Mechanics* 55.1, pp. 1–45. DOI: 10.1146/annurev-fl-55-101822-100001.

Sulovsky, I., Hauteclocque, G. d., Greco, M., and Prpić-Oršić, J. (2023). “Comparative Study of Potential Flow and CFD in the Assessment of Seakeeping and Added Resistance of Ships”. In: *Journal of Marine Science and Engineering* 11.3. ISSN: 20771312. DOI: 10.3390/jmse11030641.

Sun, G. and Wang, S. (2019). “A review of the artificial neural network surrogate modeling in aerodynamic design”. In: *Proceedings of the Institution of Mechanical Engineers, Part G: Journal of Aerospace Engineering* 233.16, pp. 5863–5872. DOI: 10.1177/0954410019864485.

Tadros, M., Ventura, M., and Guedes, S. C. (2023). “Review of the decision support methods used in optimizing ship hulls towards improving energy efficiency”. In: *Journal of Marine Science and Engineering* 11.4. ISSN: 2077-1312. DOI: 10.3390/jmse11040835.

Tezdogan, T., Incecik, A., and Turan, O. (2016). “Full-scale unsteady RANS simulations of vertical ship motions in shallow water”. In: *Ocean Engineering* 123, pp. 131–145. ISSN: 0029-8018. DOI: https://doi.org/10.1016/j.oceaneng.2016.06.047.

Todd, F. H. (1963). *Methodical experiments with models of single-screw merchant ships*. Tech. rep. Alexandria, Virginia, USA: Department of Navy, David Taylor Model Basin.

Tuck, E. O. (1966). “Shallow-water flows past slender bodies”. In: *Journal of Fluid Mechanics* 26.01, p. 81. ISSN: 0022-1120. DOI: 10.1017/S0022112066001101.

Uddin, S., Khan, A., Hossain, M. E., and Moni, M. A. (2019). “Comparing different supervised machine learning algorithms for disease prediction”. In: *BMC Medical Informatics and Decision Making* 19.1, p. 281. ISSN: 1472-6947. DOI: 10.1186/s12911-019-1004-8.

Vantorre, M. (2020). *Captive Manoeuvring Tests with Ship Models: A Review Of Actual Practice, Based On The 22nd ITTC Manoeuvring Committee Questionnaire*. Tech. rep. Antwerp, Belgium: University of Ghent, pp. 1–3.

Wagner, J. R., Mount, E. M., and Giles, H. F. (2014). “Design of experiments”. In: *Extrusion*. William Andrew Publishing, pp. 291–308. ISBN: 978-1-4377-3481-2. DOI: 10.1016/B978-1-4377-3481-2.00025-9.

Wang, P., Chen, Z., and Feng, Y. (2021). “Many-objective optimization for a deep-sea aquaculture vessel based on an improved RBF neural network surrogate model”. In: *Journal of Marine Science and Technology* 26.2, pp. 582–605. ISSN: 1437-8213. DOI: 10.1007/s00773-020-00756-z.

Wang, P., Feng, Y., Chen, Z., and Dai, Y. (2023). “Study of a hull form optimization system based on a Gaussian process regression algorithm and an adaptive sampling strategy, Part I: Single-objective optimization”. In: *Ocean Engineering* 279, p. 114502. ISSN: 0029-8018. DOI: https://doi.org/10.1016/j.oceaneng.2023.114502.

Wang, X., Ni, B., Zeng, L., and Liu, Y. (2021). “An adaptive sampling strategy for construction of surrogate aerodynamic model”. In: *Aerospace Science and Technology* 112, p. 106594. ISSN: 1270-9638. DOI: https://doi.org/10.1016/j.ast.2021.106594.

Weinblum, G. P., Kendrick, J. J., Todd, M. A., and Basin., D. W. T. M. (1952). *Investigation of wave effects produced by a thin body - TMB model 4125*. Washington, D.C: Dept. of the Navy, David Taylor Model Basin. URL: https://www.biodiversitylibrary.org/item/102278.

Westermann, P. and Evins, R. (2019). “Surrogate modelling for sustainable building design – A review”. In: *Energy and Buildings* 198, pp. 170–186. ISSN: 0378-7788. DOI: https://doi.org/10.1016/j.enbuild.2019.05.057.

Xu, H., Li, H., Xiang, G., and Zhang, X. (2021). “An improved adaptive surrogate model and application in thermal management system design”. In: *Materials & Design* 208, p. 109883. ISSN: 0264-1275. DOI: https://doi.org/10.1016/j.matdes.2021.109883.

Yadav, A. M., Chaurasia, R. C., Suresh, N., and Gajbhiye, P. (2018). “Application of artificial neural networks and response surface methodology approaches for the prediction of oil agglomeration process”. In: *Fuel* 220, pp. 826–836. ISSN: 0016-2361. DOI: https://doi.org/10.1016/j.fuel.2018.02.040.

Yang, L. and Shami, A. (2020). “On Hyperparameter Optimization of Machine Learning Algorithms: Theory and Practice”. In: *CoRR* abs/2007.15745. arXiv: 2007.15745. URL: https://arxiv.org/abs/2007.15745.

Yasemin, E. and Durmusoglu, A. (2022). “An efficient parameter tuning method based on the Latin Hypercube Hammersley Sampling and fuzzy C-Means clustering methods”. In: *Computer and Information Sciences Journal of King Saud University* 34.10, pp. 8307–8322. ISSN: 1319-1578. DOI: 10.1016/j.jksuci.2022.08.011.

Yazdi, J. and Salehi, N. S. A. A. (2014). “Adaptive surrogate modeling for optimization of flood control detention dams”. In: *Environmental Modelling & Software* 61, pp. 106–120. ISSN: 1364-8152. DOI: https://doi.org/10.1016/j.envsoft.2014.07.007.

Yeo, I.-k. and Johnson, R. A. (2000). “A new family of power transformations to improve normality or symmetry”. In: *Biometrika* 87, pp. 954–959.

Yuangyai, C. and Nembhard, H. B. (2010). “Chapter 8 - Design of Experiments: A Key to Innovation in Nanotechnology”. In: *Emerging Nanotechnologies for Manufacturing*. Ed. by Ahmed, W. and Jackson, M. J. Micro and Nano Technologies. Boston: William Andrew Publishing, pp. 207–234. ISBN: 978-0-8155-1583-8. DOI: https://doi.org/10.1016/B978-0-8155-1583-8.00008-9.

Zeng, Q. (2019). “ A method to improve the prediction of ship resistance in shallow water”. PhD thesis. Delft, Netherlands: Delft University of Technology, p. 78. DOI: 10.4233/uuid:d4d8524a-fedc-4949-a953-f5848a1634bb.

Zhang, Y. and Wu, Y. (2021). “Introducing machine learning models to response surface methodologies”. In: *Response Surface Methodology in Engineering Science*. Ed. by Kayaroganam, P. Rijeka: IntechOpen. Chap. 2. DOI: 10.5772/intechopen.98191.

Zhao, L.-e. (1984). *Optimal ship forms for minimum total resistance in shallow water*. Tech. rep. Hamburg, Germany: Technical University of Hamburg-Harburg. DOI: 10.15480/882.930.

Zheng, B. (2022). “Feature selection for global tropospheric ozone prediction based on the BO-XGBoost-RFE algorithm”. In: *Scientific Reports* 12.1, p. 9244. ISSN: 2045-2322. DOI: 10.1038/s41598-022-13498-2.

Zitzler, E. and Deb, K. (2000). “Comparison of multiobjective evolutionary algorithms: empirical results.” English. In: *Evolutionary computation* 8.2, pp. 173–195. ISSN: 10636560. DOI: 10.1162/106365600568202.